BETA SPECTRA OF THE MASS 12 NUCLEI

Thesis by

F. Curtis Michel

In Partial Fulfillment of the Requirements

For the Degree of

Doctor of Philosophy

California Institute of Technology

Pasadena, California

1962

ABSTRACT

This thesis, "The Beta Spectra of the Mass 12 Nuclei," is mainly concerned with an experimental test of the conserved-vector-current theory. This theory predicts a deviation from the allowed shape of the B^{12} and N^{12} beta spectra. The ratio of the shape factors of the two spectra is expected to have an energy dependence of 1.10 ± 0.17 percent per Mev. If the CVC hypothesis is not invoked, this ratio is estimated to be an order of magnitude smaller. The two spectra have been measured with a magnetic spectrometer and found to give for this ratio the value 1.30 ± 0.31 percent per Mev. In addition the branching fraction of the N^{12} decay to the 7.6-Mev state of C^{12} has been determined to be 3.0 ± 0.5 percent. The geometrical mean of the two shape factors was observed to have an unexpected linear energy dependence of 1.18 percent per Mev. Theoretical estimates are made of relevant matrix elements in search of an understanding of this. Baffle penetration by the beta particles gives a systematic effect estimated to account for about one third of the observed mean shape factor. The uncertainty in this estimate precludes a definite conclusion on the actual presence of this term in the spectra. Such penetration is expected, however, to have little influence on the conserved vector current theory test. A preliminary report of this work has been published (1, 2).

ACKNOWLEDGMENTS

The author is indebted to Professors T. Lauritsen, W. A. Fowler, H. A. Weidenmüller, C. A. Barnes, U. Hauser, and F. Boehm for valuable discussions and encouragement. He is particularly indebted to Dr. Theodor Mayer-Kuckuk of the Max-Planck-Institut für Kernphysik, Heidelberg, whose collaboration made this research possible. Two earlier experiments (3) in this laboratory by H. Hilton and V. Soergel and H. Hilton and C. Van der Leun provided much of the groundwork for this experiment. The assistance of Barbara A. Zimmerman with calculations is much appreciated.

The research was assisted by the joint program of the Office of Naval Research and the Atomic Energy Commission.

TABLE OF CONTENTS

I. THEORY

Universal Fermi Interaction

The suggestion has been made by several investigators (4) that the nuclear beta-decay interaction is just one manifestation of a Universal Fermi Interaction. It will be useful to give a definition of universality in anticipation of our needs here.

In the conventional field theory formulation the Lagrangian is written

$$L_{total} = \Sigma L_{free} + \Sigma L_{interaction} \tag{1}$$

where the first sum extends over all the elementary particles and the second sum is over all the fundamental interactions among the elementary particles. Whether or not it is meaningful to select certain particles as "elementary" and certain interactions as "fundamental" are important questions which will not be considered here. The weak interactions among the non-strange fermions are

$$n + \bar{p} \longrightarrow e + \bar{\nu} \tag{2a}$$

$$\mu + \bar{\nu} \longrightarrow e + \bar{\nu} \tag{2b}$$

$$n + \bar{p} \longrightarrow \mu + \bar{\nu} \tag{2c}$$

where n, p, e, ν, and μ represent respectively the neutron, proton, electron, neutrino, and negative muon, and the bar over a symbol indicates the antiparticle. Moving a particle from one side of the

reaction to the other changes it into the antiparticle. Thus the reactions

$$n \longrightarrow p + e + \bar{\nu} \tag{3a}$$

$$p \longrightarrow n + \bar{e} + \nu \tag{3b}$$

$$p + e \longrightarrow n + \nu \tag{3c}$$

$$n + \nu \longrightarrow p + e \tag{3d}$$

are formally equivalent although representing different processes (electron decay, positron decay, electron capture, and neutrino capture respectively). The postulate (5) is that the pairs in reactions 2a-2c, $(n\bar{p})$, $(e\bar{\nu})$, and $(\mu\bar{\nu})$, interact to produce the other pairs as indicated. The universality hypothesis is that the strength of the interaction and the form (scalar, vector, etc.) of the interaction are the same between any two pairs.

A more familiar example of a universal coupling is electromagnetism where the coupling constant, e^2, has the same magnitude for the electron, proton, muon, pion, etc., and the coupling form is vector in all cases. This example is misleading, however, because universality does not assert that exactly the same coupling constant and precisely the same coupling form will be observed experimentally. The presence of other interactions will in general modify the behavior of the actual physical particle.

Why then does the universality of electromagnetism show through so clearly in spite of the presence of very much stronger

interactions that could in principle alter e^2 in a fashion dependent upon the other couplings possessed by the particle? This situation is understood as a consequence of the principle of charge conservation. Thus, for example, the strong coupling $p \rightarrow n + \pi^+$ preserves the net charge before and after the interaction. The amplitude for the proton to virtually dissociate into a neutron and a positive pion does not change the net charge of the system, although influencing the distribution of this charge.

On the other hand, the proton can positron decay (in nuclei) while the neutron cannot; hence one might expect crudely that the effective beta-decay coupling would be reduced due to such virtual dissociation. All one could then hope for is that the universality of the interaction is not completely obscured by the strong interactions. In fact, experiment seems to indicate that the axial vector coupling constant, $-G_A$, is about 20% larger (6) than the vector coupling constant, G_V. Presumably this is just such an effect. Fortunately the decay $\mu \rightarrow e + \nu + \bar{\nu}$ allows the determination of the beta-decay coupling constant without interference from the strong interactions, since none of the particles involved is strongly coupled.

Conserved Vector Current Hypothesis

Surprisingly, the coupling constant derived from muon decay, G^μ, and G_V as determined from nuclear physics (7) are equal within a few percent. The problem now is to explain why G_V is <u>not</u>

different from G^{μ} in spite of the strong interactions that are supposedly responsible for the disparity between $-G_A$ and G_V.

To understand this, it was proposed (8,9) that the vector part of the beta-decay current is conserved in analogy to the conservation of the vector electromagnetic current. Thus was born the conserved-vector-current (CVC) theory.

Such a theory automatically predicts $G_V = G^{\mu}$, except for electromagnetic corrections, and to further test its validity one must look for other consequences.

The interaction of the strongly interacting particles with the electromagnetic field, A_a, can be written $J^{em} \cdot A$ where

$$J_a^{em} = \sqrt{4\pi}\, e\left[\bar{\psi}\gamma_a \frac{1}{2}(1+\tau_z)\psi + i(\phi^* T_z \partial_a \phi - (\partial_a \phi)^* T_z \phi) + \ldots\right] \qquad (4)$$

is the electromagnetic current with

$$\tau_z p = p, \tau_z n = -n,$$
$$T_z \pi^{\pm} = \pm \pi^{\pm}, \; T_z \pi^0 = 0,$$
$$\psi = n \text{ or } p, \text{ and } \phi = \pi^{\pm}, \pi^0.$$

Only the nucleon and pion contributions have been written explicitly. For convenience, we will treat the strong interactions as consisting fundamentally of the pion-nucleon interaction. Whether or not this is a valid description is not relevant to the problem at hand, the essential postulate being that isotopic spin is conserved by the strong interactions. The isotopic vector part (z component)

of this current is then

$$J^{em}_{az} = \sqrt{4\pi}\, e\, [\, \bar{\psi}\, \gamma_a \frac{1}{2} \tau_z \psi + i(\phi^* T_z \partial_a \phi - (\partial_a \phi)^* T_z \phi) + \ldots\,] \qquad (5)$$

As discussed above, the pion contribution must be included if the current is to remain conserved. In this form it is easy to generalize to the beta-decay interaction $J^{\beta} \cdot L$ with the replacement $\sqrt{4\pi}e \longrightarrow \sqrt{8}G$ and $z \longrightarrow +$.

$$J^{\beta}_{a+} = \sqrt{8}G\, [\bar{\psi}\, \gamma_a \frac{1}{2} \tau_+ \psi + i(\phi^* T_+ \partial_a \phi - (\partial_a \phi)^* T_+ \phi) + \ldots\,] \qquad (6)$$

where $\tau_+ \; n = p$, $\tau_- \; p = n$,

$$T_{\overline{+}}\, \pi^{\overline{+}} = \sqrt{2}\pi^o, \qquad T_{\underline{+}}\, \pi^o = \sqrt{2}\pi^{\underline{+}},$$

and $$L_a = \bar{\psi}_e \gamma_a \frac{1}{2}(1 + i\gamma_5)\psi_\nu$$

for electron decay. Again the pion term is required if the vector beta-decay interaction current is to be conserved. The most direct test of this expression would then be to look for effects from the pionic interaction. This interaction predicts the decay

$$\pi^- \longrightarrow \pi^o + e + \bar{\nu} \qquad (7)$$

and gives the decay rate unambiguously. The existence of such a decay is not a unique prediction since it should occur anyway by the indirect process

$$\pi^- \longrightarrow (\bar{p} + n) \longrightarrow (p + \bar{p}) + e + \bar{\nu} \longrightarrow \pi^o + e + \bar{\nu}\ . \qquad (8)$$

It has not been possible to compute such a chain decay reliably;

however, if the vector interaction is not conserved, there is no reason for the rate to be that predicted from equation 6. Experimental verification is difficult, however, since the observed decay rate for $\pi^- \longrightarrow \mu + \bar{\nu}$ is about 10^8 times faster (9) than the decay rate for $\pi^- \longrightarrow \pi^o + e + \bar{\nu}$ as predicted from the CVC theory.

Gell-Mann (10) has pointed out that a more accessible test of the theory can be made by looking for deviations in nuclear beta decay due to the pion term in the interaction current. Such a test, derived from the observation that the nucleons have large anomalous magnetic moments due to the charge carried by the pion, is the subject of this work.

The magnetic moments of the proton and neutron are, in units of $\frac{e}{M_p}$, $\mu_p = 2.79$, and $\mu_n = -1.91$. In isotopic spin formalism this result can be written in the form

$$\mu = \frac{1}{2}\left[\left(1 + \mu^S\right) + \left(1 + \mu^V\right)\tau_z\right] \qquad (9)$$

where $\mu^V = 3.70$ and $\mu^S = -0.12$ are the anomalous isotopic vector and scalar magnetic moments.

The pion interaction is purely isotopic vector while the nucleon interaction is partly isotopic scalar and partly isotopic vector. Thus the large difference between μ^S and μ^V is attributed to the contribution from the pion. If the pion did not interact with the electromagnetic field, a crude estimate (11) of μ^V would be to set it equal to $\mu^S = -0.12$.

If the pion indeed carries the beta-decay interaction, then the nuclear-decay contribution from the "anomalous beta-decay moment" should be enhanced by a factor of $(1 + \mu^V) = 4.70$ and such a contribution might be detectable.

Transition Matrix Elements

Historically, beta-decay has been formulated in a language somewhat different from electromagnetism. It is therefore worthwhile to review the correspondence between the two.

The transition matrix element for a nucleon to emit a photon of momentum $\vec{q}$ and polarization ϵ_a is

$$\sqrt{4\pi}\, e \sum \int \psi_f^+ (\vec{r})\, e^{-i \vec{q}\cdot\vec{r}}\, \beta \gamma_a \frac{1}{2} (1 + \tau_z)\, \psi_i (\vec{r})\, d^3 r \qquad (10)$$

where ψ are the 4-component Dirac wave functions, β and γ_a are defined in Appendix A, and Σ symbolizes a sum over the coordinates of all the nucleons. The matrix $\beta\gamma_a$ consists of an even parity piece, 1, and an odd parity piece, $\vec{\alpha}$. It is natural to treat these separately since parity is a good quantum number for nuclear states. The factor $\exp(-i \vec{q}\cdot\vec{r})$ may also be conveniently written as

$$e^{-i \vec{q}\cdot\vec{r}} = \sum_{\ell} (-i)^{\ell} (2\ell + 1)\, j_{\ell} (qr)\, P_{\ell} (\cos\theta) \qquad (11)$$

where $\vec{q}\cdot\vec{r} = qr \cos\theta$ and $j_\ell(qr)$ is the usual spherical Bessel function normalized so that $\lim(x \to 0)\, j_\ell(x) = x^\ell\, [1 \cdot 3 \cdot 5 \cdots (2\ell + 1)]^{-1}$.

Thus the 1 from $\beta\gamma_a$ generates operators characterized by the

series 1, r_i, $(r_i r_j - \frac{1}{3}\delta_{ij} r^2)$, etc., where the leading term of $j_\ell(qr)$ only has been kept to characterize the operator, with the momentum dependence and numerical factors omitted. These terms are coupled to the timelike polarization (Coulomb potential) and correspond to the static multipole interactions of a static electric field with the charge, the dipole moment, the quadripole moment, etc., respectively. The remaining $\vec{a}$ term, when properly coupled with $\vec{r}$ to give operators of definite rotational properties, gives the series $\vec{a}$, $(a \cdot r)_{0,1,2}$, etc., where $(a \cdot r)_0$, for example, stands for the scalar product $\vec{a} \cdot \vec{r}$, $(a \cdot r)_1$ is the vector product $\vec{a} \times \vec{r}$, and $(a \cdot r)_2$ is the tensor product $(\frac{1}{2} a_i r_j + \frac{1}{2} a_j r_i - \frac{1}{3}(a \cdot r)\delta_{ij})$. The matrix element of $\vec{a} \times \vec{r}$, for example, has the selection rules $\Delta J^\pi = 0, 1 (0 \not\rightarrow 0)$ (no) since $\vec{a}$ and $\vec{r}$ both have odd parity. This expansion of $\vec{a} \exp(-\vec{q} \cdot \vec{r})$ contains both the static magnetic interactions and the radiation transition operators. The first term, $\vec{a}$, corresponds both to the El transition operator and to the interaction of the moving charge and its magnetic moment with a static magnetic field. Next $(a \cdot r)_{0,1,2}$ give, respectively, the E0, Ml, and E2 transition operators, together with the spin-orbit and tensor spin forces. This complexity vanishes for beta decay, since the electron-neutrino field is made up of two spin-$\frac{1}{2}$ particles and the selection rules then correspond to emission of either a "particle" of spin zero or one. This feature makes possible the contribution of all of the above terms to the beta-decay transition matrix element.

With these preliminaries we can immediately write down the transition matrix elements for beta decay if we know the correct operator $O^{(\beta)}$. As a result of a now historical series of experimental and theoretical successes (12) dealing first with the establishment of parity nonconservation and then with the elimination of the scalar and tensor interactions as being important contributors to the beta decay interaction, it is now possible to write simply

$$O_{\alpha}^{(\beta)} = G_V \gamma_\alpha - G_A \, i\gamma_\alpha \gamma_5 \tag{12}$$

where G_A is a negative number, hence the lepton interaction is $\gamma_\alpha + i\gamma_\alpha \gamma_5$ with a plus sign. The pseudoscalar term does not play an important role in nuclear beta decay (13) and has not been excluded experimentally for this reason. It is excluded by the theory (8) in lowest order although higher order effects should produce an "induced" pseudoscalar interaction (Appendix D).

The vector beta-decay interaction is thus indistinguishable from the electromagnetic interaction insofar as the form of the transition matrix elements are concerned. The axial vector contribution, $\beta i\gamma_\alpha \gamma_5$, consists of two pieces, $\vec{\sigma}$, even in parity, and $i\gamma_5$, odd in parity. We then construct Table I from inspection, first giving abbreviated transition matrix elements and then the explicit operator to be evaluated. The series of terms starting with 1 and $\vec{\sigma}$ are often called "ordinary" matrix elements while those starting with $\vec{\alpha}$ and $i\gamma_5$ are called "relativistic." These terms are classified according to their

TABLE I

Order	Vector		Axial Vector	
	Ordinary	Relativistic	Ordinary	Relativistic
Allowed	1		$\vec{\sigma}$	
First Forbidden	$\vec{r}$	$\vec{a}$	$(\sigma\cdot r)_{0,1,2}$	γ_5
Second	r^2	$(a\cdot r)_{0,1,2}$	$(\sigma\cdot r)_{1,2,3}$	$\gamma_5\vec{r}$
Allowed	1		$\vec{\sigma}$	
First	$-i\vec{r}\cdot\vec{q}$	$\vec{a}$	$\frac{1}{3}i(\vec{\sigma}\cdot\vec{r})\vec{q}$	$i\gamma_5$
			$\frac{1}{2}i(\vec{\sigma}\times\vec{r})\times\vec{q}$	
			$i(\vec{\sigma}\cdot\vec{r})_{ij}q_j$	
Second	$-\frac{1}{2}R_{ij}Q_{ij}$	$\frac{1}{3}i(\vec{a}\cdot\vec{r})\vec{q}$	$-\frac{3}{10}\sigma_j R_{jk}Q_{ki}$	$\gamma_5\vec{r}\cdot\vec{q}$
		$\frac{1}{2}i(\vec{a}\times\vec{r})\times\vec{q}$	$\frac{1}{3}\epsilon_{ijk}T_{j\ell}Q_{k\ell}$	
		$i(\vec{a}\cdot\vec{r})_{ij}q_j$	$\frac{1}{6}S_{ijk}Q_{jk}$	

where $(\vec{a}\cdot\vec{b})_{ij} = [\frac{1}{3}(\vec{a}\cdot\vec{b})\delta_{ij} - \frac{1}{2}a_ib_j - \frac{1}{2}a_jb_i]$; $R_{ij} = (\vec{r}\cdot\vec{r})_{ij}$;
$Q_{ij} = (\vec{q}\cdot\vec{q})_{ij}$; $T_{ij} = ((\vec{r}\times\vec{\sigma})\cdot\vec{r})_{ij}$; $S_{ijk} = [\sigma_{(i}r_jr_{k)} - \frac{1}{5}\delta_{(ij}\sigma_{k)}r^2 - \frac{2}{5}\delta_{(ij}r_{k)}\vec{\sigma}\cdot\vec{r}]$ with $\sigma_{(i}r_jr_{k)}$ representing $\sigma_ir_jr_k + \sigma_jr_kr_i + \sigma_kr_ir_j$, etc.

"forbiddenness" which is the order ℓ of the retardation expansion (plus 1 for $\vec{\alpha}$ or γ_5), where the parity selection rules are (no) for even order of forbiddenness and (yes) for odd. Zero forbidden transitions are called "allowed."

Nuclear matrix elements are estimated from nonrelativistic wave functions, and consequently it is necessary to reduce the above 4x4 matrices to the 2x2 nonrelativistic form. For the ordinary matrix elements the replacement is immediately $1 \longrightarrow 1$, $\vec{\sigma} \longrightarrow \vec{\sigma}$. The reduction of matrix elements containing $\vec{\alpha}$ and γ_5 is more difficult since these mix the large and small components between four component spinors. The reduction of these two to nonrelativistic form is illustrated in Appendix A. A reduction of particular interest is

$$\frac{1}{2}\ \vec{\alpha} \times \vec{r} \longrightarrow -\frac{1}{2M}\ (\vec{\sigma} + \vec{\ell}), \tag{A5}$$

the familiar operator for the M1 electromagnetic transition. It is just this transition that is important since the anomalous nuclear moments give the modification

$$\vec{\sigma} \longrightarrow (1 + \mu_{anom})\ \vec{\sigma}\ . \tag{13}$$

To look for the presence of the analog μ_{anom} in the beta-decay interaction suggests examination of transitions having the form $\Delta J = 1$ (no). The matrix elements contributing to such a transition are given from Table I to be $\vec{\sigma}$, $\vec{\alpha} \times \vec{r}$, $\gamma_5 \vec{r}$, and $(\sigma \cdot r_2)_1$. In addition, the next term in the expansion of $\vec{\sigma}\, j_o(qr)$ gives $-\frac{1}{6}\ \vec{\sigma}\, r^2 q^2$

which is comparable to $(\sigma \cdot r_2)_1$ and must also be considered. It is next necessary to see how these terms influence the transition rate, spectrum shape, etc.

Spectrum Shape

The complete transition amplitude is

$$\frac{1}{\sqrt{2}} \sum_n \int d^3 r_n \, d^3 r_\ell \, \delta^3(\vec{r}_n - \vec{r}_\ell) \tag{14}$$

$$\times [\psi_f^+(\vec{r}_n) \beta (G_V \gamma_a - G_A i \gamma_a \gamma_5) \tau_+ \psi_i(\vec{r}_n)]$$

$$\times [\psi_e^+(\vec{r}_\ell) \beta (\gamma_a + i \gamma_a \gamma_5) \psi_\nu(\vec{r}_\ell)]$$

where the delta function indicates the very short range of the beta-decay interaction. The plane wave expression for ψ_ν is $u_\nu(\vec{k}) e^{i\vec{k}\cdot\vec{r}}$ and for ψ_e is $u_e(\vec{p}) e^{i\vec{p}\cdot\vec{r}}$. Both the electron and antineutrino are to be outgoing which corresponds to an incoming neutrino with negative k and $\vec{k}$. The integration over $d^3 r_\ell$ is trivial and writing

$$M_a = \sum_n \int d^3 r_n \, e^{-i\vec{q}\cdot\vec{r}} [\psi_f^+(\vec{r}_n) \beta (G_V \gamma_a - G_A i \gamma_a \gamma_5) \tau_+ \psi_i(\vec{r}_n)] \tag{15}$$

the transition matrix element becomes

$$\frac{1}{\sqrt{2}} [\bar{\psi}_e \mathcal{M} (1 + i\gamma_5) \psi_\nu] \tag{16}$$

where $\mathcal{M} = \beta(M_o - \vec{\alpha} \cdot \vec{M})$ and $\bar{\psi} = \psi^+ \beta$. The computation with this expression is illustrated in Appendix A for the allowed matrix element, with the result

$$M^2 = 2G_A^2 |<\sigma_z>|^2 (Wk - \frac{1}{3} \vec{p}\cdot\vec{k}) \qquad (A12)$$

where W is the total electron energy, $\vec{p}$ is electron momentum, and $k, \vec{k}$ represent the same quantities for the neutrino. For high energy electrons this gives the electron-neutrino angular correlation of $(1 - \frac{1}{3} \cos\theta)$ where θ is the angle between the electron and neutrino momenta. One must average over this angle when the experiment is insensitive to the angular correlation, giving simply

$$M^2 = 2G_A^2 |<\sigma_z>|^2 Wk \qquad (17)$$

Table II gives the contribution of each pair of interference terms, normalized to give the allowed contribution unit magnitude. The definitions

$$a = \frac{\frac{1}{-} G_V}{G_A} \frac{2 <\vec{a} \times \vec{r}>}{<\vec{\sigma}>} \qquad b = \frac{<\gamma_5 \vec{r}>}{<\vec{\sigma}>} \qquad (18)$$

$$c = \frac{<3(\vec{\sigma}\cdot\vec{r})\vec{r} - \vec{\sigma} r^2>}{<\vec{\sigma}>} \qquad \text{and } d = \frac{<\vec{\sigma} r^2>}{<\vec{\sigma}>}$$

have been used.

In positron decay the electron and neutrino wave functions are interchanged. This amounts to interchanging $W, \vec{p}$ and $k, \vec{k}$ in the plane wave approximation, and only the sign of the quantity a in definition 18 is changed. Since the allowed-a interference term is linearly dependent on the electron energy, a comparison between an electron and positron spectrum will double the effect while any contribution from

TABLE II
Shape Factor Terms

Interference Term	Shape Factor	Coulomb Correction	Anglular Correlation
Allowed	1	$\eta R\left(\frac{1}{3}\frac{p^2}{W} - 2W\right)$	$-\frac{1}{3}$
a	$\frac{4}{3}a\left(W - k - \frac{m^2}{W}\right)$	$4a\,\xi$	$\frac{4}{3}a(k - W)$
b	$-\frac{2}{3}b\left(W + k - \frac{m^2}{W}\right)$	$-2b\,\xi$	$-\frac{2}{3}b(k + W)$
c	$-\frac{4}{27}\,c\,\frac{p^2k}{W}$	$-\frac{8}{9}\,c\,\frac{pk}{W}\,\xi$	$-\frac{4}{45}\,c(p^2 + k^2)$
d	$-\frac{1}{3}\,d\left(p^2 + k^2 - \frac{2}{9}\,pk\right)$	$\frac{2}{9}\,d(k - 9p)\xi$	$\frac{1}{9}\,d(p^2 + k^2 - 6Wk)$

where $\xi = \frac{Ze^2}{2R}$, $\eta = Ze^2$, R ~ charge radius of the nucleus, and the angular correlation factors multiply $\frac{\vec{p}\cdot\vec{k}}{Wk}$

the other interference terms will cancel in the ratio. The latter cancellation may not be complete, however, if the end-point energies are different for the two decays. What is required then is a mirror decay such as $B^{12} \xrightarrow{\beta^-} C^{12}$ and $N^{12} \xrightarrow{\beta^+} C^{12}$ where the coefficients a, b, c, and d should be very nearly the same for both transitions. These decays in fact are $1^+ \longrightarrow 0^+$, $\Delta T = 1$ with a large end-point energy giving a wide range over which to look for deviations in the spectrum. Figure 1 exhibits the principal features of the decay schemes (14) of B^{12} and N^{12}. Boron^{12}, which has a half-life (51) of 20.4 msec, decays mainly (97 percent) to the ground state of C^{12} with a maximum electron energy of 13,369 Mev. Nitrogen^{12}, with a half-life (51) of 11.0 msec, also decays mainly to the ground state of C^{12}, with a maximum positron energy of 16.43 Mev. The two radionuclides are members of a T = 1 triplet, whose central member is the 15.11-Mev level of C^{12}. The ground states of B^{12} and N^{12} are $J^\pi = 1^+$, while the C^{12} ground state is 0^+. The gamma-decay width of the 15.11-Mev T = 1 level in C^{12} for the ground state transition has been measured by several investigators, and the weighted average (2) of their results is $\Gamma_\gamma = 50 \pm 4$ ev. From Table I we see that the operator responsible for the electromagnetic transition $1^+ \longrightarrow 0^+$ is $\vec{a} \times \vec{r}$. Thus this matrix element for beta decay is given (Appendix B) by Γ_γ and the assumption of charge independence, while $G_A \langle \sigma_z \rangle$ and G_V are derived from the ft values of B^{12} and O^{14} to yield

$$|a| = \left[\frac{3\,\Gamma_{\gamma}\, ft(B^{12})}{4e^2\omega^3\, ft(O^{14})} \right]^{1/2} \qquad (B4)$$

assuming $|\langle 1 \rangle| = \sqrt{2}$ for O^{14}. The ft value of N^{12} is about 13% larger (51) than that of B^{12}, and a slightly better estimate is to use the average ft value of the two. This refinement is slight and the deviation of the ft values from equality, in violation of charge symmetry, does not appear to be an important source of uncertainty, although this difference between the ft values of B^{12} and N^{12} does not seem to be quantitatively understood. The values (7, 14, 16) $ft(B^{12}) = 11,700 \pm 100$, $ft(N^{12}) = 13,300 \pm 300$, and $ft(O^{14}) = 3,075 \pm 10$ give

$$|a| = 2.48 \times 10^{-3}\ \text{Mev}^{-1}. \qquad (19)$$

The expected value of a from the theory is

$$a \sim \frac{(1 + 3.70)}{2M} \frac{G_V}{-G_A} \sim +2.1 \times 10^{-3}\ \text{Mev}^{-1} \qquad (20)$$

which is so close to the value derived from Γ_{γ} that the sign is almost certainly positive. In making this estimate we have neglected the orbital contribution (see Appendix D) and taken $-G_A/G_V = 1.19$.

The theory of beta decay ignoring direct pionic contributions is sometimes called the Fermi theory. Goldberger and Treiman (17) have attempted to estimate the induced contribution due to virtual dissociation of the pion into nucleon-antinucleon pairs discussed previously. Their result is

$$\mu^{V}(F) \sim \frac{1}{15} \mu^{V}(CVC) \tag{21}$$

which leads to the prediction $a \sim 0.64 \times 10^{-3}$ Mev^{-1} in the Fermi theory. If this estimate is reasonable, it should be possible to distinguish between the CVC and Fermi theories.

These are the estimates pertinent to an experimental test of the CVC theory. The following is concerned with estimation of the remaining matrix elements to see if they also give important contributions to the shape factor.

The nonrelativistic limit for $\gamma_5 \vec{r}$ is (Appendix A)

$\frac{1}{2M} [(\vec{\sigma}\cdot\vec{p})\vec{r} + \vec{r}(\vec{\sigma}\cdot\vec{p})]$, and it is somewhat difficult to estimate such a velocity dependent term. A crude estimate is made in Appendix B, yielding

$$b \sim \frac{3}{4M} i \tag{22}$$

Fortunately, the contribution of this term to the spectrum shape is negligible, as can be seen from Table II.

The quantity c must be estimated from a specific nuclear model. The simplest model is the extreme j-j coupling scheme, in which the nucleons fill the shells $S_{1/2}$, $P_{3/2}$, $P_{1/2}$, etc. This simple model gives

$$c = \frac{1}{2} d. \tag{23}$$

A more detailed shell model calculation gives for this ratio the value

0.57d. These calculations are discussed in Appendix B.

In estimating $d = \frac{\langle \vec{\sigma} r^2 \rangle}{\langle \vec{\sigma} \rangle} \sim \langle r^2 \rangle_{radial}$, we can make use of independent experiments (18) on electron scattering from C^{12}, which give a root-mean-square charge radius of 2.37 f. The decay takes place from the P-shell, while the charge distribution includes also the S-shell. The decaying nucleons then contribute to $\langle r^2 \rangle_{radial}$ more effectively and give

$$d = \langle r^2 \rangle_{decay} = \frac{15}{13} \langle r^2 \rangle_{charge} = 6.48 \text{ f}^2 . \qquad (24)$$

This estimate is discussed in Appendix B, along with an evaluation of other radial matrix elements of interest.

The contributions to the shape factor from $\gamma_5 \vec{r}$, $(\vec{\sigma} \cdot \vec{r})\vec{r}$, and $\vec{\sigma} r^2$ are the same for positron and electron decay, and consequently should cancel when mirror decays are compared. This is not exactly true when the end-point energies of the two (mirror) decays are unequal, since the electron and neutrino energies are related by $W + k = W_o$. Substituting this relation in Table III gives, for example, a contribution $-\frac{1}{3}\left(W_o^2 - \frac{20}{9} W W_o + \frac{20}{9} W^2\right)$ from the allowed-d interference term. The W_o^2 piece gives an insignificant change in normalization while the W^2 piece is independent of an end-point energy difference. The remaining piece is linearly dependent on the beta-particle energy and gives a factor $1 + \frac{20}{27} \delta W_o \cdot W = 1 + \delta A \cdot W$ multiplying the ratio of the shape factors for two mirror decays of maximum energy W_o and $W_o + \delta W_o$. A similar term is derived from the allowed-

c interference term, giving altogether $\delta A = \frac{4}{27}\,\delta W_o(5\,d\text{-}c) \sim +0.04$ percent per Mev for the B^{12}/N^{12} ratio. Since this simulates the CVC prediction, this quantity must be subtracted from the experimental results.

Coulomb Corrections

Use of the plane wave approximation neglects the distortion of the electron wave functions by the Coulomb field of the nucleus. In the A = 12 decays, these corrections should be small, as the decay energy is large compared to the Coulomb energy near the nucleus. They are important, however, since they change sign when going from electron decay to positron decay, and hence contribute spectral deviations analogous to weak magnetism. These corrections have been included in Table II, and a technique of derivation is given in Appendix C. Note that the most important terms (of order ξ) can be obtained from the $\xi = 0$ expressions by simply replacing $W \longrightarrow W + 3\xi$, $k \longrightarrow k$, where $\xi = \frac{Ze^2}{2R}$. This can be understood in the following manner: since the electron at the nucleus is in the potential well of the Coulomb interaction, it behaves to first order as if it had an energy $W + e\bar{V}_c$ where $\bar{V}_c$ is some effective constant potential simulating the actual Coulomb potential of the nucleus. If the nucleus is viewed as a uniformly charged sphere of radius R, then the potential at the center is just 3ξ. The net effect of Coulomb corrections is given to be a contribution to the shape factor of $1 + \delta A_{Coulomb} \cdot E$. Gell-Mann and Berman (19) have carefully computed this quantity and report

$\delta A_{Coulomb} = -0.21$ percent per Mev.

Inner Bremsstrahlung

The possibility that one or more photons are emitted in the course of the nuclear beta decay results in electrons being shifted from the high energy end of the beta spectrum towards the low energy end. This distortion of the spectrum must be factored out if the true shape is to be determined. Expressed as a multiplicative factor to be applied to the observed spectrum, the correction for inner bremsstrahlung (20) is $f = 1 - \delta$ with

$$\delta = \frac{e^2}{2\pi}\left[4(x-1)\ln\left(\frac{W_o - W}{W}\right) + \left(x - \frac{4}{3}\right)\frac{W_o}{W} + \frac{x}{6}\left(\frac{W_o}{W}\right)^2 - \frac{43}{6}x + B\right] \qquad (25)$$

where $x = \frac{1}{2}\frac{W}{p}\ln\left(\frac{W+p}{W-p}\right)$, W = total electron energy, W_o = total end point energy, p = electron momentum, and B is a collection of terms which, being independent of W, do not affect the spectrum shape. This correction is tabulated in Table III as a function of energy for B^{12} and N^{12}, normalized to unity at 8-Mev.

Predictions

Altogether, the prediction is that the shape factors of B^{12} and N^{12}, corrected for inner bremsstrahlung, should exhibit in their ratio a linear dependence on the beta-particle energy of

$$\frac{|M(B^{12})|^2}{|M(N^{12})|^2} = 1 + (A + \delta A)E \qquad (26)$$

TABLE III

The Inner Bremsstrahlung Correction, f(E)

E(Mev)	$f(E, B^{12})$	$f(E, N^{12})$
5.0	.9840	.9850
5.5	.9868	.9878
6.0	.9894	.9904
6.5	.9921	.9929
7.0	.9947	.9953
7.5	.9974	.9977
8.0	1.0000	1.0000
8.5	1.0028	1.0022
9.0	1.0056	1.0046
9.5	1.0086	1.0068
10.0	1.0118	1.0092
10.5	1.0154	1.0117
11.0	1.0192	1.0141
11.5	1.0237	1.0167
12.0	1.0277	1.0194
12.5	1.0369	1.0223
13.0	1.0499	1.0253

where $A = \frac{16a}{3} = 1.35 \pm 0.07$ percent per Mev (0.35 in Fermi theory) and δA is the net correction (19) from Coulomb effects and end-point energy differences = -0.25 ± 0.15 percent per Mev, giving

$$\begin{aligned} A + \delta A &= 1.10 \pm 0.17 \text{ percent per Mev (CVC)} \\ &\sim 0.10 \quad\quad \text{percent per Mev (F)} \end{aligned} \tag{27}$$

No important contributions to the mean shape factor are expected, since the only significant terms are c and d whose corrections to the shape factor slope are small and vanish near 8 Mev.

It should be emphasized that this prediction follows directly from the CVC hypothesis and, except for determination of the sign of A, does not depend (10) on such details as the explicit nonrelativistic form of the matrix elements, etc.

The possibility of terms in the beta-decay interaction in addition to V and A is discussed in Appendix D.

II. APPARATUS

The beta spectra of B^{12} and N^{12} were analyzed with an iron-free single-lens magnetic spectrometer directly connected to a 3-Mev Van de Graaff accelerator. The B^{12} was produced in the reaction $B^{11}(d,p)B^{12}$, and N^{12} was produced in the reaction $B^{10}(He^3,n)N^{12}$. Both targets were located at the object point of the spectrometer. The deuteron and He^3 beams were periodically interrupted at a frequency of 60 cps and the beta particles counted in an anthracene scintillator after suitable delay. The production rate of the activity was monitored by the reaction protons from $B^{10}(d,p)B^{11}$ for B^{12} and $B^{10}(He^3,p)C^{12}$ for N^{12}. A silicon p-n junction counter served as a proton detector.

Spectrometer

The spectrometer used here is essentially that described by Hornyak et al. (21), except the baffle system was modified for the high beta-particle energies involved. This arrangement is illustrated in Figure 2. As can be seen in this figure, all baffles on the counter end of the spectrometer were faced with lucite. The lucite was coated with a conducting layer of carbon to inhibit static charging. To further reduce scattering, the walls of the spectrometer were lined with narrow brass rings to serve as traps for forward-scattered electrons. Similarly, the central brass absorber was machined to have the saw-toothed cross section shown in the figure. The annular momentum-defining slits were of aluminum, shaped so as to permit the minimum possible transmission of particles outside the selected momentum range. The

spectrometer alignment is discussed in Appendix E. The best source and counter position could be determined to within 0.3 mm, while the final experimental arrangement was quite insensitive to such small displacements. The targets were positioned by use of a pointer that could be moved to a standard fixed point in space perpendicular to the spectrometer axis, and could be moved along that axis. It was possible to then locate a specified point on a target within about 0.5 mm of the source-detector axis and 0.2 mm along the axis. With a calibrated Bi^{207} source, kindly supplied by Dr. F. Boehm, the transmission was experimentally determined to be 0.85 percent and the resolution to be 1.5 percent. Energy calibration was accomplished using the conversion lines (22) of Cs^{137} (3381.1 gauss-cm), Bi^{207} (2838.9 and 4657.6 gauss-cm) and the F, I, L, M, and X lines of thorium deposit (1388.4, 1753.9, 2607.2, 2891, and 9986.7 gauss-cm). The magnet current was measured in terms of the voltage drop across a 5 milliohm shunt, and the voltage at which a given conversion line is observed, divided by the magnetic rigidity, should be a constant of the spectroeter. Figure 3 shows the observed values of this ratio plotted as a function of the conversion line energy. This constant was derived from a least-squares fit to the assumed relation

$$I = A \cdot H\rho + B \tag{28}$$

where I is the magnet current measured as stated above and $H\rho$ is the

magnetic rigidity in kilogauss-cm, with the result A = 11.965 ± .005 millivolts per kilogauss-cm. The quantity B was found to be negligible (.0015 millivolt). The calibration data was also fitted to the relation

$$\frac{I}{H\rho} = A' + B' \cdot H\rho \qquad (29)$$

to test for nonlinearities due to nearby iron construction beams, etc. This gave A' = 11.963 ± .005 millivolt per kilogauss-cm and B' = .0003 millivolts per kilogauss-cm per kilogauss-cm. Such a nonlinearity would not be an important source of uncertainty, since the rigidities of interest in this experiment are below about 40 kilogauss-cm. A second shunt was employed for the high field work (>2 Mev) which had a nominal resistance of 0.67 milliohms. The two were calibrated against each other and found to have resistances in the ratio 0.13358 ± .00003. The earth's magnetic field was reduced to less than 1/10 of its ambient value in each axis of the spectrometer by using three orthogonal sets of compensating coils.

Beta Detector

The beta-particle detector consisted of a 10-mm thick, 38-mm diameter anthracene crystal mounted on a 90-cm long lucite light pipe leading to an RCA 6292 photomultiplier tube. The tube was shielded from the stray magnetic field of the spectrometer by three mu-metal layers wrapped directly on the photomultiplier tube and two concentric

cylinders of soft iron. An 0.5-mg/cm^2 aluminum window covered the crystal. The effect of the magnetic field on the photomultiplier was checked using a Po^{210} source and a thin CsI crystal. The line shift was less than one percent in energy between zero and the maximum field used in this experiment. No change in shape or area of the pulse-height distribution was observed. The ratio of the average counting rate for the zero field divided by the maximum field gave $1.0006 \pm .0030$.

The pulse-height distributions recorded on a 100-channel analyzer for two ranges of beta-particle energies are displayed in Figure 4 and Figure 5. It may be observed in Figure 5 that the high-energy electrons give nearly identical pulse-height distributions for energies above 5 Mev. The "double-peaked" distributions at the lower energies are discussed by Porter et al. (23). The lower energy peak is ascribed to electrons that pass through the crystal, while the second peak represents electrons that are scattered through large angles within the crystal and hence stop in the crystal. Below 2.3 Mev, the energy of electrons having a range equal to the crystal thickness, all of the electrons stop in the crystal and hence the two peaks merge into a single peak. At very high energies it is unlikely that an electron will stop in the crystal, and one again observes only a single peak.

The pulse-height distributions were continuously monitored during the actual runs, and the total count was recorded by a scaler which counted all pulses above a given channel. Figures 6 and 7 are

experimental pulse-height distributions of 8-Mev beta particles from B^{12} and N^{12} including background. The background was separately determined from measurements at zero field and high ($>E_{max}$) field. To estimate the number of real counts below channel 21 in Figure 6 we assume, from the near constancy of the difference between the background and 8-Mev counts, that this number is reasonably given by the number of real counts in channels 10 to 30. We then find that about 0.6 percent of the true counts fall below the discriminator level at 8 Mev. The same number is obtained from the observed distribution of 5-Mev and 10.5-Mev B^{12} electrons. Since this quantity does not appear to be energy dependent, no correction is necessary for these counts.

The approximately uniform intensity of small pulses over a large channel spread, as seen in Figure 6, is significant for another reason. The channel in which a pulse appears is, for high-energy electrons, directly proportional to the path length of the electron in the crystal. The only part of the pulse-height spectrum inaccessible corresponds then to the very short path lengths. Any backscattered electrons not seen in the tail must either lose enough energy to produce a pulse larger than the tail pulses and thereby be counted, or be scattered within a very shallow depth of the crystal. Only the latter can be lost and need to be examined in more detail. If the intensity in channel 10 is assumed to consist entirely of such backscattered electrons, then an upper limit to the total backscattered intensity lost may

be calculated from the data, as illustrated in Appendix F, to be approximately 0.90 percent at 5 Mev and 0.96 percent at 11.5 Mev.

The energy loss spectrum of high energy beta particles should be given approximately by the Landau curve (24) and this has been verified experimentally (25). Figure 8 shows the pulse height spectrum of 8-Mev electrons from B^{12} decay, together with a Landau curve having the same full width at half maximum and normalized to the same scale. The observed width (30%) is slightly larger than that given from folding together the theoretical (25) width (15%) and the natural width (15%) of the crystal-photomultiplier-electronics system, the latter being obtained from the 2.2 Mev data where the electrons all stop in the crystal. The Landau analysis does not, however, include angular deviations due to scattering, and in this sense the crystal is actually not sufficiently thin to be rigorously described by this analysis.

The possibility of using a scintillator thick enough to stop all electrons was also examined experimentally, but rejected on the ground that the increased volume led to greatly increased sensitivity to room background, due largely to x-rays from the accelerator, and stray neutrons originating in the target. The pulse-height distributions of Figures 9 and 10 exhibit test runs with a 100-mm long, 50-mm diameter NE-102 plastic scintillator. The relatively large background of small pulses, particularly evident in the N^{12} curves of Figure 10, makes the precise determination of the number of real counts

excessively difficult.

Proton Detector

The reaction protons from the target were monitored as a measure of the number of active nuclei produced. Since the gating cycle is fixed and the beam pulse fluctuations average out, the total number of protons divided by the total duration of the run (clock time) is then directly proportional to the average activity. A silicon p-n junction counter was used to detect the protons. This counter was located inside the spectrometer near the target, as shown in Figure 2. For the B^{12}-reaction monitor, the protons from $B^{10}(d, p)B^{11}$ leading to the ground state (Q = 9.2 Mev) were detected after absorbing the lower energy protons in 118 mg/cm^2 of aluminum. For the N^{12}-reaction monitor, the protons from $B^{10}(He^3, p)C^{12}$ leading mainly to the first excited state (Q = 15.3 Mev) were detected after passing through 344 mg/cm^2 of aluminum. The pulse-height distributions were monitored on a multichannel analyzer. A typical B^{12}-proton spectrum is shown in Figure 11. No field dependence of the proton spectra could be detected (less than one percent in energy) between zero and the maximum magnetic field. The solid angle subtended by the proton counter amounted to 0.7 percent of the sphere. The protons must travel about 1.2 cm perpendicular to the magnetic field direction to reach the proton detector and when 10-Mev electrons are focussed, the magnetic field in the vicinity of the proton detector is about 200 gauss. The protons struck the detector within about 10 degrees from the normal,

consequently the field dependence due to curvature of the proton trajectory was less than 0.001 percent per Mev. The independence of the proton counting rate was also tested by examining the proton counting rate vs. magnetic field during a B^{12} run in which the beam current was exceptionally stable. This analysis gave an energy dependence of -0.1 ± 0.3 percent per Mev consistent with the expected independence.

Circuitry

Figure 12 shows a block diagram of the detection system. The beam is on for 8.3 msec and off for 8.3 msec; the "beam-off" signal triggers the gate generator which, after a delay of 1 msec, turns on the beta-particle scaler for 5.25 msec. The total counting time is monitored by simultaneously counting the oscillations from a 20-kc quartz oscillator. The pulse-height distributions from the beta-particle and proton detectors were monitored and recorded on multichannel analyzers. The "coincidence" scaler checks the operation of the gate generator by recording a count if the beam and beta-particle scaler are on simultaneously. This and the total number of gate pulses were monitored as a check. The average coincidence rate was about one per hour for the data analyzed in this experiment. It is difficult to determine the source of such rare events; however, this coincidence rate gives an infinitesimal increase in the background and is quite unimportant to the experiment. All the scalers were simultaneously turned on and off by an external timer unit not shown in the figure.

Targets

The targets consisted of approximately 0.3 mg/cm^2 of boron on foils of thickness 0.5 mg/cm^2 and 3 mg/cm^2 for B^{12} and N^{12}, respectively. The B^{12} spectrum was also taken using the thicker 3 mg/cm^2 backing. No influence on the shape factor was found for the energies considered here. The boron was deposited on the foils by heating them in a low pressure atmosphere (less than 15-mm Hg) of diborane gas (26). This heating was accomplished by focusing the image of an arc light on the foil which was mounted in a frame of 1.5-mil aluminum. The physical arrangement for maintaining this environment is schematized in Figure 13, and Figure 14 shows the foil mounting. The diborane was frozen with liquid nitrogen and the entire system evacuated. While the target was exposed to the arc light, the system was isolated from the vacuum system and the liquid nitrogen removed, allowing the diborane to melt and vaporize. After deposition the diborane was refrozen and the residual hydrogen pressure, proportional to weight of boron deposited, read from the manometer. This system was calibrated by weighing (before and after deposition) a preheated target on a microbalance. The calibration was performed twice with identical results. Best results were obtained by preheating the target foil for 30 sec before deposition. The boron was deposited as a shiny black layer entirely on the nickel foil. Failure of successive depositions to adhere strongly together with limits on the

heating time (aluminum foil buckles) and diborane pressure (convective heating decomposes the gas) limits this particular scheme to relatively thin target layers. For the B^{12} the foils were 5000 Å nickel, and for the N^{12} they were 500 Å nickel on 3 mg/cm^2 copper backing. This backing enabled the target to withstand the strong He^3 beam in the N^{12} experiment, while the boron deposit adhered better to the nickel. Natural boron (19 percent B^{10}; 81 percent B^{11}) targets were used for the B^{12} and enriched boron (96 percent B^{10}; 4 percent B^{11}) for the N^{12}.

Bombarding Conditions

The beam from the electrostatic accelerator was magnetically analyzed and brought into the spectrometer to give a beam spot 2-mm square. The size and position of the beam spot were insensitive to changes in the spectrometer field, and it was not necessary to reposition the beam spot for each beta-particle energy. 1.65-Mev deuterons at a beam current of 0.2 μa were used for the B^{12} and 2.75-Mev He^3 ions at 2-3 μa for the N^{12}. The beam was chopped at the ion source by periodically turning off the RF voltage. The possibility of an HD^+ contamination of the beam, which could produce a B^{12} activity in the N^{12} experiment, was examined by bombarding a natural boron target with a 1.00-Mev He^3 beam.

The $B^{11}(d,p)B^{12}$ cross-section is comparable at this bombarding energy to that at 1.65 Mev, while the $B^{10}(He^3,p)N^{12}$ becomes quite small. Together with the change in target composition, this should

reduce the counting rate to the background value except for B^{12} activity produced by beam contamination. The resultant counting rate was essentially equal to the old background, and from the uncertainty in the background counting rate it was concluded that less than 8×10^{-4} electrons were produced per positron at the 2.75-Mev bombarding energy on the enriched target. Possibility of such contamination could in principle have been eliminated by passing the beam through a stripping foil before it was magnetically analyzed, since any known charged ion containing deuterium would be separated from He^{3++}. Unfortunately, the beam current necessary to produce a reasonable N^{12} activity exceeded by an order of magnitude the current that the foil (100 Kev thick carbon) could withstand.

III. EXPERIMENTAL PROCEDURE AND RESULTS

The spectra were sampled at 0.5-Mev intervals in the range 5 to 15 Mev for B^{12} and 2.5 to 18 Mev for N^{12}, the data being collected at alternating high and low-energy points to minimize effects of target deterioration and instrumental drifts. Each data point consisted of the number of beta-particle counts divided by the number of proton counts and by the "live" counting time, determined by the 20-kc oscillator. All points were taken with a fixed total duration (clock time) of 3 min for B^{12} and 10 min for N^{12}.

Figure 15 presents the observed counting rates as a function of energy. These rates have been normalized as indicated above, but have not been corrected for background or adjusted for the variable momentum interval accepted by the spectrometer. Typical counting rates obtained at 8-Mev beta energy were approximately 40,000 electrons/min and 120,000 protons/min for B^{12}, 600 positrons/min and 600,000 protons/min for N^{12}. Typical background corrections at 8 Mev amounted to about 1.7 percent for B^{12} and 4.2 percent for N^{12}.

The background was studied at spectrometer settings above the end points of the beta spectra, at zero field, and with blank targets. To simulate the effects of neutrons produced during the bombardment periods, separate studies were made with a beryllium target bombarded by deuterons, examining the background in the normal counting cycle.

The counting rate with the beryllium target, which combined the effects of neutrons and general background due to the accelerator, was independent of the spectrometer field setting. In the B^{12} experiment, about one-fourth of the 1.7 percent background could be accounted for by neutron and general background, and the remainder, about 1.2 percent at zero field and 1.6 percent at high field, must be attributed to scattered electrons and/or bremsstrahlung within the spectrometer. The fact that high and zero field were roughly equal suggests the latter as the more plausible. For N^{12} the yield was much smaller and bombarding energies much higher, consequently the neutron and general background were increased by a factor of ten. Thus, after subtracting the neutron and general background, about 1.7 percent remained of the 4.2 percent N^{12} background. This remaining N^{12} background, about 1.6 percent at zero field and 1.8 percent at high field, has a magnitude and variation comparable with the residual B^{12} background which tends to confirm scattering and/or bremsstrahlung as a common background source. In the B^{12} experiment, the variation of the background was studied up to 5 Mev beyond the B^{12} end point and showed little dependence upon the field. Both spectra were investigated over a region symmetrical about the maximum counting rate, hence an error in the background subtraction leads to a slight curvature of the observed shape factor, but virtually no change in the least-squares fit to a straight line.

In the spectrum studies, particular attention was given to the

regions 5 to 10.5 Mev for B^{12} and 5 to 13 Mev for N^{12}. The lower limit of 5 Mev was dictated by uncertainties introduced by branching to excited states of C^{12}--indicated by arrows on Figure 15--and the upper limits were held well below the spectrum end points to minimize the effect of uncertainties in calibration and background subtraction. The data for the relevant ranges are exhibited in Table IV, in terms of counts per unit momentum interval, corrected for background, as a function of magnetic rigidity. The indicated standard deviations represent combined uncertainties from statistics and background subtraction.

Results

The measured momentum distributions for B^{12} and N^{12} are tabulated in Table IV; the Fermi plots of this data are exhibited in Figure 16. The end points obtained from this experiment are, for B^{12}, $13.381 \pm .041$ Mev and for N^{12}, $16.36 \pm .21$ Mev, to be compared with values of $13.369 \pm .001$ and $16.43 \pm .06$ Mev, respectively (27, 28), as determined from reaction data.

We first consider the analysis of the B^{12} data. The derivation of the shape factor requires correction for branching to excited states of C^{12}. The end points of these beta-decay branches are known from the level structure of C^{12} and are indicated by arrows in Figures 15 and 16. Thus, to construct $S(E, B^{12})$, we first subtract from the observed momentum spectrum the simple ideal Fermi spectra corresponding to these branches. To accomplish this, we first need the f values given

TABLE IV

Momentum spectra of B^{12} and N^{12}. Correction for background has been made. Second number indicates combined uncertainty due to background and statistics. The electron momentum is symbolized by η.

$B\rho$(Kg-cm)	$N(\eta, B^{12})$	S.D.	$N(\eta, N^{12})$	S.D.
9.898			3649	87
11.587			3903	87
13.270			4631	87
14.950			4980	86
16.628			5748	82
18.302	2898	23	6119	30
19.976	3076	11	6657	31
21.650	3171	10	6998	33
23.323	3212	9	7212	33
24.994	3198	8	7466	35
26.665	3085	7	7503	35
28.336	2933	7	7477	36
30.023	2722	6	7369	36
31.676	2455	6	7215	28
33.346	2139	5	6912	25
35.017	1794	6	6443	29
36.687	1433	6	6066	25
38.355	1061	6	5634	25
40.025	721	6	5021	21
41.696	415	7	4390	19
43.363	183	7	3711	16

TABLE IV (continued)

Bρ(Kg-cm)	$N(\eta, B^{12})$	S.D.	$N(\eta, N^{12})$	S.D.
45.033	38	5	2998	13
46.704			2413	33
48.373			1804	29
50.042			1158	23
51.711			678	17
53.380			260	14

by the integral $\int_1^{w_o} F(z,w)\phi(w_o,w)dw$, where w is the total electron energy divided by the electron mass, w_o is the maximum decay energy in these units, and $\phi(w_o,w) = w(w_o-w)^2(w^2-1)^{1/2}$. The integrand is tabulated in Table V for the transitions of B^{12} and N^{12}. For high energies $F(Z,w) \longrightarrow$ constant and the integral yields

$$f \sim F(Z,\infty)\left[\frac{1}{60}(w_o^2-1)^{1/2}(2w_o^4-9w_o^2-8)+\frac{1}{4}w_o \ell n(w_o+\sqrt{w_o^2-1})\right]. \quad (30)$$

This result was then corrected by numerically integrating $\int_1^{w_o}[F(Z,w)-F(Z,\infty)]\phi(w_o,w)dw$ using the tabulated (29) values of $F(Z,w)$. The resultant f values are included in Table V. The branching fraction to the i^{th} state is given by $a_i f_i/f_T$ where $f_T = \sum_i a_i f_i$ where a_i is the magnitude of the transition matrix element to the i^{th} state. Here we can normalize $a_o = 1$ for the ground state transitions and neglect the other f_i relative to f_o, then $a_i = \frac{f_o}{f_i} \times$ (experimental branching fraction). The branching fractions for the 4.4 and 7.6-Mev levels have been measured (15, 30, 31) to be 1.3 ± 0.1 and 1.3 ± 0.4 percent, respectively. The ground state spectrum is then given by multiplying the observed spectrum by $\phi(w_o,w)/\sum_i a_i\phi(w_i,w)$. Thus the shape factor $S(E,B^{12})$ is obtained from the spectrometer data (after background correction) by dividing by $F(Z,w)(w^2-1)^{1/2}\sum_i a_i\phi(w_i,w)$ where the factor $(w^2-1)^{1/2}$ adjusts for the variable momentum interval seen by the spectrometer. Note that the ft value of the branch to the first excited state is an order of magnitude less than the ground state

TABLE V

The Function $F(Z,w)\phi(w_o,w)$

	B^{12}			N^{12}		
E(Mev)	G.S.	4.43	7.6	G.S.	4.43	7.66
5.0	9270	2055	69	13107	4921	1431
5.5	9764	1867	8	14281	5057	1283
6.0	10060	1603		15277	5063	1084
6.5	10146	1282		16075	4940	846
7.0	10019	932		16649	4690	592
7.5	9686	585		16998	4320	349
8.0	9156	283		17108	3862	147
8.5	8455	70		16998	3322	22
9.0	7582			16614	2719	
9.5	6593			16021	2095	
10.0	5516			15212	1482	
10.5	4395			14206	918	
11.0	3280			13024	449	
11.5	2228			11695	125	
12.0	1302			10252		
12.5	571			8731		
13.0	114			7178		
f(G.S.)	560,275			1,152,648		
f(4.43)		81,468			252,527	
f(7.66)			9,945			56,388
log ft(expt)	4.068			4.126		
		5.105			5.062	
			4.195			4.314

transition; consequently the contribution is not as strong as suggested by Table V. No attempt is made to include possible spectral deviations in the branches themselves, as the error so introduced should be negligible. Finally, the correction for inner bremsstrahlung, $f(E,B^{12})$ from Table III, is applied to give the shape factor, Sf, which is found, as shown in Figure 17, to exhibit a linear energy dependence of 1.82 ± 0.09 percent per Mev. The error (standard deviation) cited derives from the uncertainty in the least-squares fit of a straight line to the data.

For the N^{12} data, additional complications enter since only the branching fraction to the 4.4-Mev state of C^{12}, 2.4 ± 0.2 percent (15), has been measured with precision. Vedder (16) has analyzed the Fermi plot of N^{12} into linear components using reaction data end points and reports a 3 percent branch to the 7.6-Mev level, but no uncertainties were reported. The branching fraction to the 7.6-Mev state can be estimated to be about 4.0 ± 1.3 percent from the mirror branching fractions in B^{12} quoted above and the approximation of charge symmetry. The large uncertainties in this branching fraction, introduced by the uncertainty in the mirror branching fraction and by the deviation (15) of the first two branches from the charge symmetry assumption, then give correspondingly large uncertainties in the form of $S(E,N^{12})$ below 8.5 Mev. For this reason the data has been analyzed to see if a better value for this branching fraction can be determined. This

involves decomposing a complex beta-decay spectrum into the separate branches. In principle, the decomposition can be realized by constructing a best fit to the linear portion of the Fermi plot near the end point of the most energetic transition which is then subtracted from the data. This procedure is repeated until either the decomposition is complete or the remaining data after extraction of the n^{th} branch is no longer adequate due to the experimental uncertainties in the data compounded with the uncertainties introduced by each subtraction. For the N^{12} spectrum, many of these uncertainties are avoided by using the branching fraction and end point of the 4.4-Mev branch which are known from independent experiments. Furthermore, the end point of the 7.6-Mev branch is also known from the reaction data so that the problem would actually be over-determined were it not for the fact that the precise shape of the ground-state transition is not known. In fact, it is just this shape that is to be measured! Advantage of this overdeterminacy is taken by introducing a shape factor of the form $(1 + aE)$ into the ground-state spectrum and demanding agreement between the reaction data end point of the 7.6-Mev branch and that found by the subtraction procedure indicated above. The Fermi plots for two assumed values of the quantity a are shown in Figure 18. These results are shown in Figure 19 where each datum is treated as a point in a plot of assumed ground state end-point energy

versus the branching end-point energy obtained from Fermi plots such as Figure 18. Lines of constant branching fractions then may be inferred and the uncertainty in the branching fraction determined by projecting the uncertainties in the two energies parallel to these lines. A similar graph was used to analyze the value and uncertainty in the quantity a. In this fashion the quantity a is found to be 0.6 ± 0.3 percent per Mev and the 7.6-Mev branching fraction is 3.0 ± 0.4 percent where the uncertainties are derived from the uncertainties in the various branching end points, in the 4.4-Mev branching fraction and in the statistical scatter of the data itself. This value of 3.0 percent for the 7.6-Mev branching fraction, along with the other known branching data, is now used to determine $S(E,N^{12})f(E,N^{12})$ which is plotted in Figure 17.

It is readily apparent that the shape factors shown in Figure 17 differ appreciably from one another; the N^{12} shape factor rises with a slope of 0.60 ± 0.08 percent per Mev, while the B^{12} rises with a slope of 1.82 ± 0.09 percent per Mev. Comparing the two slopes, one finds 1.22 ± 0.13 percent per Mev for the experimental value of the factor $A + \delta A$. The uncertainties quoted above are from the statistical scatter of the data alone. Other uncertainties, including that introduced from the branching fraction estimated above, are discussed below. The effect of the uncertain 7.6-Mev branching fraction can be avoided, at the expense of precision, by using the N^{12} data for

positron energies greater than 8.0 Mev only. The least-squares fit to this limited portion of the shape factor, which is insensitive to the 7.6-Mev branch, yields an energy dependence of 0.52 ± 0.20 percent per Mev and, consequently, a value of 1.30 ± 0.22 percent per Mev for $A + \delta A$.

Errors and Corrections

The sensitivity of the spectrometer to source misalignment has been checked by deliberately placing a Bi^{207} source off axis and also by moving the beam spot 2 mm on the target. Figure 20 shows the effect of such displacement. Such a misalignment is over ten times what we would reasonably expect during the experiment. Another test was made by displacing the beam spot 2-mm during an actual B^{12} run. The shape factor derived from this data was in agreement with that obtained with the beam spot properly centered.

If the upper limit of the HD^{+} impurity in the He^{3} beam were accepted as being present, then the $A + \delta A$ result would be decreased by 0.02 percent per Mev.

In analysis of the data the effect of a change in duration of the counting cycle increasing (for example) the number of beta-particle counts was compensated by dividing by the "live" counting time. This compensation is imperfect due to the decay of the activity. In the experiment, the activity decayed by about 20% during the counting cycle and the "live" time was observed to wander about one percent

between consecutive data points, so an error of about 0.1 percent was expected. This wander was not correlated with the magnetic field strength or the counting rate and the resultant uncertainty was unimportant compared to statistical fluctuations in the total number of beta-particle counts. Corrections for dead time were made for each experiment. Although the proton counting rate was high, only the differences between the average counting rate and the individual counting rates entered in computing the relative corrections for dead time. The proton counts were recorded on Eldorado SC-700 scalers having a dead time of about 1.2 μsec, and the relative dead time corrections amounted, in the N^{12} experiment, to about 0.5 percent with an uncertainty of the order of 0.1 percent. This uncertainty, as with uncertainty introduced above by the gating cycle fluctuations, is uncorrelated with the beta-particle energy and has therefore already been folded into the uncertainty in the least-squares fit to the shape factors.

The uncertainty due to the residual component of the earth's magnetic field is completely negligible at these energies.

In the energy region studied, an error of a constant amount in the background subtraction will lead to a slight curvature of the shape factor but will not essentially change the least-squares fit to the slope. If the background correction is applied assuming that the background has a form $b + cE$ with b and c determined from the high and zero field backgrounds, instead of just averaging the two, then $A + \delta A$ is increased by 0.04 percent per Mev.

The 1.5-kev uncertainty in the actual end-point energy of the B^{12} transition, given from the reaction data, has negligible influence on the B^{12}-shape factor. On the other hand, the 60-kev uncertainty in the N^{12}-end point gives an uncertainty of 0.18 percent per Mev in the N^{12}-shape factor. If only N^{12} data above 8.0 Mev is used, then this uncertainty is increased to 0.27 percent per Mev. A 10-kev error in calibration at 13 Mev gives 0.04 percent per Mev for both B^{12} and N^{12} but these are in the same direction and give almost no error in the value of $A + \delta A$, which is given by the difference between the two shape factors. The recoil energy lost to the C^{12} nucleus varies between about 4 kev at the midpoint of the spectrum to 9 kev at the end point. This virtually cancels in the ratio and in any case is tiny compared to the uncertainty in the N^{12} end-point energy.

The uncertainty in the branching ratios of B^{12} and N^{12} to the 4.4-Mev state of C^{12} is significant only for the N^{12}-shape factor, where it introduces a 0.04 percent per Mev uncertainty unless only data above 8.0 Mev are used, whereby this uncertainty is reduced to 0.01 percent per Mev. The 7.6-Mev branch is unimportant for the B^{12}-shape factor in the energy range considered, but strongly influences the N^{12}-shape factor. The uncertainty in our result for this branching fraction in the N^{12} decay, 3.0 ± 0.4 percent, introduces an uncertainty of 0.14 percent per Mev in the slope of the N^{12}-shape factor.

The beta-particle counting efficiency of the anthracene crystal

may be energy dependent due to backscattering or, in the N^{12} experiment, annihilation in flight of the decay positrons. In both cases, the beta particle must be lost before a sufficient energy has been deposited in the crystal to produce a pulse that will pass the discriminator level. In this experiment such backscattering loss is negligible but the annihilation loss will be significantly greater for the low-energy positrons than for the high-energy positrons and consequently gives the N^{12}-shape factor a spurious slope of approximately 0.06 ± 0.02 percent per Mev with the uncertainty due to variations of the discriminator level among the various N^{12} runs. If the beta particle loses a large fraction of its energy via bremsstrahlung, and the bremsstrahlung quanta are not captured, then it will not be counted. Computation indicates that only about 1 in 10^4 beta particles are so lost with the experimental arrangement used. This computation, along with the estimate of positron annihilation effects, above, are reproduced in Appendix F. Experimentally, the small number of small pulses in the pulse-height distribution testifies to the unimportance of this effect. Annihilation of positrons should also give a contribution to this small-pulse region in the N^{12} experiment, but the statistical accuracy of the data was not sufficient to verify the annihilation correction experimentally.

Finally, we must consider the possibility that beta particles reach the detector by penetrating through the aperture baffle which defines the ring focus and the baffles defining the acceptance solid angle.

Such penetration will effectively increase the accepted momentum interval by a factor of $1 + \alpha E^2$ where α depends upon the geometry and composition of the baffles. This quantity is estimated in Appendix G to be 2.4×10^{-4} (Mev)$^{-2}$, which gives a spurious energy dependence of about 0.38 percent per Mev for each of the two shape factors. In view of the magnitude of this correction, the absolute shape factors must be taken with some reservation. However, the positron penetration is only about 5 percent greater than the electron penetration so the quantity $A + \delta A$ is increased by only 0.02 percent per Mev.

The nonlinearity of this correction requires a re-examination of several points, namely the comparison of the B^{12} and N^{12}-shape factors in slightly different energy regions and the computation of the N^{12} branching fraction to the 7.6-Mev state of C^{12}. It is appropriate here to point out that theoretical estimates (32) of Coulomb, finite nuclear size, and other higher order corrections predict a curvature of the shape factors of the same magnitude but opposite sign. Taken together, the curvatures then essentially cancel, as is suggested experimentally by the B^{12} data. If we suppose that either correction may have been incorrectly estimated by a factor of two, then the existence of these nonlinearities introduces an uncertainty of $\pm$ 0.3 percent in the 7.6-Mev branching fraction and a net uncertainty of $\pm$ 0.16 percent per Mev in $A + \delta A$. If N^{12} data above 8.0 Mev are used, the disparity in energy of the data compared is increased but

the 7.6-Mev branching fraction has no influence, altogether giving an uncertainty of $\pm$ 0.12 percent per Mev. If we select only data in the range 8.5 to 10.5 Mev, which is then free both of uncertainties in the 7.6-Mev branching fraction and in nonlinear effects (since we now can compare data at the same energy and the curvatures then cancel in the ratio), we obtain for A + δA the value 1.30 $\pm$ 0.41.

IV. SUMMARY AND CONCLUSION

The B^{12}-shape factor has an energy dependence of 1.82 ± 0.09 percent per Mev, while the N^{12}-energy dependence is 0.60 ± 0.08 percent per Mev, if the value of 3.0 percent is used for the 7.6-Mev branching fraction, or 0.52 ± 0.20 percent per Mev if only N^{12} data insensitive to this branch are used, giving 1.22 ± 0.13 and 1.30 ± 0.22 percent per Mev, respectively, for $A + \delta A$. The absolute values of the individual shape factors may suffer from important systematic corrections, however these corrections are not expected to appear significantly in the ratio and consequently have small effect on the quantity $A + \delta A$. A value of 1.30 ± 0.41 percent per Mev for $A + \delta A$ results if the analysis is further restricted to data in the energy region 8.5 to 10.5 Mev. The uncertainties are only the statistical standard deviations, and therefore we must include the known systematic errors and corrections discussed in the preceding section and listed in Table VI. This finally yields for $A + \delta A$ the experimental values 1.30 ± 0.31, 1.38 ± 0.37, and 1.38 ± 0.47 percent per Mev. These values are all in agreement with the CVC theory prediction of 1.10 ± 0.17 percent per Mev and not in agreement with the Fermi theory estimate of about 0.10 percent per Mev.

Since the first value has the smallest error and represents the most extensive use of the available data, which is internally consistent in that the quantity a from the branching fraction determination agrees

TABLE VI

Errors (Standard Deviation)

Source	Error in $A + \delta A$ (percent per Mev)		
Statistics	0.13[a]	0.22[b]	0.41[c]
Calibration	0.00		
B^{12} end-point energy	0.00		
N^{12} end-point energy	0.18[a]	0.27[b]	0.22[c]
4.4-Mev branching of B^{12} decay	0.00		
4.4-Mev branching of N^{12} decay	0.04[a]	0.01[b]	0.02[c]
7.6-Mev branching of B^{12} decay	0.00		
7.6-Mev branching of N^{12} decay	0.14[a]	0.00[b]	0.00[c]
Background correction	0.04		
HD^{+} contamination of He^{3} beam	0.02		
Backscattering	0.00		
Annihilation	0.02		
Non-linear corrections	0.16[a]	0.12[b]	0.00[c]
Net Error	0.31[a]	0.37[b]	0.47[c]
Value of $A + \delta A$	1.30	1.38	1.38

[a] Error if 3.0 ± 0.4 percent used for the 7.6-Mev N^{12} branching fraction.

[b] Error if N^{12} data below 8.5 Mev discounted.

[c] Error if B^{12} and N^{12} data compared in energy region 8.5 to 10.5 Mev.

with the observed shape factor slope, we select 1.30 ± 0.31 as being the result of our experiment.

This result strongly favors the CVC theory. Boehm, Soergel, and Stech (33) have found a beta-gamma correlation in the decay $F^{20}(\beta^-)Ne^{20*}(\gamma)Ne^{20}$ with sign and magnitude consistent with estimates from the CVC theory. Nordberg, Morinigo, and Barnes (34) have studied the beta-alpha correlation in the mirror decays $Li^{8}(\beta^-)Be^{8*}(\alpha)He^{4}$ and $B^{8}(\beta^+)Be^{8*}(\alpha)He^{4}$ and find agreement within limits imposed by a shell-model calculation of the relevant M1 matrix element. Precise measurements of the O^{14} decay energy and half-life (7) have established that the beta-decay and muon-decay coupling constants differ by only about 1.8 percent with an uncertainty depending largely on theoretical corrections: Weidenmüller (35) has pointed out that a deviation of this magnitude is consistent with plausible admixing of collective excitations. The analysis of muon capture in C^{12} (36) also appears to support the CVC theory.

At this writing this comparison of the B^{12} and N^{12} is being performed at several laboratories, and even the difficult $\pi^- \longrightarrow \pi^o + e + \bar{\nu}$ branching ratio determination is to be attempted.

There seems to be no anomalous behavior of the second-forbidden axial-vector matrix elements to explain the mean shape factor of 1.18 percent per Mev, which strengthens the possibility that this feature derives from a systematic effect.

It is interesting to note that the relatively strong energy dependence of the B^{12}-transition matrix element accounts for the failure of Hornyak and Lauritsen (37) to observe a B^{12} branch to the 4.4-Mev state of C^{12}, and in fact gives a Fermi plot that is slightly concave downwards, as can be seen in Figure 16.

REFERENCES

1. T. Mayer-Kucuk and F. C. Michel, Phys. Rev. Letters, 7, 167-169 (1961).
2. T. Mayer-Kuckuk and F. C. Michel, to be published.
3. H. Hilton, Ph. D. Thesis, California Institute of Technology (1960), unpublished.
4. A. Lundby, Progress in Elementary Particle and Cosmic Ray Physics (North Holland Publishing Co., Amsterdam, 1960), Vol. 5, pp. 46-50.
5. G. Puppi, Nuovo Cimento, 6, Series 9, 194-199 (1949).
6. O. Kofoed-Hansen and A. Winther, Kgl. Danske Videnskab Selskab, Mat. fys. Medd., 30, Nr. 20 (1956).
7. R. K. Bardin, C. A. Barnes, W. A. Fowler, and P. A. Seeger, Phys. Rev. Letters, 5, 323-326 (1960); and to be published.
8. R. P. Feynman and M. Gell-Mann, Phys. Rev., 109, 193-198 (1958).
9. S. S. Gershtein and J. B. Zeldovich, Zhur. Eksptl. i Teort. Fiz U.S.S.R., 29, 698-699 (1955) (translation: Soviet Phys. JETP 2, 576-578 (1957)).
10. M. Gell-Mann, Phys. Rev., 111, 362-365 (1958).
11. M. Gell-Mann, Lecture Notes on Theoretical Physics, California Institute of Technology (1958-1959), pp. 301-321.

12. E. J. Konopinsky, Annual Reviews of Nuclear Science (Annual Reviews Inc., Palo Alto, Calif., 1959), Vol. 9, pp. 99-158.

13. C. P. Bhalla and M. E. Rose, Phys. Rev., 120, 1415-1424 (1960).

14. F. Ajzenberg-Selove and T. Lauritsen, Nuclear Phys., 11, 111-137 (1959).

15. N. W. Glass, R. W. Peterson, and R. K. Smith, Bull. Am. Phys. Soc., 6, 49 (1961).

16. J. F. Vedder, UCRL 8324 (1958).

17. M. L. Goldberger and S. B. Treiman, Phys. Rev., 111, 354-361 (1958); M. L. Goldberger, Revs. Modern Phys., 31, 797-801 (1959).

18. J. H. Fregeau, Phys. Rev., 104, 225-236 (1956).

19. M. Gell-Mann and S. M. Berman, Phys. Rev. Letters, 3, 99-101 (1959).

20. T. Kinoshita and A. Sirlin, Phys. Rev., 113, 1652-1660 (1959).

21. W. F. Hornyak, T. Lauritsen, and V. K. Rasmussen, Phys. Rev., 76, 731-739 (1949).

22. K. Siegbahn, Beta- and Gamma-Ray Spectroscopy (North Holland Publishing Co., Amsterdam, 1955).

23. F. T. Porter, M. S. Freedman, T. B. Novey, and F. Wagner, Jr., Phys. Rev., 103, 921-942 (1956).

24. L. Landau, J. Phys. (U.S.S.R.), 8, 201-205 (1944).

25. E. L. Goldwasser, F. E. Mills, and A. O. Hanson, Phys. Rev., 88, 1137-1141 (1952).

26. J. Overly, Ph. D. Thesis, California Institute of Technology (1960), unpublished.

27. F. Ajzenberg-Selove, M. L. Bullock, and E. Almquist, Phys. Rev., 108, 1284-1288 (1957).

28. F. Everling, L. A. König, J. H. E. Mattauch, and A. H. Wapstra, Nuclear Phys., 15, 342-345 (1960).

29. Tables for the Analysis of Beta Spectra, National Bureau of Standards Applied Mathematics Series, No. 13 (1952).

30. C. W. Cook, W. A. Fowler, C. C. Lauritsen, and T. Lauritsen, Phys. Rev., 107, 508-515 (1957).

31. V. Soergel (private communication) reports, however, a larger value for the B^{12} branching ratio to the 7.6-Mev level of C^{12}.

32. M. Morita, Phys. Rev., 113, 1584-1589 (1959); J. Bernstein and R. R. Lewis, Phys. Rev., 112, 232-238 (1958).

33. F. Boehm, V. Soergel, and B. Stech, Phys. Rev. Letters, 1, 77-79 (1958).

34. M. E. Nordberg, F. B. Morinigo, and C. A. Barnes, Phys. Rev. Letters, 5, 321-323 (1960); and Phys. Rev., 125, 321-330 (1962).

35. H. A. Weidenmüller, to be published.

36. G. Flamand and K. W. Ford, Phys. Rev., 116, 1591-1596 (1959).

37. W. F. Hornyak and T. Lauritsen, Phys. Rev., 77, 160-164 (1950). For further analysis of their data, see N. W. Tanner, Phil. Mag., 1, 47-54 (1956).

38. S. S. Schweber and H. A. Bethe, An Introduction to Relativistic Quantum Field Theory (Row, Peterson and Co., Elmsford, New York, 1961), Ch. 4.

39. L. L. Foldy and S. A. Wouthuysen, Phys. Rev., 78, 29-36 (1950).

40. E. Feenberg, Shell Theory of the Nucleus (Princeton University Press, Princeton, New Jersey, 1955), pp. 141-145.

41. J. P. Elliot and A. M. Lane, Handbuch der Physik (Springer-Verlag, Berlin, 1957), Vol. 39, pp. 317-357.

42. H. A. Weidenmüller, Nuclear Phys., 21, 397-405 (1960).

43. H. A. Jahn and H. van Wieringen, Proc. Roy. Soc. London A209, 502-525 (1951).

44. H. A. Bethe and L. C. Maximon, Phys. Rev., 93, 768-784 (1954).

45. M. L. Goldberger, Phys. Rev., 110, 1478-1479 (1958); and J. C. Taylor, Phys. Rev., 110, 1216 (1958).

46. S. Weinberg, Phys. Rev., 112, 1375-1379 (1958).

47. A. H. Wapstra, G. J. Nijgh, and R. Van Lieshout, Nuclear Spectroscopy Tables (North Holland Publishing Co., Amsterdam, 1959), pp. 40-42.

48. W. Heitler, The Quantum Theory of Radiation, Third Edition (Clarendon Press, Oxford, 1954), pp. 242-275.

49. G. R. White, National Bureau of Standards Report 1003 (1952).

50. F. Rohrlich and B. C. Carlson, Phys. Rev., 93, 38-44 (1954).

51. T. R. Fisher, to be published.

APPENDIX A

Spinology

The Dirac equation is discussed (38) in most books on advanced quantum mechanics, and here we mainly define conventions used in the text. The Hamiltonian for free fermions is written, in momentum space,

$$H\psi = (\vec{\alpha} \cdot \vec{p} + \beta M) = W\psi \tag{A1}$$

where $\vec{\alpha} = \begin{pmatrix} 0 & \vec{\sigma} \\ \vec{\sigma} & 0 \end{pmatrix}$; $\beta = \begin{pmatrix} I & 0 \\ 0 & I \end{pmatrix}$; $\vec{\sigma} = (\sigma_x, \sigma_y, \sigma_z)$, the conventional Pauli spin matrices, and I is the 2x2 unit matrix. Equation A1 is often rewritten in the covariant form

$$(\not{p} - M)\,\psi = 0 \tag{A2}$$

where $\not{p} = \gamma_o W - \vec{\gamma} \cdot \vec{p}$ and $\gamma_o = \beta$, $\vec{\gamma} = \beta\vec{\alpha}$. In this latter notation scalar, vector, tensor, axial vector, and pseudoscalar couplings are $(\bar{\psi}\psi)$, $(\bar{\psi}\gamma_\alpha\psi)$, $(\bar{\psi}\sigma_{\alpha\beta}\psi)$, $(\bar{\psi} i\gamma_\alpha\gamma_5\psi)$ and $(\bar{\psi}\gamma_5\psi)$, respectively, where $\bar{\psi} = \psi^+\beta$, $\gamma_5 = i\begin{pmatrix} 0 & I \\ I & 0 \end{pmatrix}$ and $\sigma_{\alpha\beta} = \frac{1}{2} i (\gamma_\alpha\gamma_\beta - \gamma_\beta\gamma_\alpha)$. So defined, the γ's obey the relations

$$\gamma_\alpha\gamma_\beta + \gamma_\beta\gamma_\alpha = 2\delta_{\alpha\beta}; \quad \gamma_\alpha\gamma_5 = -\gamma_5\gamma_\alpha; \text{ and } \quad \gamma_5\gamma_5 = -1 \tag{A3}$$

The 4-component spinor, ψ, may be written as a 2-component spinor whose elements are in turn 2-component spinors, i.e. $\psi = \begin{pmatrix} \phi \\ \zeta \end{pmatrix}$. The Dirac equation then splits into two coupled equations

$$(W - M)\,\phi = \vec{\sigma}\cdot\vec{p}\,\zeta$$
$$(W + M)\,\zeta = \vec{\sigma}\cdot\vec{p}\,\phi \qquad \text{(A4)}$$

The second equation is the basis of a nonrelativistic approximation, since for small kinetic energies $W + M = E + 2M \sim 2M$, hence $\zeta \sim \frac{1}{2M}(\vec{\sigma}\cdot\vec{p})\phi$ and it is possible then to write everything in 2-component nonrelativistic notation. Since $\zeta \longrightarrow 0$ as $\vec{p} \longrightarrow 0$ while $\phi \longrightarrow$ nonrelativistic spinor, it is customary to call ϕ the "large component" and ζ the "small component." In the extreme relativistic limit they are comparable.

The matrix elements containing $\vec{\alpha}$ and γ_5 can now be reduced to nonrelativistic form by eliminating ζ and using the usual commutation relations $[p_i, r_j] = -i\delta_{ij}$ and $[\sigma_i, \sigma_j] = i\sigma_k$ (ijk cyclic). Thus, for example,

$$\psi_f^{+}(\vec{\alpha}\times\vec{r})\psi_i = (\phi_f^{*}\ \zeta_f^{*}) \begin{pmatrix} 0 & \vec{\sigma}\times\vec{r} \\ \vec{\sigma}\times\vec{r} & 0 \end{pmatrix} \begin{pmatrix} \phi_i \\ \zeta_i \end{pmatrix}$$

$$\sim \frac{1}{2M}\,\phi_f^{*}\left[(\vec{\sigma}\times\vec{r})(\vec{\sigma}\cdot\vec{p}) + (\vec{\sigma}\cdot\vec{p})(\vec{\sigma}\times\vec{r})\right]\phi_i \qquad \text{(A5)}$$

$$\sim -2\,\frac{1}{2M}\,\phi_f^{*}\,(\vec{\sigma}+\vec{\ell})\,\phi_i$$

Similarly,

$$\psi_f^{+}\gamma_5\,\vec{r}\,\psi_i \sim \frac{1}{2M}\,\phi_f^{*}\left[(\vec{\sigma}\cdot\vec{p})\,\vec{r} + \vec{r}\,(\vec{\sigma}\cdot\vec{p})\right]\phi_i\,. \qquad \text{(A6)}$$

Foldy and Wouthuysen (39) give a more consistent method of deducing the nonrelativistic limit which is, however, the same as the above to order $(v/c)^2$.

The necessary relativistic lepton wave functions can be handled easily by trace techniques. Consider the transition matrix $M = \frac{1}{\sqrt{2}} [\bar{\psi}_e \mathcal{M}(1 + i\gamma_5)\psi_\nu]$ where the decay rate (neglecting nuclear recoil) is given by

$$\Gamma_\beta = \int \frac{1}{4(2\pi)^5} |M|^2 \, k p dW \, d\Omega_p \, d\Omega_k \tag{A7}$$

If the polarizations of neither the electron nor antineutrino are observed, then $|M|^2$ can be simplified.

$$|M|^2 = \frac{1}{2} \sum_{\text{spin}}^{e} \sum_{\text{spin}}^{\nu} \frac{1}{\sqrt{2}} (\bar{u}_e \mathcal{M} (1+i\gamma_5) u_\nu) \frac{1}{\sqrt{2}} (u_\nu \beta (1 - i\gamma_5) \mathcal{M}^+ \beta u_e)$$

$$= \frac{1}{4} \operatorname{Tr} [(\not{p} + m) \mathcal{M}(1+i\gamma_5) \not{k} \, \mathcal{M}^* (1 + i\gamma_5)] \tag{A8}$$

since $\sum_{\text{spin}}^{e} u_e \bar{u}_e = \not{p} + m$ and similarly for the neutrino. Using the commutation properties of γ_a, γ_5, we obtain

$$\frac{1}{2} \operatorname{Tr}[\not{p} \mathcal{M} \not{k} \mathcal{M}^* (1 + i\gamma_5)] \tag{A9}$$

$$= 2[2 \operatorname{Re}(M \cdot p)(M \cdot k)^* - (p \cdot k)(M \cdot M^*) + i \epsilon_{\alpha\beta\gamma\delta} M_\alpha^* M_\beta p_\gamma k_\delta]$$

where $i \epsilon_{\alpha\beta\gamma\delta} M_\alpha^* M_\beta p_\gamma k_\delta$ can be written in the more accessible form

$$M_o^* (\vec{M} \cdot \vec{p} \times \vec{k}) - M_o (\vec{p} \cdot \vec{k} \times \vec{M}^*) + W(\vec{k} \cdot \vec{M}^* \times \vec{M}) - k(\vec{M}^* \cdot \vec{M} \times \vec{p})$$

and vanishes when any two of M, M^*, p or k are equal. The allowed matrix element, $G_A\langle\vec{\sigma}\rangle$ accounts for most of the decay and we will illustrate the computation with this matrix element. The quantity $\langle\vec{\sigma}\rangle$ is an abbreviation for $\langle oo|\sigma_m|1\text{-}m\rangle$, where the states are labeled $|JM_J\rangle$. In evaluating $|M|^2$, we must average over the initial states of the system and sum over the final states. For this purpose it is convenient to use the Wigner-Eckart theorem, which gives

$$\langle 00|\sigma_m|1\text{-}m\rangle = \frac{(-1)^m}{\sqrt{3}}\ \langle 0\|\sigma\|1\rangle \qquad \text{(A10)}$$

or

$$\langle 0\|\sigma\|1\rangle = \sqrt{3}\ \langle 00|\sigma_z|10\rangle = \sqrt{3}\ \langle\sigma_z\rangle$$

The sum over all initial and final states is then $|\langle\|\sigma\|\rangle|^2 = 3|\langle\sigma_z\rangle|^2$, but since the initial state has three possible configurations, we must divide by three. In this way the average and sum over states gives

$$\langle\vec{\sigma}\rangle\cdot\langle\vec{\sigma}\rangle^* \longrightarrow |\langle\sigma_z\rangle|^2$$

and $$(\vec{A}\cdot\langle\vec{\sigma}\rangle)(\vec{B}\cdot\langle\vec{\sigma}\rangle^*) \longrightarrow \frac{1}{3}(\vec{A}\cdot\vec{B})\ |\langle\sigma_z\rangle|^2 . \qquad \text{(A11)}$$

Inserting $M_a = (0,\ G_A\langle\vec{\sigma}\rangle)$ into equation A9 and using equation A11 gives

$$|M|^2 = 2G_A{}^2\ |\langle\sigma_z\rangle|^2\ (Wk - \frac{1}{3}\vec{p}\cdot\vec{k}) . \qquad \text{(A12)}$$

APPENDIX B

Estimation of the Matrix Elements

The strength of the electromagnetic coupling is $\sqrt{4\pi}\, e$ $(e^2 = \frac{1}{137})$ thus from the Golden Rule,

$$\Gamma_\gamma = \frac{2\pi |M|^2 D}{2\omega} \tag{B1}$$

where $D = \frac{\omega^2 d\Omega}{(2\pi)^3}$ is the density of final states if nuclear recoil is neglected. Now $\vec{M} = \sqrt{4\pi}\, e \frac{1}{2}(\vec{a} \times \vec{r}) \times \vec{q}\ \frac{1}{2}\tau_z$ from equation 10 and Table I, and measuring from the z component of $\frac{1}{2}(\vec{a} \times \vec{r})$ gives $\frac{1}{2}(\vec{a} \times \vec{r})_z\, \omega \sin\theta$ where $\omega = |\vec{q}|$. The integral $\int \sin^2\theta\, d\Omega = \frac{8\pi}{3}$, hence

$$\Gamma_\gamma = \frac{4}{3} e^2 \omega^3 \left| < \frac{1}{2} \vec{a} \times \vec{r}\ \frac{1}{2}\ \tau_z > \right|^2 \tag{B2}$$

for the ground state transition from the 15.11-Mev $T = 1$ state of C^{12}.

By definition,

$$a = \frac{G_V < \frac{1}{2} \vec{a} \times \vec{r}\, \tau_+ >}{-G_A < \vec{\sigma} \tau_+ >} = \frac{2}{\sqrt{2}} \frac{G_V < \frac{1}{2} \vec{a} \times \vec{r}\ \frac{1}{2}\ \tau_z >}{-G_A < \vec{\sigma} \tau_+ >}$$

giving

$$\Gamma_\gamma = \frac{4}{3} e^2 \omega^3 a^2 \left| < \sigma_z > \right|^2 \frac{G_A^2}{2G_V^2}$$

where the $\frac{1}{\sqrt{2}}$ derives from the τ_+ defined here differing from the

irreducible + component of τ_z by this factor.

Since the ft value of B^{12} is inversely proportional to $G_A^2 |< \sigma_z >|^2$ and the ft value of O^{14} is in the same relation to $G_V^2 |<1>|$,

$$\frac{ft\,(B^{12})}{ft(O^{14})} = \frac{G_V^2 \,|<1>|^2}{G_A^2 \,|<\sigma_z>|^2} \tag{B3}$$

and therefore

$$|a| = \left[\frac{3\Gamma_{\gamma} \; ft\,(B^{12})}{4e^2 \; 3 \; ft(O^{14})}\right]^{1/2} \tag{B4}$$

assuming $|<1>| = \sqrt{2}$ for O^{14}.

The matrix element $\gamma_5 \vec{r}$ is reduced in Appendix A to the form $\frac{1}{2M}\left[(\vec{\sigma}\cdot\vec{p})\vec{r} + \vec{r}(\vec{\sigma}\cdot\vec{p}) \right]$. Using the identity

$$\vec{a}(\vec{b}\cdot\vec{c}) = -\frac{1}{3}\vec{b}(\vec{a}\cdot\vec{c}) + \frac{1}{2}\vec{b}\times(\vec{a}\times\vec{c}) + \frac{1}{3}\vec{b}(\vec{a}\cdot\vec{c}) - \frac{1}{2}\vec{a}\,(\vec{b}\cdot\vec{c}) - \frac{1}{2}(\vec{a}\cdot\vec{b})\vec{c} \tag{B5}$$

we have

$$2M\gamma_5\vec{r} \rightarrow -\frac{1}{3}\vec{\sigma}\,(\vec{p}\cdot\vec{r} + \vec{r}\cdot\vec{p}) + \vec{\sigma}\times(\vec{r}\times\vec{p}) + \sigma_j Q_{ij} \tag{B6}$$

where $Q_{ij} = (\vec{p}\cdot\vec{r})_{ij} + (\vec{r}\cdot\vec{p})_{ij}$ as defined in Table I, but $<\|\sigma\,(\vec{p}\cdot\vec{r} + \vec{r}\cdot\vec{p})\|>$ differs from $<\|\sigma\, r^2\|>$ only by the ratio

$$\frac{<\ell\|\,\vec{p}\cdot\vec{r} + \vec{r}\cdot\vec{p}\,\|\ell>}{<\ell\|\,\vec{r}\cdot\vec{r}\,\|\ell>} \tag{B7}$$

when ℓ is the orbital angular momentum of the initial and final state. This relation is no longer rigorous if other angular momenta are admixed into the p-shell. Similarly, $<\sigma_j Q_{ji}>$ is given from

$<\| \sigma_j R_{ji} \| >$ when multiplied by

$$\frac{<\ell\| Q\| \ell>}{<\ell\| R\| \ell>} \tag{B8}$$

where R_{ij} is defined in Table I. Taking $\ell = 1$ for the p-shell then gives for both equations B7 and B8

$$-i <2 + \frac{\partial}{\partial r} r + r \frac{\partial}{\partial r} >_{radial} / <r^2>_{radial}$$

Any choice of ℓ will give this result; however the radial wave functions vary with ℓ, and $<\ell'\| Q\| \ell>$ has in general non-zero values between off-diagonal elements when admixing is present. The radial matrix element $<2 + \frac{\partial}{\partial r} r + r \frac{\partial}{\partial r} >$ depends only upon the form of the radial wave functions. In fact this matrix element is identically zero if the initial and final wave functions are identical, an assumption usually made in shell-model calculations. If the wave functions are described by a single scale parameter (e.g. the quantity β defined at the end of this appendix), this matrix element is zero even when the initial and final wave functions are assigned different scales. Thus

$$\gamma_5 \vec{r} \longrightarrow \frac{1}{2M} (\vec{\sigma} \times \vec{\ell}) \tag{B9}$$

and the expression $\vec{\sigma} \times \vec{\ell}$ can be reduced, using the identities $\vec{\sigma} \times \vec{\sigma} = 2i\vec{\sigma}$ and $\vec{A} \times (\vec{B} \times \vec{C}) = \vec{B}(\vec{A}\cdot\vec{C}) - (\vec{A}\cdot\vec{B})\vec{C}$, to $\frac{i}{2}[\vec{\sigma}(\vec{\sigma}\cdot\vec{\ell}) - (\vec{\sigma}\cdot\vec{\ell})\vec{\sigma}]$. Since $<\vec{\sigma}\cdot\vec{\ell}> = j(j+1) - \ell(\ell+1) - s(s+1)$ for single particle states we can estimate $\gamma_5 \vec{r}$ by assuming the extreme j-j coupling mode which gives for the transition $(\frac{1}{2}\ 1\ \frac{3}{2}) \longrightarrow (\frac{1}{2}\ 1\ \frac{1}{2})$ in $(s\ell j)$ notation

$\frac{i}{2}<\vec{\sigma}(\vec{\sigma}\cdot\vec{\ell})-(\vec{\sigma}\cdot\vec{\ell})\vec{\sigma}> \sim \frac{3}{2}\ i<\vec{\sigma}>$, yielding $b \sim \frac{3}{4M}\ i$.

Now to consider $(\sigma \cdot r_2)_1$. In the extreme j-j coupling model (40) the C^{12} nucleus constitutes a filled $(S^2_{1/2}\ P^4_{3/2})(S^2_{1/2}\ P^4_{3/4})$ configuration where the proton shell has been written first. For B^{12}, having one more neutron and one less proton, the configuration is $(P^3_{3/2})(P_{3/2}\ P_{1/2})$ with the filled $S_{1/2}$ shells implied but not written. The transition is then from a $j = 1/2$ neutron to a $j = 3/2$ proton, each coupled to the $(P^3_{3/2})(P^4_{3/2})$ "hole" wave function having $T = 1/2$, $J = 3/2$. In calculating $<\sigma_z>$ the coupling to the hole gives a common factor $(\sqrt{2})$ times $(j = 3/2 \mid \sigma_z \mid j = 1/2)$. The evaluation of the j-j matrix elements is straightforward giving

$$(3/2 \mid \sigma_z \mid 1/2) = -\frac{2\sqrt{2}}{3} \qquad \text{(B10)}$$

$$(3/2 \mid 3(\vec{\sigma}\cdot\vec{r})z - \sigma_z\, r^2 \mid 1/2) = -\frac{\sqrt{2}}{3}\ <r^2>_{\text{radial}}$$

Therefore, $c = \frac{d}{2}$ in this model. The transition matrix element predicted from this model is about twice that observed experimentally, although the ratio c/d may not be as far off. With this rough estimate as a guide the matrix element is computed from the intermediate coupling model. This model is discussed extensively by Elliot and Lane (41). The matrix element of

$$(\sigma \cdot r_2)_1 = -\sqrt{\frac{1}{10}}\ (3(\vec{\sigma}\cdot\vec{r})\vec{r} - \vec{\sigma}\, r^2) \qquad \text{(B11)}$$

is computed for the Rosenfeld, Kurath and Serber force mixtures with the parameters $L/K = 5.3$, 6.8, and 8.3 and $a/K = 0$, 3, 4.25, 5.5

6.75, and 8 for which the energy matrix has been diagonalized by Weidenmüller (42). The fractional parentage coefficients of Jahn and van Wieringen (43) were used to compute the transition matrix element between the five possible eigenstates comprising the C^{12} ground state and the eight for the B^{12} or N^{12} ground states. The result for the Rosenfeld force is displayed in Figure 21. The Kurath and Serber forces give similar results. Only one value of a/K gives the proper ft value for a given choice of L/K and force mixture, and when this constraint is applied the value of c/d is found to be nearly independent (with 1% for the range studied) of L/K with c/d = 0.59, 0.56, and 0.46 for the Rosenfeld, Kurath, and Serber forces. The first two estimates are probably more reliable since the Serber force mixture does not reproduce the level structure of even simple nuclei. From these estimates we conclude that large spectral deviations are not likely to derive from anomalously large values of the matrix elements $\gamma_5 \vec{r}$ or $(\sigma \cdot r_2)_1$.

To calculate the radial wave functions we assume that the actual distribution can be fit reasonably well into harmonic oscillator wave functions with the same scale factor, β, for both the s- and p-shells. Then the charge density (normalized to unity) is

$$\rho(r) = \frac{1}{3} N_s^2 e^{-\beta r^2} + \frac{2}{3} N_p^2 r^2 e^{-\beta r^2} \qquad \text{(B12)}$$

where $N_s^2 = \left(\frac{\beta}{\pi}\right)^{3/2}$, $N_p^2 = \frac{2}{3}\left(\frac{\beta^5}{\pi^3}\right)^{1/2}$. The mean-square charge

radius is then $\langle r^2 \rangle_{charge} = \frac{13}{6\beta} = 5.61\ f^2$ (Experiment). The value of the mean-square radius for just the p-shell gives $\langle r^2 \rangle_{p\text{-shell}} = \frac{5}{2\beta} = \frac{15}{13} \langle r^2 \rangle_{charge}$. In this fashion the p-shell gives $\langle \frac{1}{r} \rangle = 0.466\ f^{-1}$, $\langle r \rangle = 2.42\ f$, and $\langle r^2 \rangle = 6.48\ f$ while the net charge distribution gives $\langle \frac{1}{r} \rangle = 0.544\ f^{-1}$, $\langle r \rangle = 2.22\ f$, and $\langle r^2 \rangle = 5.61\ f^2$.

APPENDIX C

Coulomb Corrections

Having a situation where the Coulomb interaction is only a perturbation, we can use the approximate Sommerfeld-Maue wave functions (44) rather than the exact Coulomb wave functions. These wave functions are written in the form

$$\psi_{sm}(\vec{r}) = e^{i\vec{p}\cdot\vec{r}}\, C(\vec{r})\, u_e(\vec{p}) \tag{C1}$$

where $C(\vec{r}) = N\left(1 - \frac{i}{2W}\,\vec{\alpha}\cdot\vec{\nabla}\right)F$

$$F = F\left(i\eta\,\frac{W}{p}\,;\,1;\,ipr - i\vec{p}\cdot\vec{r}\right), \quad \eta = Ze^2$$

and $N = e^{1/2\,\pi Ze^2}\Gamma(1 + iZe^2)$. $C(\vec{r})$ is then a 4×4 matrix that transforms the free Dirac spinor for an electron of momentum $\vec{p}$, $u_e(\vec{p})$, into the approximate Sommerfeld-Maue spinor. The confluent hypergeometric function, F, may be expanded about $\eta = 0$ and yields to order $\eta(pr)^2$.

$$\psi_{sm} = N[C_0 + C_1 + C_2]\; u_e(\vec{p}) \tag{C2}$$

where

$$\begin{aligned}
C_0 &= \left[1 - \eta WR - \frac{1}{2}\,i\eta\,\vec{\alpha}\cdot\vec{p}\left(1 + \frac{1}{2}\,ipR\right)\right] \\
C_1 &= \left[\eta\,\frac{W}{p}\,\vec{p}\cdot\vec{R} + \frac{1}{2}\,\frac{\eta}{R}(\vec{\alpha}\cdot\vec{R})\left(1 + \frac{1}{2}\,ipR\right) - \frac{1}{4}\,\frac{\eta}{p}\,(\vec{\alpha}\cdot\vec{p})(\vec{p}\cdot\vec{R})\right. \\
&\qquad\qquad \left. + i\vec{q}\cdot\vec{r}\; C_o\right] \\
C_2 &= \left[\frac{1}{4}\,\frac{\eta}{R}(\vec{\alpha}\cdot\vec{R})(\vec{p}\cdot\vec{R}) - \frac{1}{2}\,(\vec{q}\cdot\vec{r})^2 + i\vec{q}\cdot\vec{r}\,\left(\frac{1}{2}\,i\,\frac{\eta}{R}\;\vec{\alpha}\cdot\vec{R}\right)\right]
\end{aligned} \tag{C3}$$

which includes the contribution $e^{i\vec{k}\cdot\vec{r}}$ from the neutrino wave function. In the limit $\eta \rightarrow 0$ this is just the retardation expansion which generates Table I in the text. We have distinguished the position vector of the decaying nucleon, $\vec{r}$, from the distance between the decaying nucleon and the other charges, $\vec{R} = (\vec{r} - \vec{r}_i)$, where $\vec{r}_i$ is the positron vector of the i^{th} proton and the sum over i is to be performed after integration over $\vec{r}$.

The Coulomb corrections to the allowed decay are mainly derived from C_0, while additional corrections of the same order come from terms in C_2 representing scalar spatial components. Since

$$(\vec{a}\cdot\vec{r})(\vec{b}\cdot\vec{r}) = \frac{1}{3}(\vec{a}\cdot\vec{b})\,r^2 + \left(\frac{1}{2}a_i b_j + \frac{1}{2}a_j b_i - \frac{1}{3}(\vec{a}\cdot\vec{b})\delta_{ij}\right)\left(r_i r_j - \frac{1}{3}r^2\delta_{ij}\right)$$

each term in C_2 can be rearranged into a spatial scalar and a spatial tensor. For the allowed transition σ both the scalar and tensor terms contribute since $\vec{\sigma}$ can couple to r_2 to form another axial vector as we have seen. In addition, the couplings $(\sigma\cdot r_2)_{2,3}$ will contribute for less restrictive transitions such as $2^+ \rightarrow 2^+$. For illustration the correction derived from C_0 and the spatial scalar terms in C_2 will be computed.

Since $u_e \rightarrow Cu_e$ then $\bar{u}_e \rightarrow (Cu_e)^+\beta = \bar{u}\bar{C}$ where $\bar{C} = \beta C^+ \beta$ and the sum over electron spins of $\Sigma u_e \bar{u}_e$ becomes

$$\Sigma C u_e \bar{u}_e \bar{C} = C(\not{p} + m)\bar{C}. \qquad (C4)$$

Starting with the first expression in A8 and the replacement C4 gives

$\frac{1}{4}$ Tr $[\mathcal{M}^{*} C \not{p} \bar{C} \mathcal{M} \not{k} (1 + i\gamma_5)]$ where $\mathcal{M} = -\beta\vec{\alpha} \cdot \langle\vec{\sigma}\rangle$ for the allowed transition. The projections of $\langle\vec{\sigma}\rangle$ are summed over (A11) and the identities $\sum_i \alpha_i \beta \alpha_i = 3\beta$, $\sum_i \alpha_i \vec{\alpha} \alpha_i = \vec{\alpha}$ give

$\frac{1}{4}$ Tr $[C\beta(W - \vec{\alpha} \cdot \vec{p})\bar{C} \beta (3k - \vec{\alpha} \cdot \vec{k}) (1 + i\gamma_5)]$ which is easily reduced using $C = C_0 +$ scalar part of C_2 and $(\vec{\alpha} \cdot \vec{p})(\vec{\alpha} \cdot \vec{p}) = p^2$ to

$$\left(1 - 2\eta R + \frac{1}{3} \eta \frac{p^2}{W} R\right) 3Wk \qquad (C5)$$

after averaging over the electron-neutrino angular correlation and performing the trace. This is the so-called finite de Broglie wavelength effect (32) and gives a correction to the ratio of the shape factors of $\delta A_{\text{de Broglie}} \sim -\frac{10}{3} \eta R \sim -0.18$ percent per Mev using the decay radius of Appendix B. Gell-Mann and Berman (16) give a more consistent analysis which includes the coupling of $\vec{\sigma}$ with r_2 and distinguishes $\vec{r}$ from $\vec{R}$ with the result $\delta A_{\text{Coulomb}} = -0.21$ percent per Mev.

APPENDIX D

Other Effects

Here we would like to touch on some questions that logically arise from the foregoing discussion.

Conserved Axial Vector Current

It has been shown (45) that a conserved axial vector current is not possible. The most general axial vector current is

$$J_a^A = (\bar{\psi}_n \left[i\gamma_a \gamma_5 \; A(q^2) + iq_a \gamma_5 \; B(q^2) + \sigma_{a\beta} q_\beta \gamma_5 \; C(q^2) \right] \psi_p) \quad (D1)$$

In momentum space the conservation condition is $q_a J_a^A = 0$, thus

$$(M_p + M_n) A(q^2) (\bar{\psi}_n | \, i\gamma_5 \, | \psi_p) + q^2 B(q^2) (\bar{\psi}_n | \, i\gamma_5 \, | \psi_p) = 0 \quad (D2)$$

which then requires $(M_p + M_n) A(q^2) = - q^2 B(q^2)$ if J_a^A is to be conserved. In the limit $q^2 \longrightarrow 0$ $A(0) \longrightarrow G_A$, and

$$B(q^2) \longrightarrow - \frac{(M_p + M_n) G_A}{q^2} \quad (D3)$$

which would mean that the second term dominates at small q (i.e. nuclear beta decay), contrary to experiment (13).

Induced Pseudoscalar Interaction

Since the nucleon is strongly coupled to the pion and since the pion interacts via the beta decay interaction we have an interaction (in second order perturbation theory)

$$\sqrt{4\pi}\ g\,(\bar{\psi}_p|\gamma_5|\psi_n)\sqrt{2}\,(m_\pi^2 - q^2)^{-1}\,F(q^2)\,(\bar{\psi}_e|\not{q}\,(1+i\gamma_5)|\psi_\nu) \qquad (D4)$$

where $F(q^2)\,(\bar{\psi}_e|\not{q}\,(1+i\gamma_5)|\psi_\nu)$ is the transition amplitude for the decay $\pi^- \longrightarrow e + \bar{\nu}$. The universality hypothesis requires this decay to be coupled with the same strength as $\pi^- \longrightarrow \mu + \bar{\nu}$, and the latter decay rate has been accurately measured.

$$\Gamma_{\pi\mu\nu} = F^2(m_\pi^2)\, m_\mu^2\, (m_\pi^2 - m_\mu^2)^2 = 2.55 \times 10^{-8}\ \text{sec.} \qquad (D5)$$

For electron decay this gives

$$8\,G_A\ \frac{m_e}{m_\mu}\left(\frac{m_\pi^2 - m_\mu^2}{m_\pi^2 - m_e^2}\right)\quad (\bar{\psi}_p|\gamma_5|\psi_n)(\psi_e|\,(1+i\gamma_5)|\psi_\nu) \qquad (D6)$$

assuming $F(m_\pi^2) \sim F(0)$ (17), where $8\,G_A$ is the effective coupling for muon capture, $\frac{m_e}{m_\mu}$ is from the smaller momentum transfer in beta decay and $(m_\pi^2 - m_\mu^2)(m_\pi^2 - m_e^2)^{-1}$ is from the pion propagator. Such a term has only $\sim 1/120$ the coupling of the allowed decay, and furthermore contributes only a second-forbidden term with momentum dependence similar to b.

Uxl

If the beta-decay interaction is mediated by a boson (Uxl), then the delta function in equation 14 is modified. It is simplest to write the correct expression in momentum space where the interaction is $J_\alpha\,\delta_{\alpha\beta}L_\beta$, and $\delta_{\alpha\beta}$ is modified to

$$\frac{\delta_{\alpha\beta} M_x^2 - q_\alpha q_\beta}{M_x^2 - q^2} \tag{D7}$$

In the limit $M_x \to \infty$ this reduces to $\delta_{\alpha\beta}$ which we have used. Although M_x is unknown, the failure to observe the decay $K \to \gamma + X$ imposes the limit $M_x > M_k$. For beta decay we then expand $M_x^2(M_x^2 - q^2)^{-1} = (1 + \frac{q^2}{M_x^2} + \cdots)$. The energy dependence at the end of the spectrum is then estimated to be less than -0.01%/Mev, hence negligible for our interests. The $q_\alpha q_\beta$ piece gives an additional term

$$M_x^{-2}(\bar{\psi}_e | \not{q}(1 + i\gamma_5) | \psi_\nu)(\bar{\psi}_p | \not{q}(1 + i\gamma_5) | \psi_n) \tag{D8}$$

$$= \frac{m_e M_n}{M_x^2}(\bar{\psi}_e | (1 + i\gamma_5) | \psi_\nu)(\bar{\psi}_p | i\gamma_5 | \psi_n)$$

with neglect of the neutron-proton mass differences. The factor $(m_e M_n / M_x^2) \leq .002$ and since only the $\vec{r}$ term in the retardation expansion of $(\bar{\psi}_p | i\gamma_5 | \psi_n)$ contributes, the effects of an Uxl are completely negligible here.

Orbital Contributions

It has also been pointed out (42) that if $\langle (1 + \mu^\nu)\vec{\sigma} + \vec{\ell} \rangle$ is dominated by the orbital term, then a positive experimental result is actually not a test of the conserved vector current theory. Weidenmüller (42) has estimated that $\left| \frac{\langle \| \ell \| \rangle}{\langle \| \sigma \| \rangle} \right| < 0.1$ so, within the limitations of the shell model, the orbital contribution is expected to be small. Experimentally this is supported in that Γ_γ agrees so closely (17%)

with the value computed simply from $< \|(1 + \mu^{\nu})\sigma\| >$. The value of the quantity a given from Γ_{γ} automatically includes the orbital contribution.

Other Terms in the C.V.C.T.

Extending the isotopic spin formulation that gave equation 6 gives (46)

$$J_{\alpha+}^{(\beta)} = \sqrt{2}\, G [(\bar{p}\gamma_{\alpha} n) + \sqrt{2}\, (\pi^{+} \partial_{\alpha} \pi^{o} - \pi^{o} \partial_{\alpha} \pi^{+})$$
$$+\sqrt{2}\, (\bar{\Sigma}^{o} \gamma_{\alpha} T_{+} \Sigma^{-} - \bar{\Sigma}^{+} \gamma_{\alpha} T_{+} \Sigma^{o}) \qquad (D9)$$
$$+ (\bar{\Xi}^{o} \gamma_{\alpha} \Xi^{-}) + (K^{o} \partial_{\alpha} K^{*} - K^{*} \partial_{\alpha} K^{o}) + \ldots]$$

Unfortunately none of the additional terms lead to any more feasible experiments than the $\pi^{-} \longrightarrow \pi^{o} + e + \nu$ decay and the nuclear "weak magnetism." In a sense the nuclear physics experiment tests to some extent all of the above couplings, since the nuclear magnetic moment is not attributable merely to the pion currents. On the other hand, the dependence is probably negligible.

The term $\sigma_{\alpha\beta}\, q_{\beta}\, G(q^{2})$ in equation D1 is usually omitted, as it transforms under charge conjugation differently from $\gamma_{\alpha}\gamma_{5}$ and thus cannot be induced by $\gamma_{\alpha}\gamma_{5}$. The consequences of such a term (46) include a small difference between the ft values (and also the quantity a) for B^{12} and N^{12}. Even if present, such a term would not be expected to vitiate the conclusions of this experiment.

APPENDIX E

Spectrometer Alignment

Three orthogonal sets of Helmholz coils were used to neutralize the earth's magnetic field at the spectrometer, the required current in each set being determined with an air-driven rotating loop magnetometer. This was done for each direction of the magnet current. It should be mentioned that whenever the magnetic field was reversed, the field was first run up to the maximum obtainable before any measurements were made. The purpose of this was to saturate any ferromagnetic material so near to the spectrometer as to possibly distort its field. Thus we were always working with a consistent magnetic history.

The physical arrangement utilized in aligning the spectrometer is illustrated in Figure 25. A small ($\sim$ 3-mm dia.) source was made by placing a drop of Cs^{137} solution on a very thin mica foil (<10 mg/cm^2) which was in turn held by an aluminum wire loop. The 0.6616-Mev conversion electrons were detected in a geiger-counter masked down to a 3-mm diameter. The source-detector axis was brought into coincidence with the symmetry axis of the magnetic field by positioning the detector end of the spectrometer to give the maximum counting rate, reversing the field direction, and repositioning the counter end to again find the maximum. The detector was then set to the average of these two positions and the entire procedure repeated for the source

end of the spectrometer. The source and detector ends of the spectrometer were alternately adjusted until no further improvement could be realized. A displacement of 0.1 mm was detectible. The central bundle from the three-ring baffle was used for this calibration.

The three-ring baffle admitted only three narrow bundles of beta rays near the inner, outer, and mean acceptance angles. The Geiger-counter was moveable along the spectrometer axis and could be positioned to detect any one of the three bundles. The identity of this bundle could be determined by moving the acceptance baffle in until the bundle was eclipsed. To determine the trajectory the counter baffle was positioned to partially eclipse the bundle. This position along with the radius of the counter baffle and the counter position gave two points through which the trajectory passed. With this information the ring-focus baffle was constructed. The results were essentially the same as those shown in Figure 28 of reference 3.

The Cs^{137} spectrum after final alignment (ring-focus baffle in place) is shown in Figures 23 and 24.

APPENDIX F

Backscattering, Annihilation, and Bremsstrahlung Losses

Backscattering

Wapstra (47) gives several empirical relations concerning the backscattering of electrons. Use of these relations is simple and gives

$$I_b/I = f(1 - 2^{-3d/d_{1/2}}) \qquad (F1)$$

where I_b/I is the fraction of the electrons backscattered within the depth d and $d_{1/2} = 0.19$ cm for backscattering 8-Mev electrons from anthracene. The value of f appropriate to backscattering with small energy loss is not known; only the value of f for total backscattering has been determined. Henceforth all backscattering mentioned refers to backscattering with small energy loss. To estimate the total backscattering ($d \longrightarrow \infty$) we put an upper limit on I_b/I by assuming that the form of equation F1 is correct and taking the intensity of electrons giving 1/4 the maximum pulse height to represent backscattering entirely. It should be noted that the electron scattered from depth d loses about $2d \cdot (-\frac{dE}{dx})$ of energy, thus the electrons under consideration must be backscattered within the first 1/8 of the crystal thickness or 0.125 cm. The experimental pulse-height spectrum as shown in Figure 6 appears to have a very flat tail, and it is this extrapolated counting rate per channel which is used to derive the numbers in the text. The experimental pulse-height spectra then give the results quoted in the text.

Annihilation

The annihilation cross section for positrons in flight is given (48) by

$$\sigma_{ann} = \pi r_o^2 \frac{1}{w+1} \left[\frac{w^2 + 4w + 1}{w^2 - 1} \ln \left[w + (w^2-1)^{1/2} \right] - (w+3)(w^2-1)^{-1/2} \right] \tag{F2}$$

where $r_o = e^2/m$, $w = W/m$, and at 8-Mev this becomes $\sigma_{ann} = (0.178)\pi r_o^2$. If the positron is not to be counted, it must be annihilated before penetrating more than about 1/3 of the crystal thickness, otherwise it will be counted as discussed in the text. The probability, P, of such annihilation is then given by $\sigma \ell \rho N_o f/M$ where $\pi r_o^2 = 25 \times 10^{-26}$ cm^2, ℓ is the path length (0.33 cm), ρ is the density (1.25 gm/cm^3), N_o is Avogadro's number (6.025×10^{23} molecules/mole), f is the number of electrons per anthracene molecule (94), and M is the mass of one mole (178.22 gm/mole). The cross-section behaves essentially as E^{-1}, and altogether we have a correction $\delta A_{ann} \sim \frac{1}{\sigma} \frac{d\sigma}{dE} P_{ann} \sim -\frac{P}{E} = -0.07$ percent per Mev. Since the lower energy positrons are preferentially annihilated, the N^{12} shape factor will tend to slope upwards and reduce the B^{12}-N^{12} difference, hence the minus sign. The mass attenuation coefficient, μ_o/ρ, for anthracene is about .035 cm^2/gm (49) for gamma rays of about 5 Mev, where $e^{-\mu_o x}$ describes the attenuation after passing through a thickness x of material of density ρ. This gives about a 10 percent probability of

observing at least one of the two annihilation photons, and reduces our correction slightly to

$$\delta A_{\text{annihilation}} = -0.06 \text{ percent per Mev.}$$

Bremsstrahlung

The differential radiative cross-section is given by (48)

$$d\sigma_{rad} = \sigma_o B Z^2 \frac{W}{E} \frac{d\epsilon}{\epsilon} \qquad \text{(F3)}$$

where $\sigma_o = \frac{1}{137} \left(\frac{e^2}{m}\right)^2 = 0.580 \times 10^{-27} \text{ cm}^2$, $W = E + m$ is the total energy, ϵ is the energy of the radiated photon, and B is a complicated function of ϵ/E and E given in reference 48. If the discriminator setting rejects particles with energy less than $E_d \sim 1$ Mev, then ϵ must be larger than $E_o - E_d$ (where E_o is the incident kinetic energy) for a particle to be lost due to emitting most of its energy via bremsstrahlung. Since $E_d \ll E_o$ we can write

$$\sigma_{rad} \sim \frac{\sigma_o \bar{B} Z^2 E_d}{E_o} \qquad \text{(F4)}$$

where the factor $\frac{W}{E}$ has been set to unity. The quantity $\bar{B}$ may be estimated from reference 48 to be roughly 4 under these conditions giving $\sigma_{rad} \sim \frac{1}{2} Z^2 \sigma_o$. The same parameters as given above enter except σf becomes $184 \sigma_o$, with the result that about .015 percent of the intensity should be lost.

APPENDIX G

Penetration Correction

Figure 25 is an idealized representation of the baffle geometry showing the quantities of interest here. The baffle is assumed to be uniformly illuminated by beta particles, each of which would strike the center of the anthracene detector crystal were it not for the baffle. If a beta particle penetrates the baffle, then scattering of the particle from its initial direction reduces the probability of striking the crystal. Rohrlich and Carlson (50) give the expression

$$\langle \cos\theta \rangle_{ave} = \frac{G(w_o)}{G(w)} \qquad (G1)$$

for the average $\cos\theta$ of beta particles initially with total energy W_o after being slowed to energy W. Here $G(w) = \left(\frac{w+1}{w-1}\right)^{aZ} \exp(bZ/\beta)$ where $w = W/m$, $\beta = p/W$, and a and b are constants given in Table I of reference 50. For relativistic beta particles

$$G(w) \longrightarrow \left(1 + \frac{2aZ}{w} + \ldots\right) e^{bZ} \qquad (G2)$$

and altogether we have for the average solid angle, Ω,

$$\langle \Omega \rangle_{ave} \sim 4\pi Za\left(\frac{w_o - w}{w_o w}\right) , \qquad (G3)$$

It is convenient to define a characteristic penetration length x_o for which $\langle \Omega \rangle_{ave}$ equals the solid angle to the detector, Ω_o.

Since the $\frac{dE}{dx}$ loss is constant and $w \sim w_o$ if Ω_o is small, we have

$$x_o = m\left(-\frac{dE}{dx}\right)^{-1} \frac{w_o^2 \Omega_o}{4\pi a Z} \tag{G4}$$

The approximation was made that all electrons are counted which must penetrate baffle thickness up to $\frac{1}{2} x_o$, and $\frac{1}{2} \frac{\Omega_o}{<\Omega>_{ave}}$ is the probability of counting the electron for deeper penetration. The effective penetration length, x_e, is the distance for which it is equivalent to say that all beta particles penetrating less than x_e are counted and none are counted for deeper penetration. The two lengths are related by

$$\begin{aligned} x_e &= \frac{1}{2} x_o + \frac{1}{2} \Omega_o m \left(-\frac{dE}{dx}\right)^{-1} \int_1^{w_o - \epsilon} <\Omega>_{ave}^{-1} \, dw \\ &\sim \frac{1}{2} x_o \left[1 + \frac{1}{w_o} \int_1^{w_o - \epsilon} (w_o - w)^{-1} \, w dw \right] \\ &\sim \frac{1}{2} x_o \, \ell n \left(\frac{8\pi a Z}{w_o \Omega_o}\right) \quad \text{where} \quad \epsilon = \frac{w_o^2 \Omega_o}{8\pi a Z} << w_o . \end{aligned} \tag{G5}$$

From Figure 25 it may be seen that the acceptance area of the baffle is effectively increased by a factor

$$\frac{1}{s}(s + x_e \cot \phi) . \tag{G6}$$

The observed shape factors have then been modified by a factor $(1 + \alpha E^2)$ where α is given from equation G5 and equation G6 to be

$$a = \frac{1}{2} \ell n \left(\frac{8\pi a Z}{w_o \Omega_o}\right) \Omega_o \cot\phi \left(-4\pi a Z m s \frac{dE}{dx}\right)^{-1} \qquad (G7)$$

The experimental geometry had for these parameters, $\Omega_o = 2\pi(.00745)$, $s = 0.278$, and $\tan\phi \sim 15$. The quantity a is given in reference 50 to be 0.305 for electrons and 0.297 for positrons, and $\left(-\frac{dE}{dx}\right)$ is about 5.4 Mev/cm. This yields a value of 2.2×10^{-4} $(Mev)^{-2}$ for a. The value 2.4×10^{-4} $(Mev)^{-2}$, quoted in the text, derives from the more generous assumption that all particles penetrating thickness x_o (instead of $\frac{1}{2}$ x_o) are counted. The acceptance baffle should have been of negligible import, since for it Ω_o is very small and s very large, as may be seen in Figure 2.

In addition to the slight difference in the parameter a for positrons and electrons, $\left(-\frac{dE}{dx}\right)$ is expected to be 2.5% less for positrons than for electrons (Fig. 3, reference 50). Together these conspire to give 5% less scattering for positrons and consequently a nominal average correction of

$$\delta A(\text{penetration}) = -0.02 \text{ percent per Mev.}$$

FIGURES

Fig. 1: Energy level diagram of the triad B^{12}, C^{12}, and N^{12}. Only the transitions and levels of importance for this paper are indicated. The notation is standard.

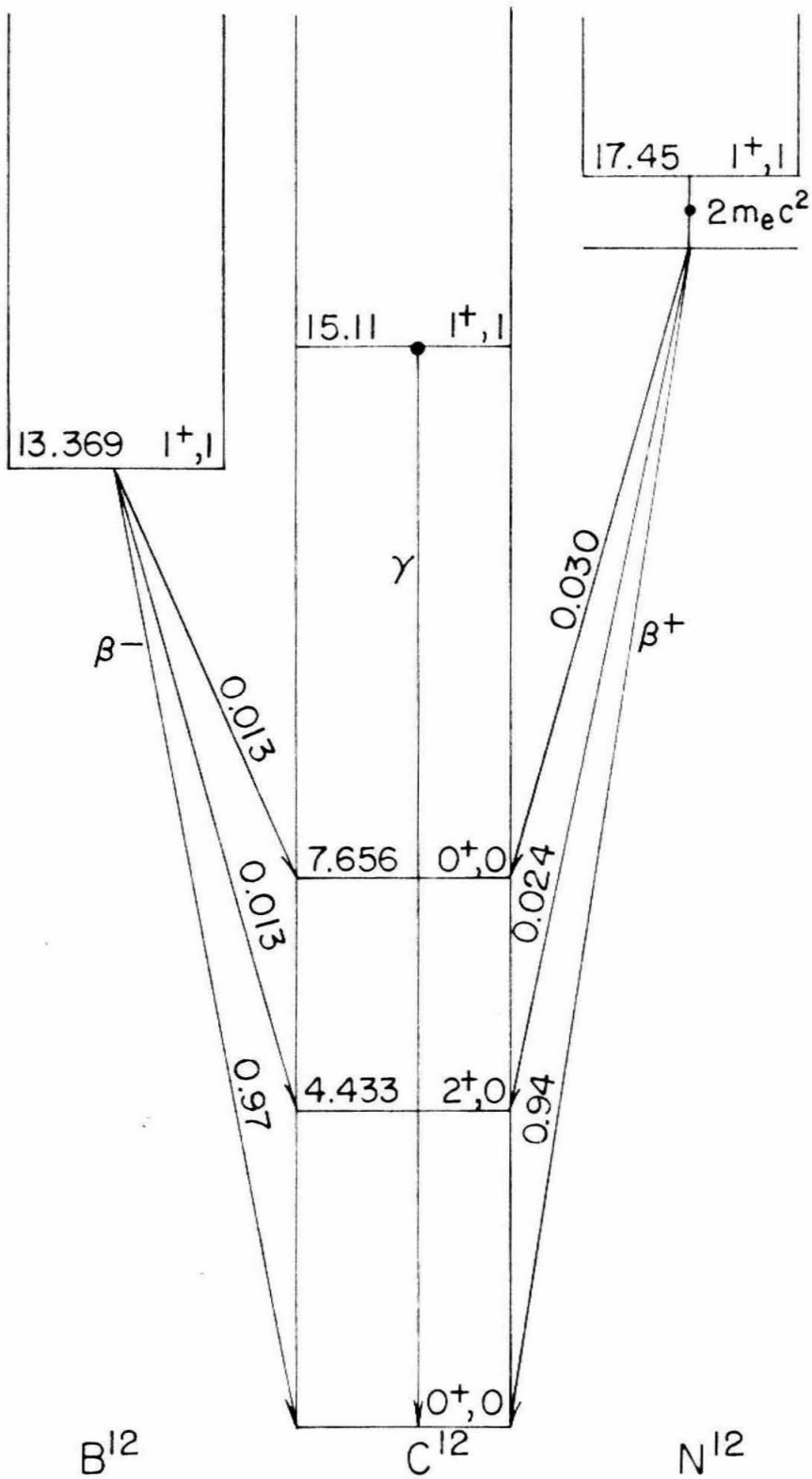
17.45 1+,1
2mec2
15.11 1+,1
13.369 1+,1
γ
0.030
β+
β−
0.013
0.013
7.656 0+,0
0.024
0.97
4.433 2+,0
0.94
0+,0
B12
C12
N12

FIG. 1

Fig. 2: The spectrometer in cross-sectional view with the axis of symmetry along the beam direction. The magnet coils are not shown full diameter. Dotted lines indicate the electron trajectories for the extreme and mean acceptance angles. Unless otherwise indicated, the material is brass.

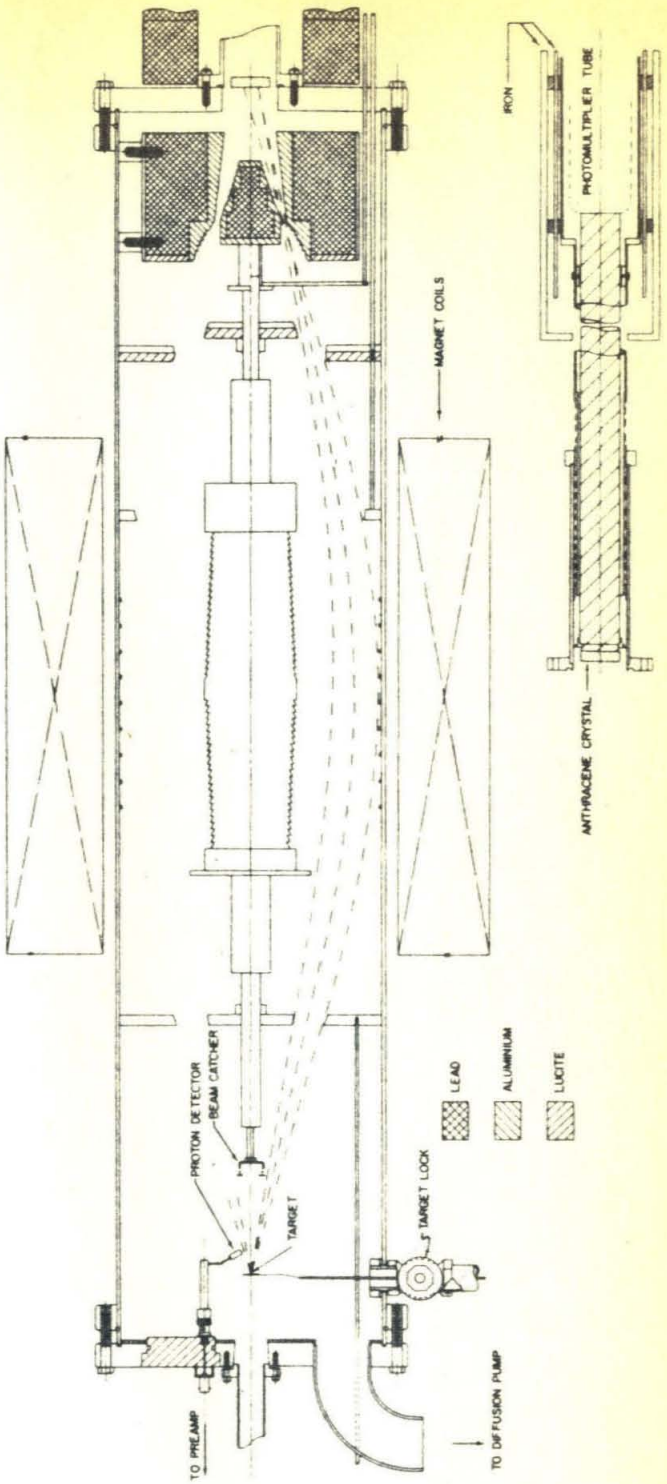
IRON
PHOTOMULTIPLIER TUBE
MAGNET COILS
ANTHRACENE CRYSTAL
PROTON DETECTOR
BEAM CATCHER
TARGET
TARGET LOCK
LEAD
ALUMINUM
LUCITE
TO PREAMP
TO DIF FUSION PUMP

FIG. 2

Fig. 3: Calibration data. The quantity A is the magnet current measured in millivolts of potential drop across a 5 milliohm shunt divided by the $H\rho$ (in kilogauss-cm) of the conversion electrons. The conversion lines are those of Cs^{137}, Bi^{207}, and thorium deposit (F, J, L, M, and X lines). The error bars represent the combined uncertainty in the quoted $H\rho$ value and in experimentally finding the center of the line.

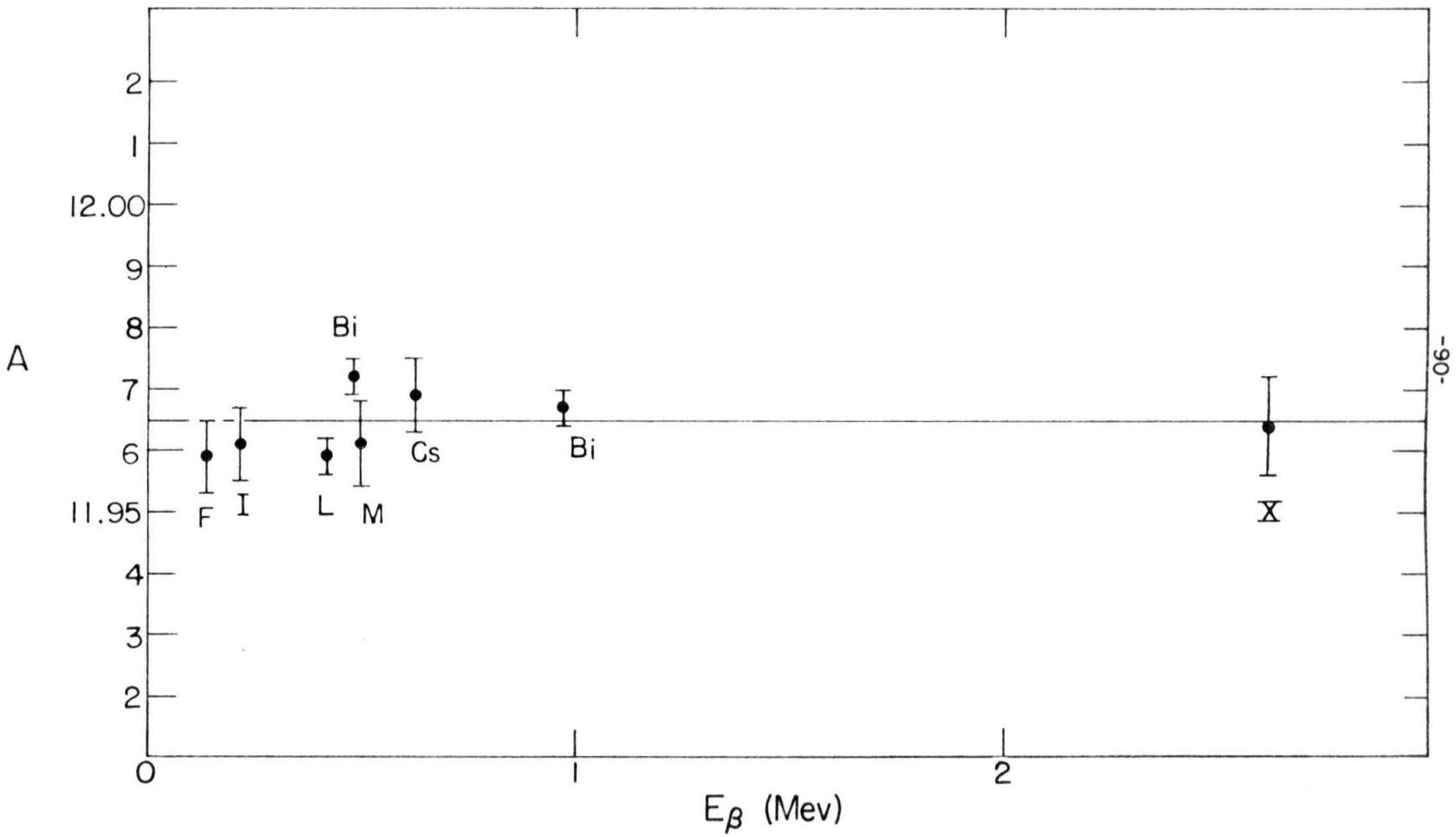

FIG.3

Fig. 4: Pulse-height distributions in the thin anthracene crystal for low-energy beta particles from B^{12}.

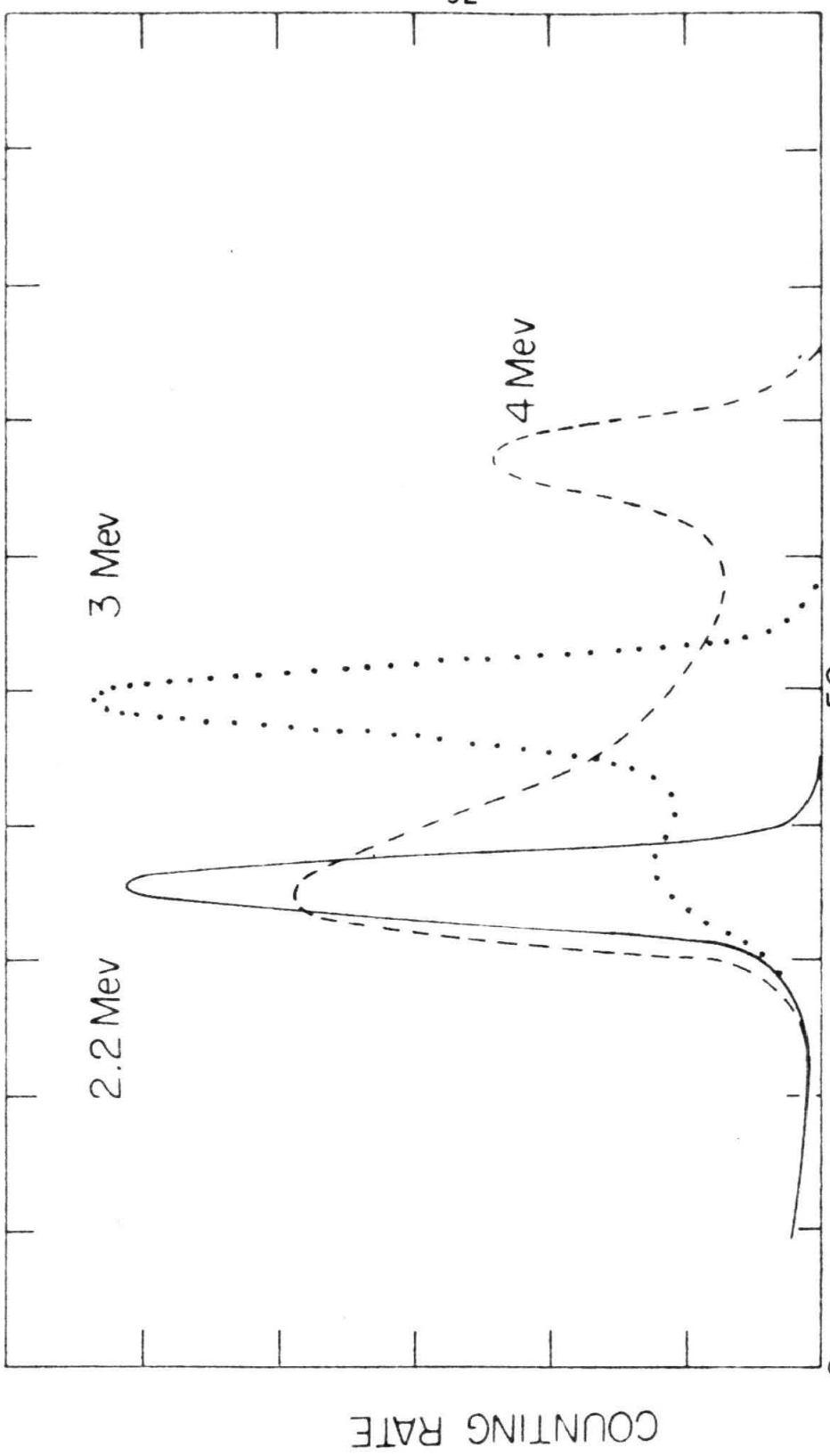

FIG. 4

Fig. 5: Pulse-height distributions in the thin anthracene crystal for high-energy beta particles from B^{12}.

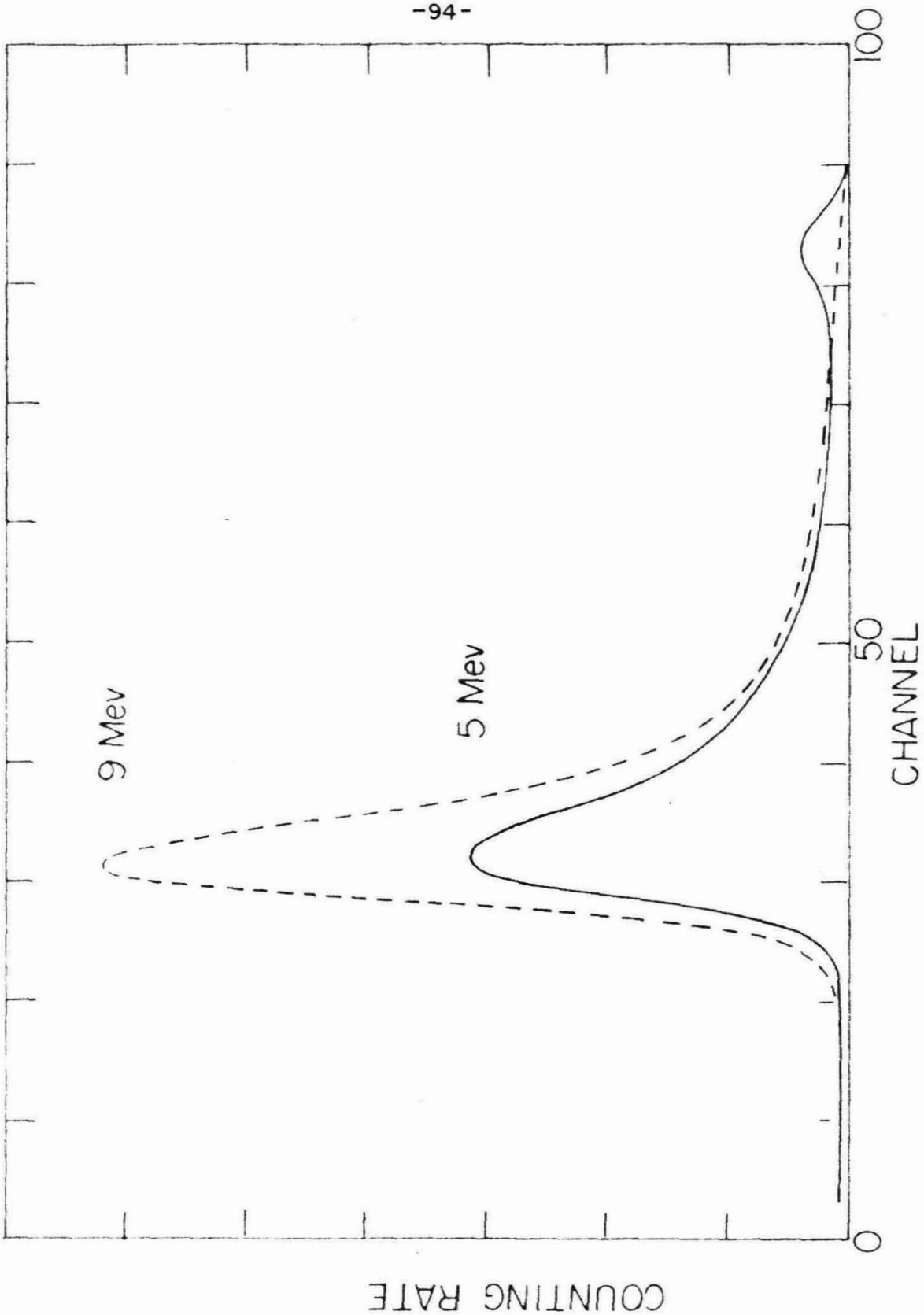

FIG. 5

Fig. 6: Pulse-height distributions for 8.0-Mev electrons from B^{12} and background. The insert shows the small pulse tail amplified by a factor of five.

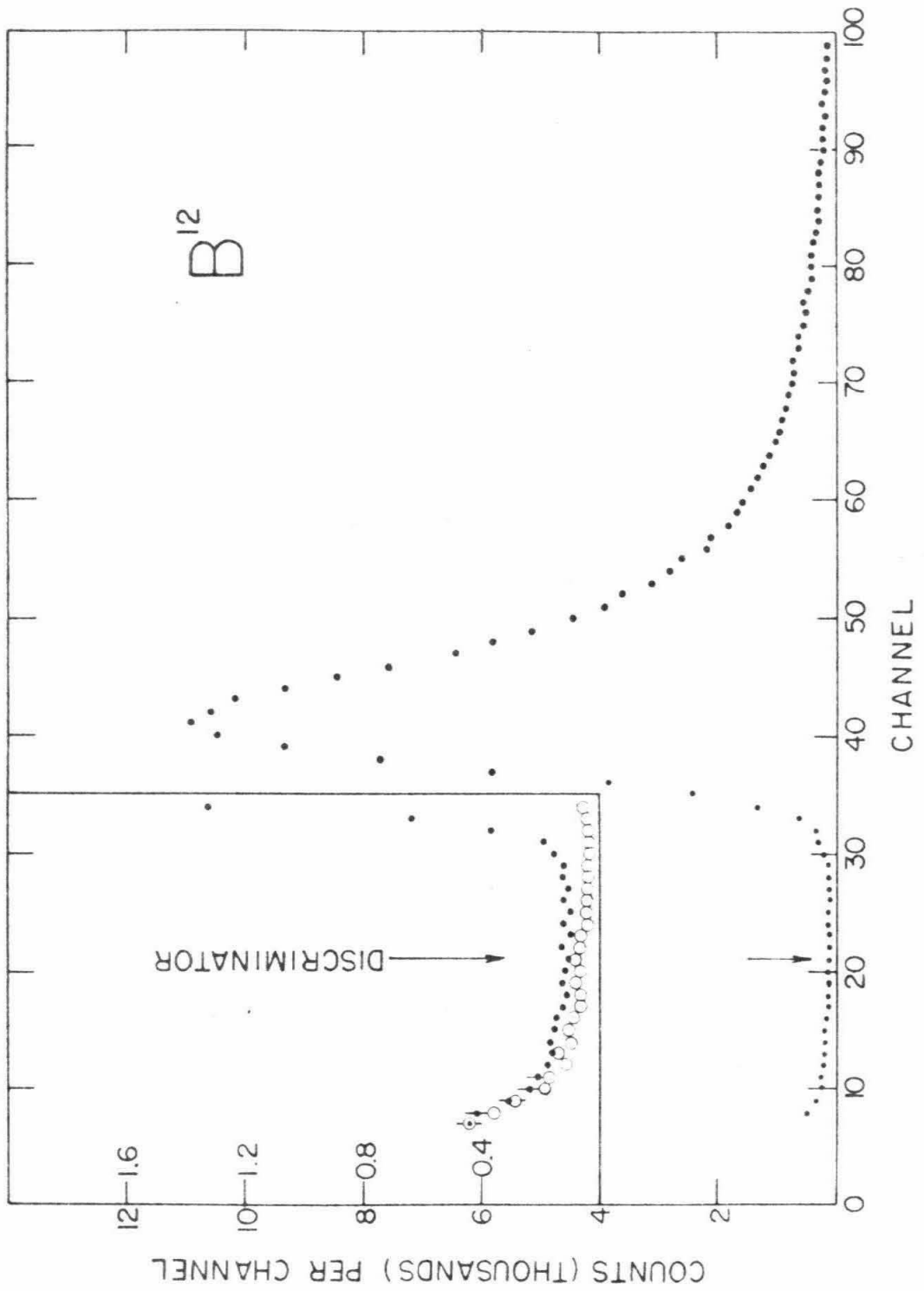
B12
DISCRIMINATOR
COUNTS (THOUSANDS) PER CHANNEL
CHANNEL
0
10
20
30
40
50
60
70
80
90
100
2
4
6
8
10
12
0.4
0.8
1.2
1.6

FIG. 6

Fig. 7: Pulse-height distributions for 8.0-Mev positrons from N^{12} and background. The insert shows the small pulse tail amplified by a factor of five. The vertical bars indicate $\sqrt{N}$ for several channels where N is the number of counts in that channel.

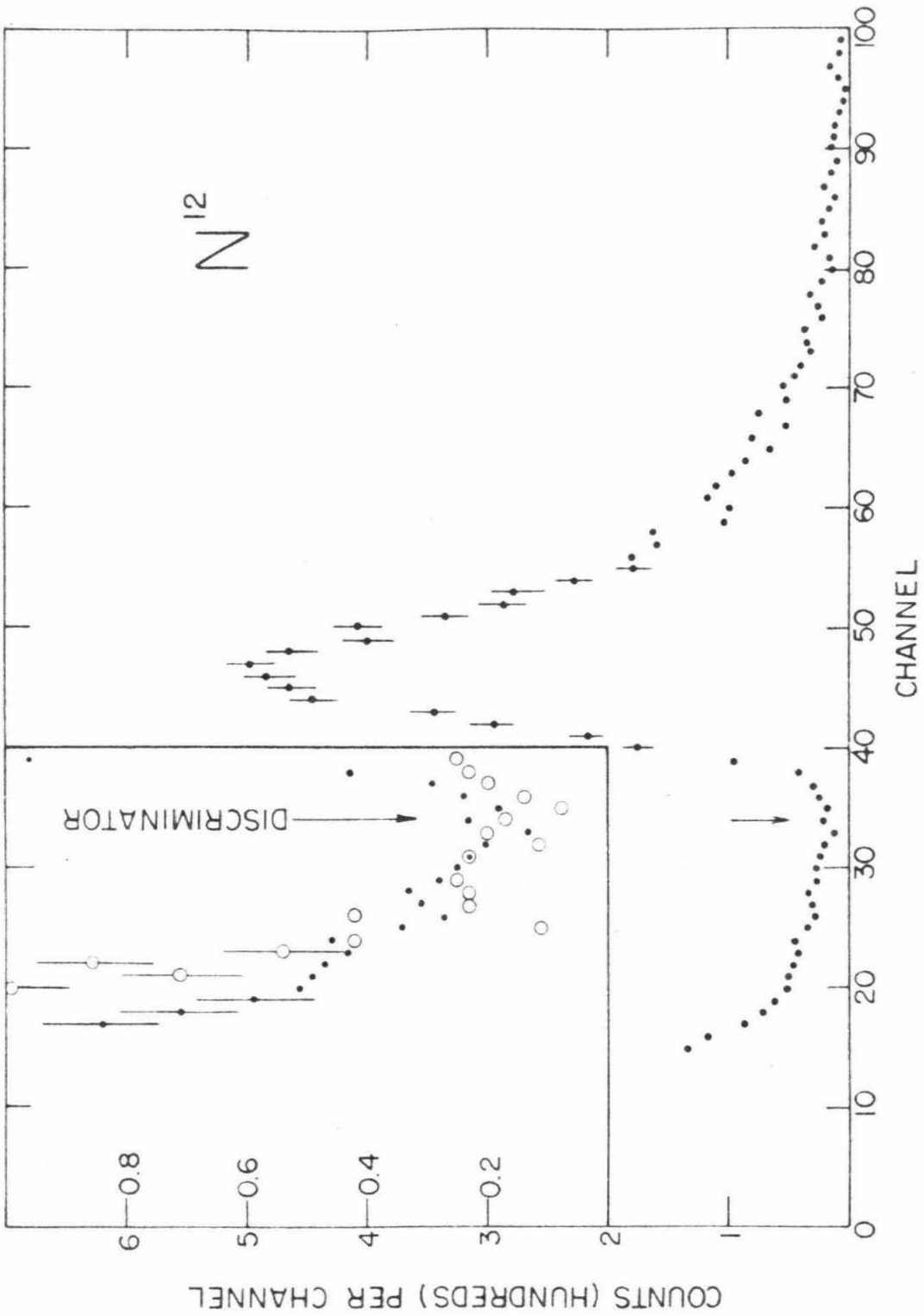
N^{12}
DISCRIMINATOR
CHANNEL
COUNTS (HUNDREDS) PER CHANNEL
0
10
20
30
40
50
60
70
80
90
100
1
2
3
4
5
6
0.2
0.4
0.6
0.8

FIG. 7

Fig. 8: Comparison of pulse-height distribution of 8-Mev electrons from B^{12} with the Landau curve.

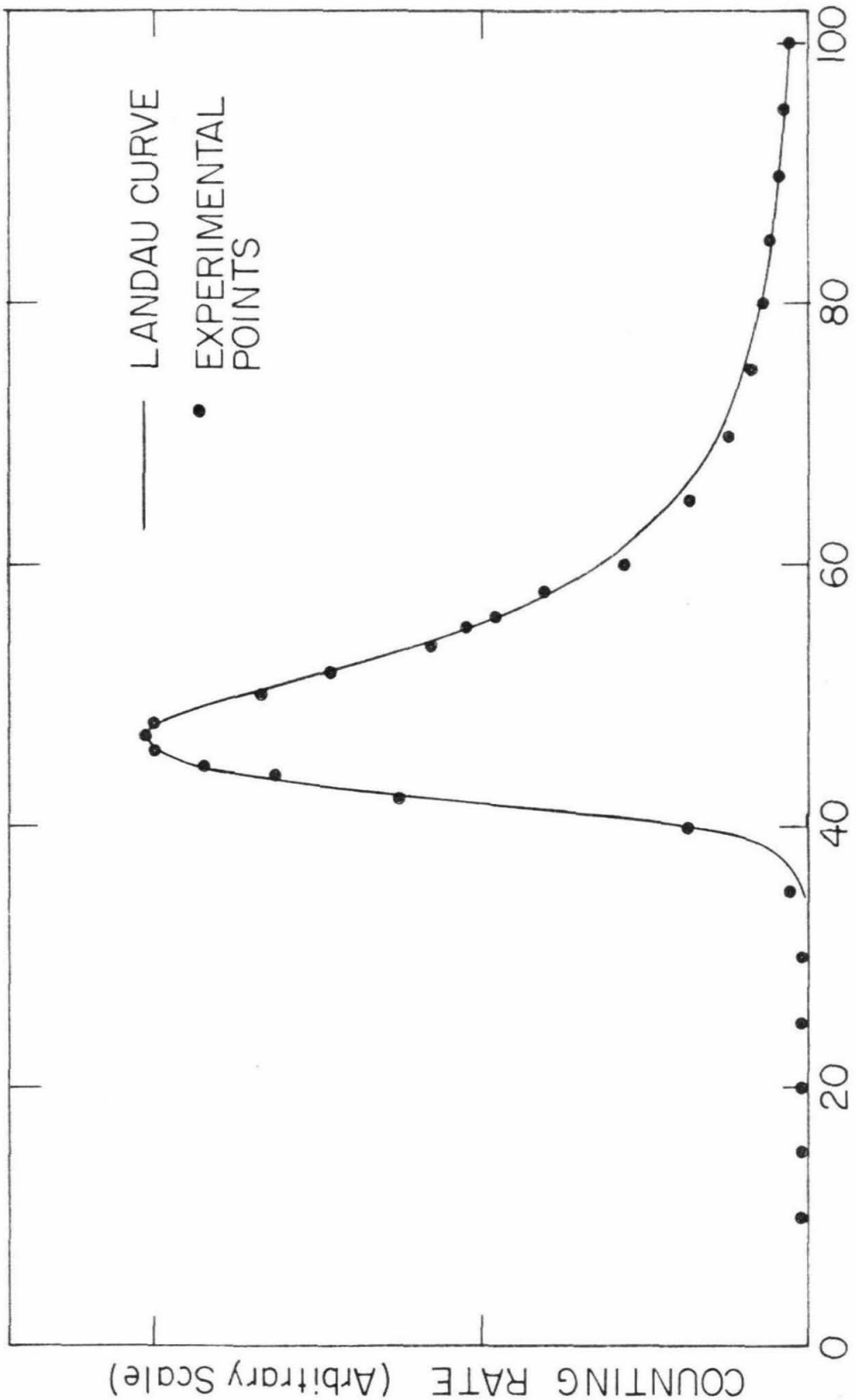
LANDAU CURVE
EXPERIMENTAL POINTS
COUNTING RATE (Arbitrary Scale)
0
20
40
60
80
100
CHANNEL (20 channels ≈ 1 Mev energy loss)

FIG. 8

Fig. 9: Pulse-height distributions of 5-, 8-, and 11-Mev electrons from B^{12} in the long NE-102 plastic scintillator.

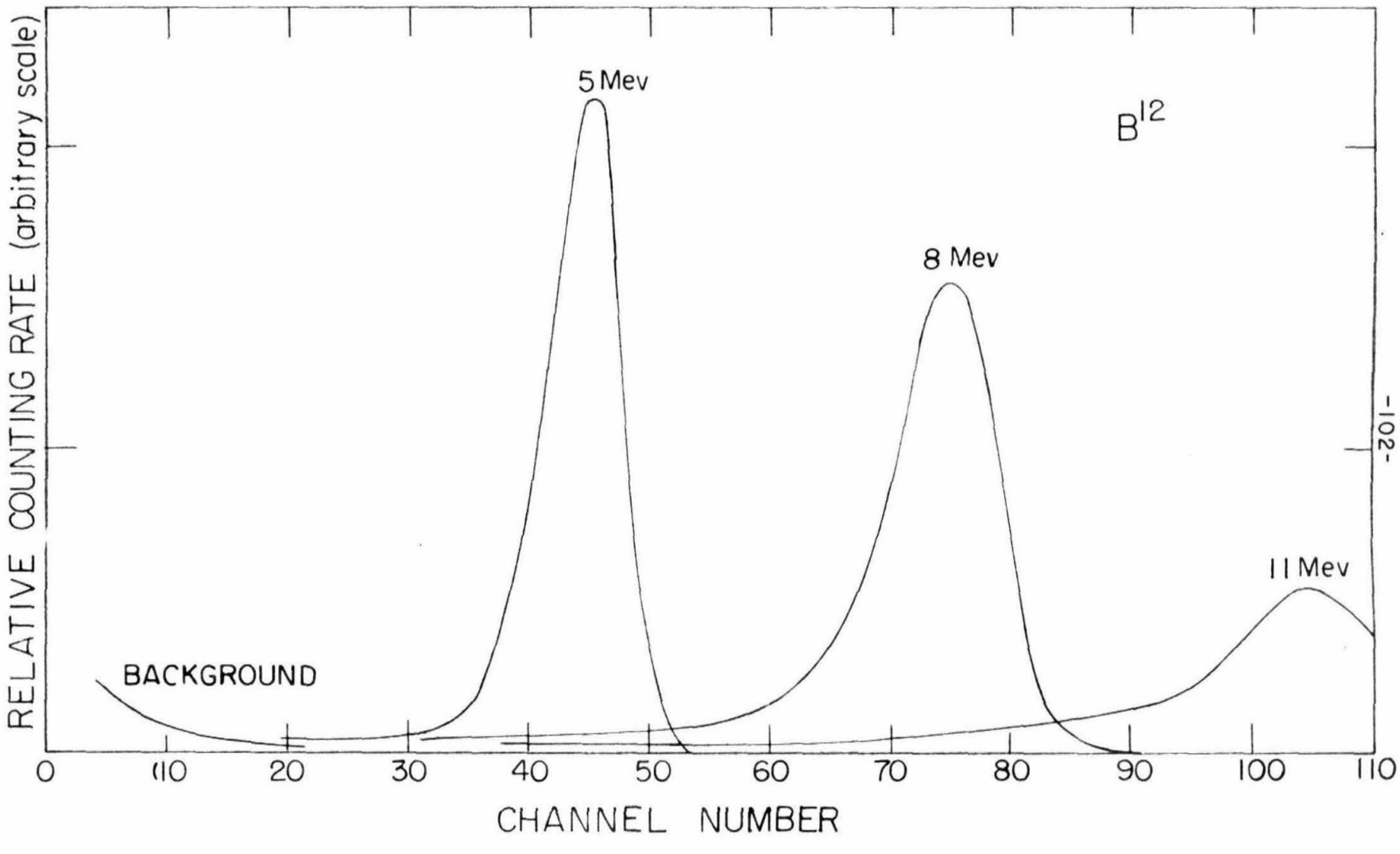
RELATIVE COUNTING RATE (arbitrary scale)
5 Mev
B12
8 Mev
11 Mev
BACKGROUND
0
10
20
30
40
50
60
70
80
90
100
110
CHANNEL NUMBER

FIG. 9

Fig. 10: Pulse-height distributions of 5-, 8-, and 13-Mev positrons from N^{12} in the long NE-102 plastic scintillator. Note the long tails into the relatively intense background.

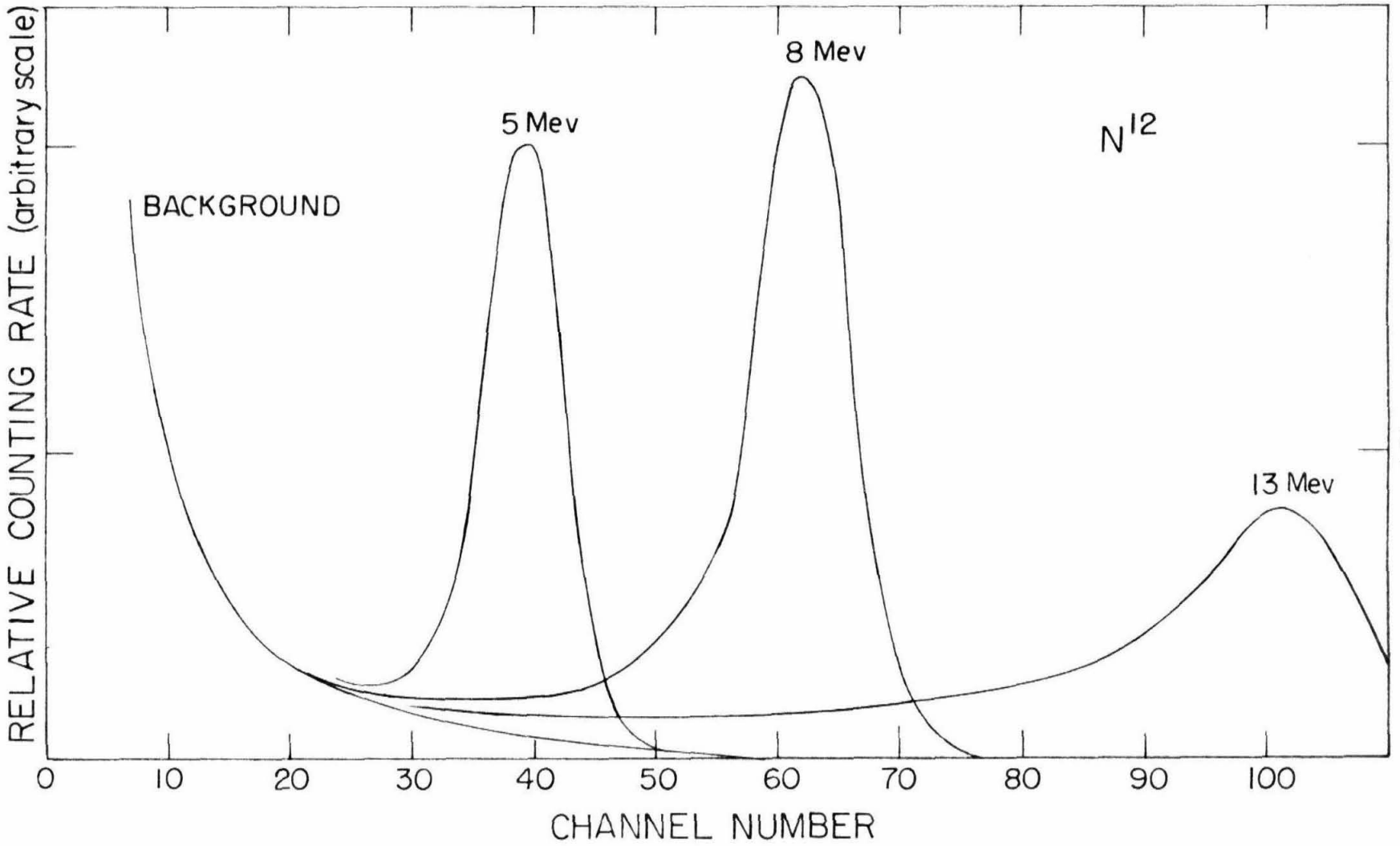
RELATIVE COUNTING RATE (arbitrary scale)
8 Mev
5 Mev
N12
BACKGROUND
13 Mev
0
10
20
30
40
50
60
70
80
90
100
CHANNEL NUMBER

FIG. 10

Fig. 11: Pulse-height distribution of protons from $B^{10}(d,p)B^{11}$ in the B^{12} experiment. The protons have passed through 118 mg/cm^2 of aluminum foil before being detected in the p-n junction counter. Arrow indicates the discriminator setting.

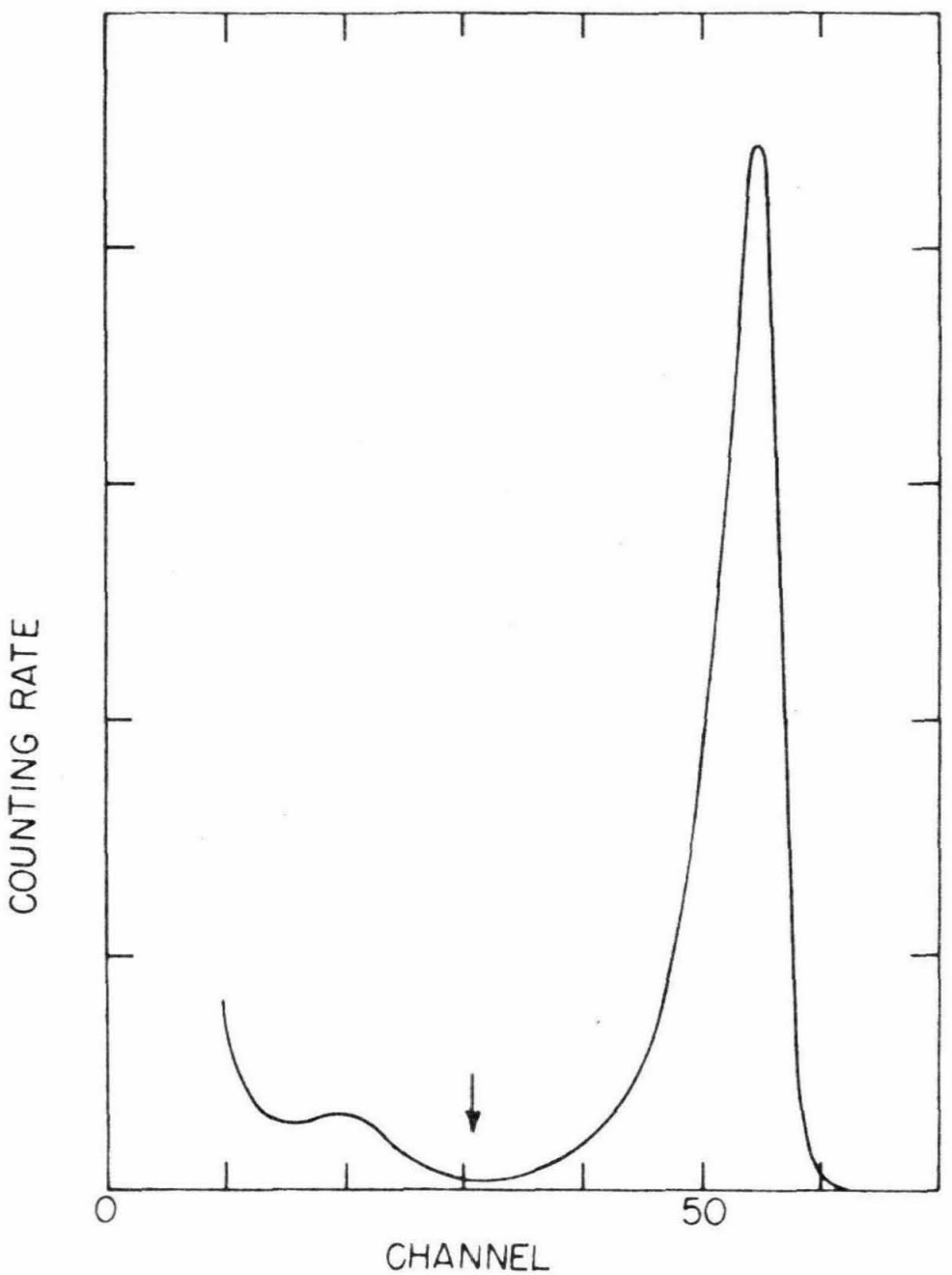

FIG. 11

Fig. 12: Block diagram of the counting and gating circuitry. An external timer to gate the scalers on and off is not shown.

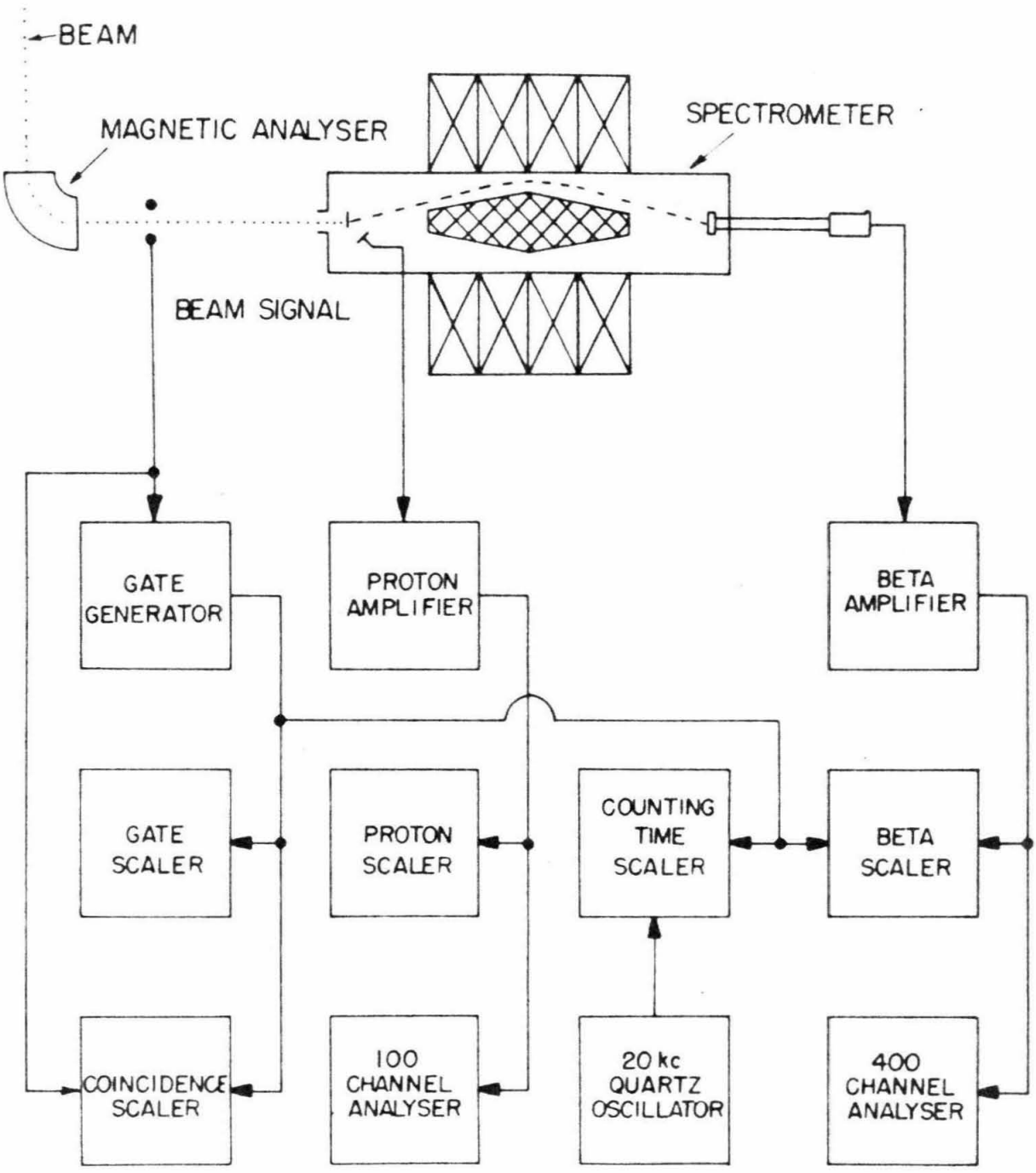
BEAM
MAGNETIC ANALYSER
SPECTROMETER
BEAM SIGNAL
GATE GENERATOR
PROTON AMPLIFIER
BETA AMPLIFIER
GATE SCALER
PROTON SCALER
COUNTING TIME SCALER
BETA SCALER
COINCIDENCE SCALER
100 CHANNEL ANALYSER
20 kc QUARTZ OSCILLATOR
400 CHANNEL ANALYSER

FIG. 12

Fig. 13: Apparatus for depositing boron. Entire system is glass, with all valves shown closed.

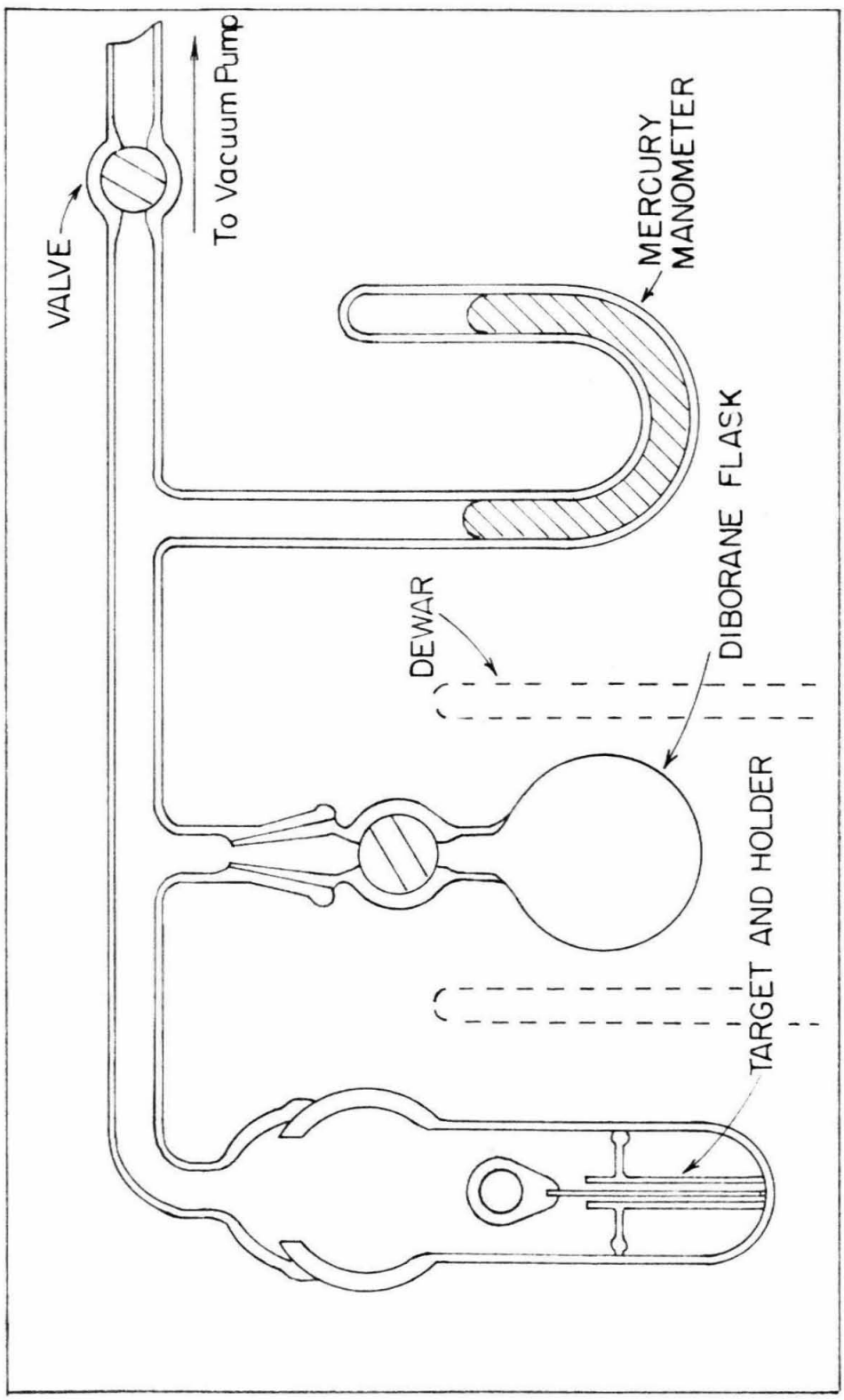
VALVE
To Vacuum Pump
MERCURY MANOMETER
DEWAR
DIBORANE FLASK
TARGET AND HOLDER

FIG. 13

Fig. 14: Target construction prior to deposition of boron. The aluminum foil was moistened with dilute shellac and used to pick up the nickel foil.

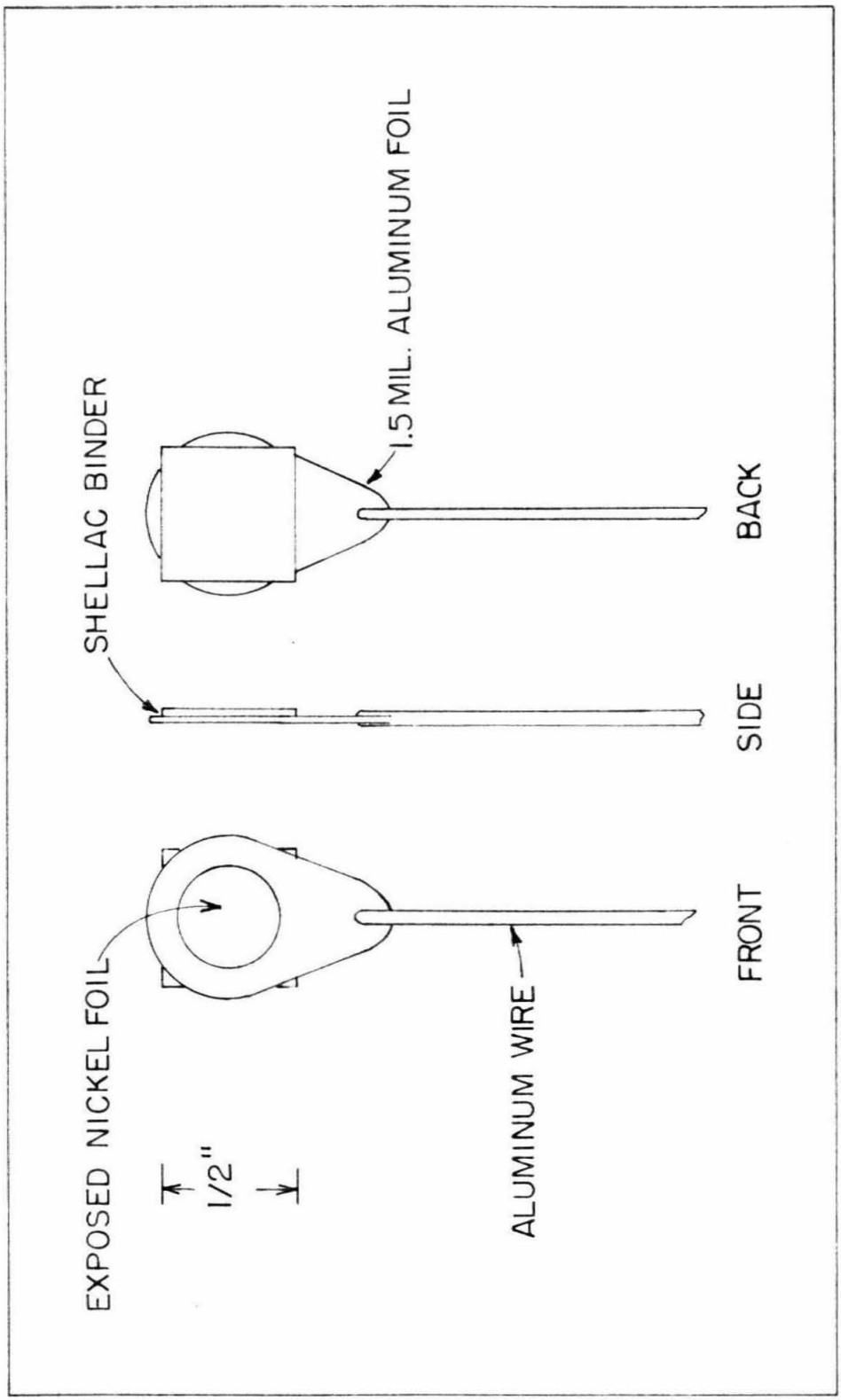
EXPOSED NICKEL FOIL
1/2"
ALUMINUM WIRE
FRONT
SHELLAC BINDER
SIDE
1.5 MIL. ALUMINUM FOIL
BACK

FIG. 14

Fig. 15: Counting rate vs energy plot of B^{12} and N^{12} data. Branching end points are indicated by arrows. Background at zero and high field is shown.

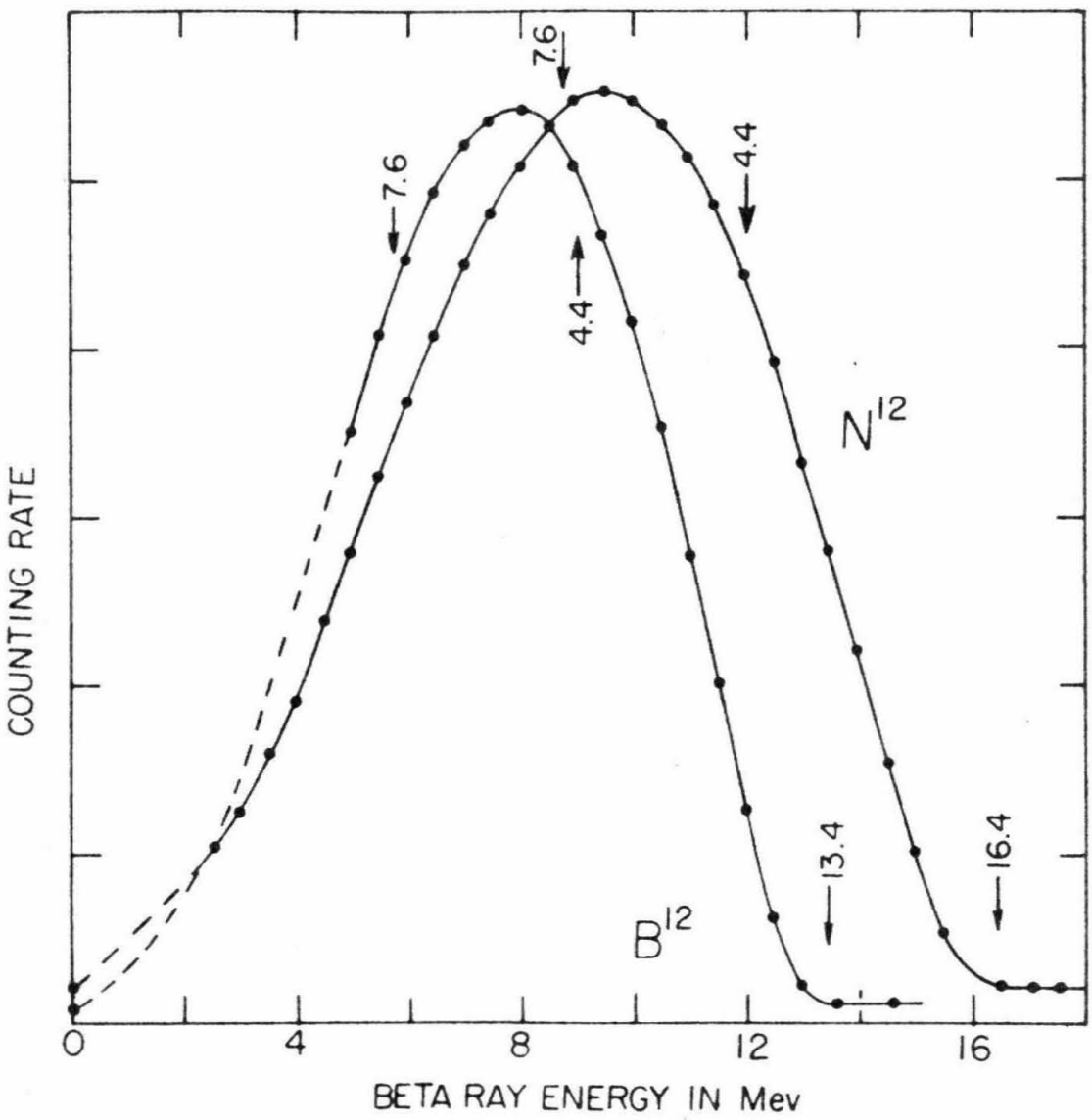
7.6
7.6
4.4
4.4
N^{12}
B^{12}
13.4
16.4
COUNTING RATE
0
4
8
12
16
BETA RAY ENERGY IN Mev

FIG. 15

Fig. 16: Fermi plots for B^{12} and N^{12}. The observed end-point energies, indicated in the figure, are in agreement with the values from reaction data of 13.369 Mev for B^{12} and 16.43 for N^{12}. The curvature of the N^{12} plot due to branching can easily be seen. In the B^{12} plot this effect is overcompensated by CVC-shape factors. Branching end points are indicated by arrows.

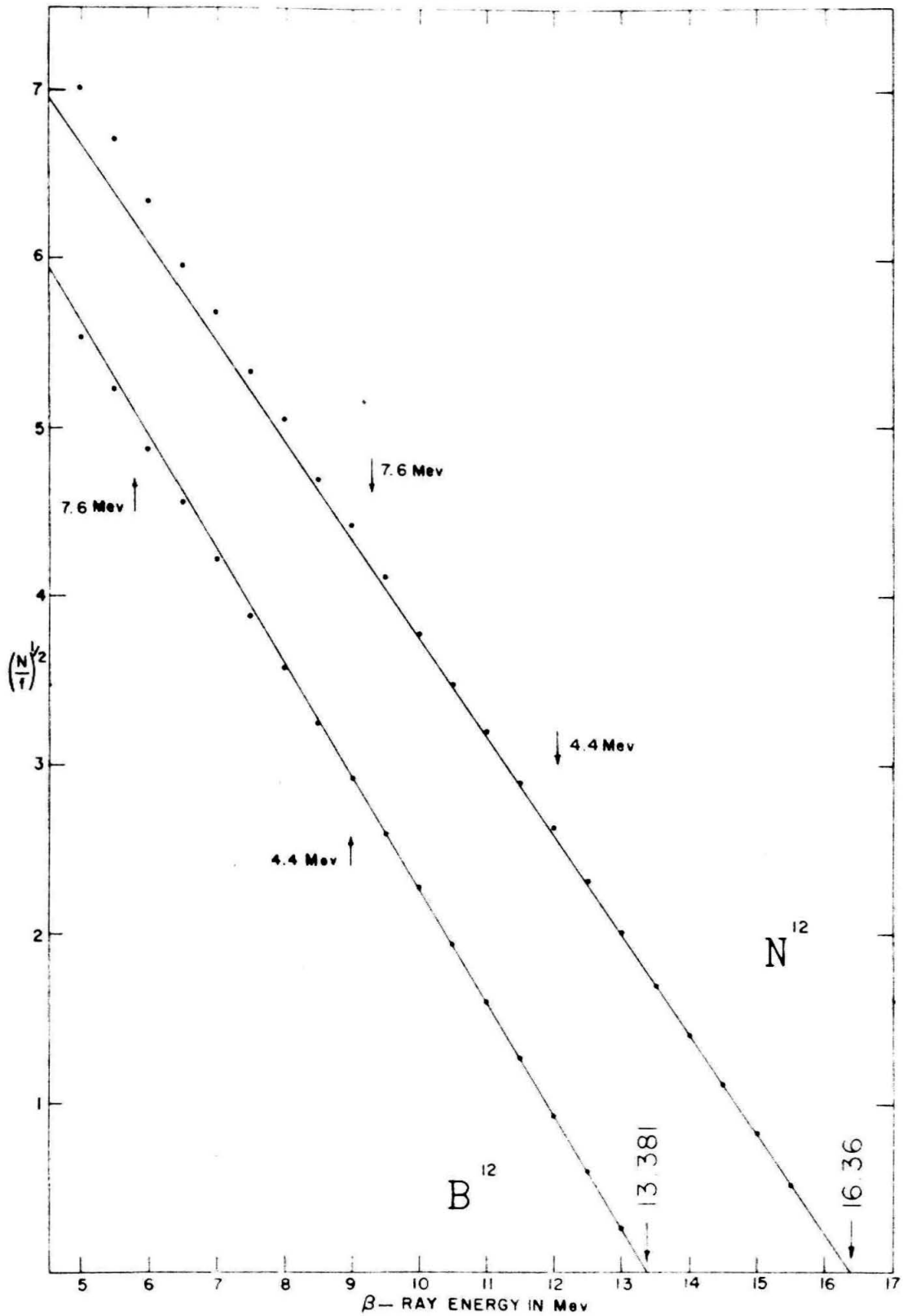
7
6
5
4
3
2
1
$\left(\frac{N}{T}\right)^{1/2}$
7.6 Mev
7.6 Mev
4.4 Mev
4.4 Mev
N^{12}
B^{12}
13.381
16.36
5
6
7
8
9
10
11
12
13
14
15
16
17
β— RAY ENERGY IN Mev

FIG. 16

Fig. 17: Plots of the shape factors $S(E,B^{12})$ $f(E,B^{12})$ and $S(E,N^{12})$ $f(E,N^{12})$ normalized to unity at 8 Mev. Statistical errors and least-squares fits are shown. Branching end points are indicated by arrows. Slopes are 1.82 percent per Mev for B^{12} and 0.60 percent per Mev for N^{12}.

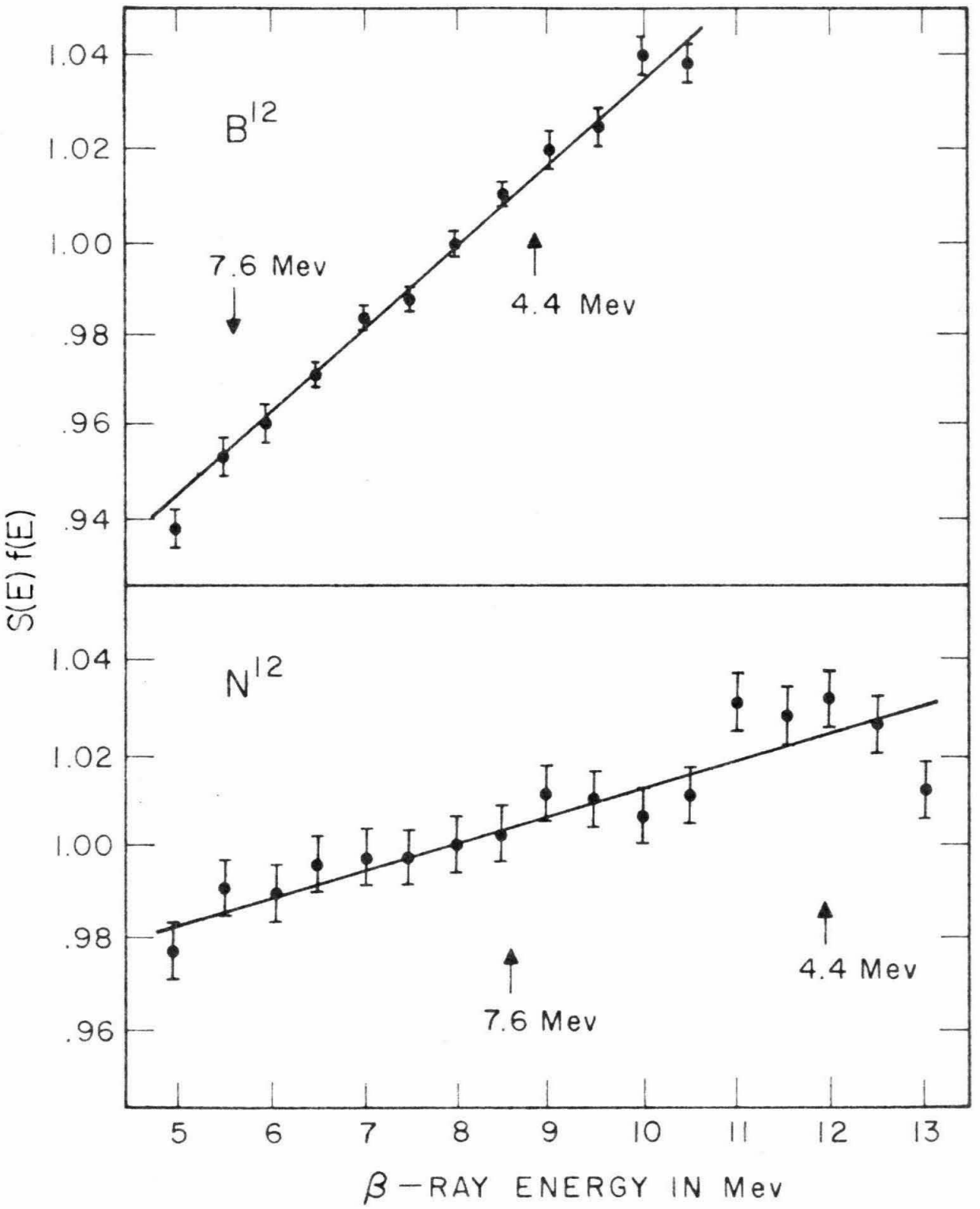
1.04
1.02
1.00
.98
.96
.94
B12
7.6 Mev
4.4 Mev
1.04
1.02
1.00
.98
.96
N12
4.4 Mev
7.6 Mev
S(E) f(E)
5
6
7
8
9
10
11
12
13
β — RAY ENERGY IN Mev

FIG. 17

Fig. 18: Fermi plots of the contribution from the 7.6-Mev branch in N^{12} after subtraction of the ground-state transition, assuming the indicated shape factors, and the 4.4.-Mev branch using the published branching ratio. The branching ratios indicated by these plots are 2.8 and 3.1 percent in that order. The end points are given by weighted least-squares fits. Error bars indicate the combined uncertainties of the 4.4-Mev branching ratio and the experimental data. The N^{12}-end point has been assumed to be 16.44 Mev in these examples.

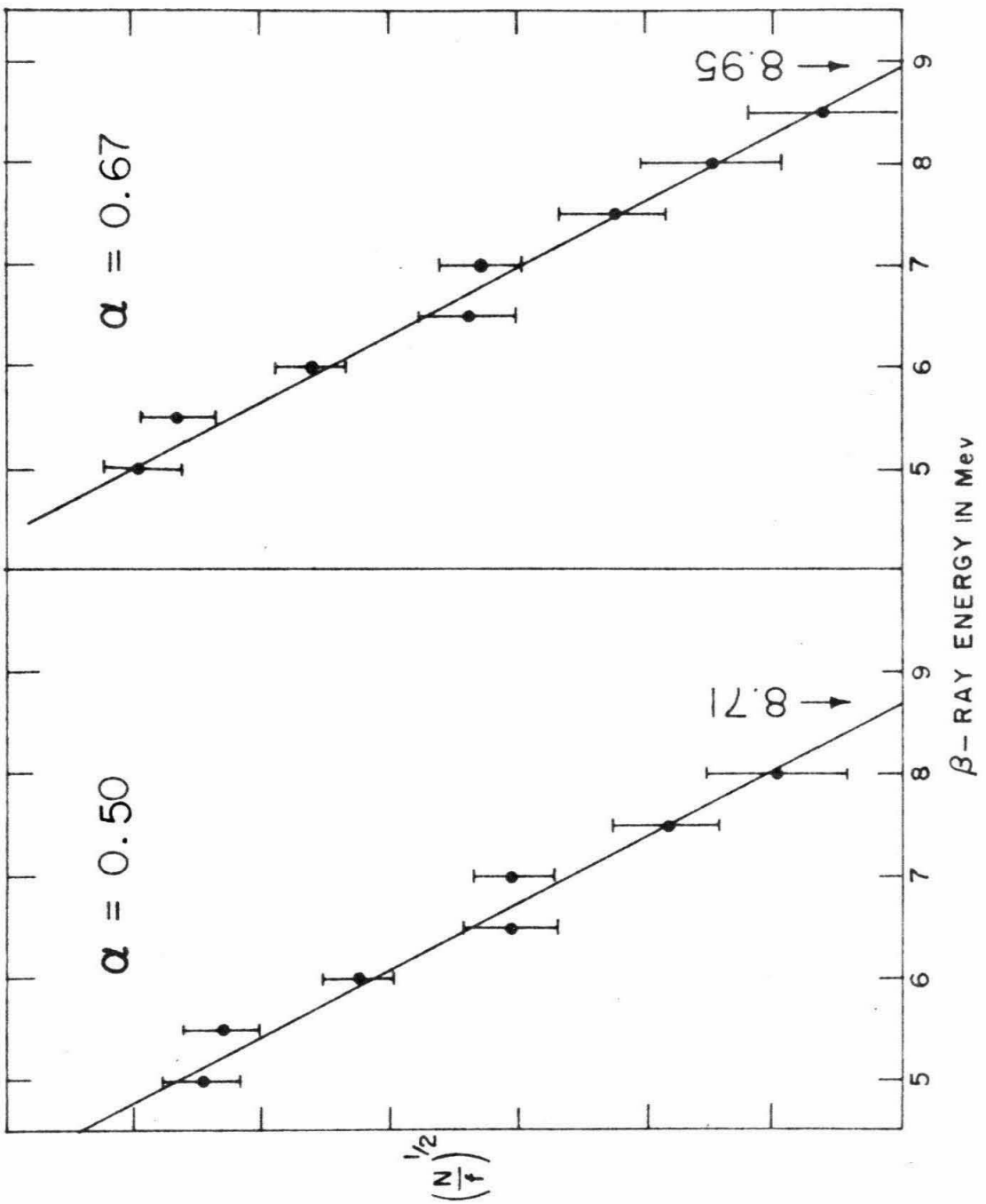
α = 0.50
α = 0.67
8.71
8.95
$\left(\frac{N}{f}\right)^{1/2}$
β- RAY ENERGY IN Mev
5
6
7
8
9

FIG. 18

Fig. 19: Error analysis. Four values of branching fraction (in parentheses next to data points) are plotted against the assumed end-point energy of the N^{12} ground state transition and the resultant end-point energy of the transition to the second excited state. The excitation energy of the second excited state has been measured accurately, and consequently the correct branching fraction must fall on this line. The best current N^{12} end point is shown with an arrow. The value of the branching fraction for this end point, satisfying the above constraint, is 2.96 percent. To first order the lines of constant branching fraction are independent of the assumed value of a. The uncertainty in the branching fraction is determined by projecting the end-point energy of the second-excited state as determined from the Fermi plots of Fig. 18 onto the branching fraction scale. A typical uncertainty is shown for the 3.11 percent point. The effect of the uncertainty ($\pm$ 60 Kev) in the ground state end point is obtained by projecting this uncertainty first on the line of constant excitation energy and from there onto the branching fraction scale. The two uncertainties are unrelated and give $\pm$0.4 (percent branching) when folded together.

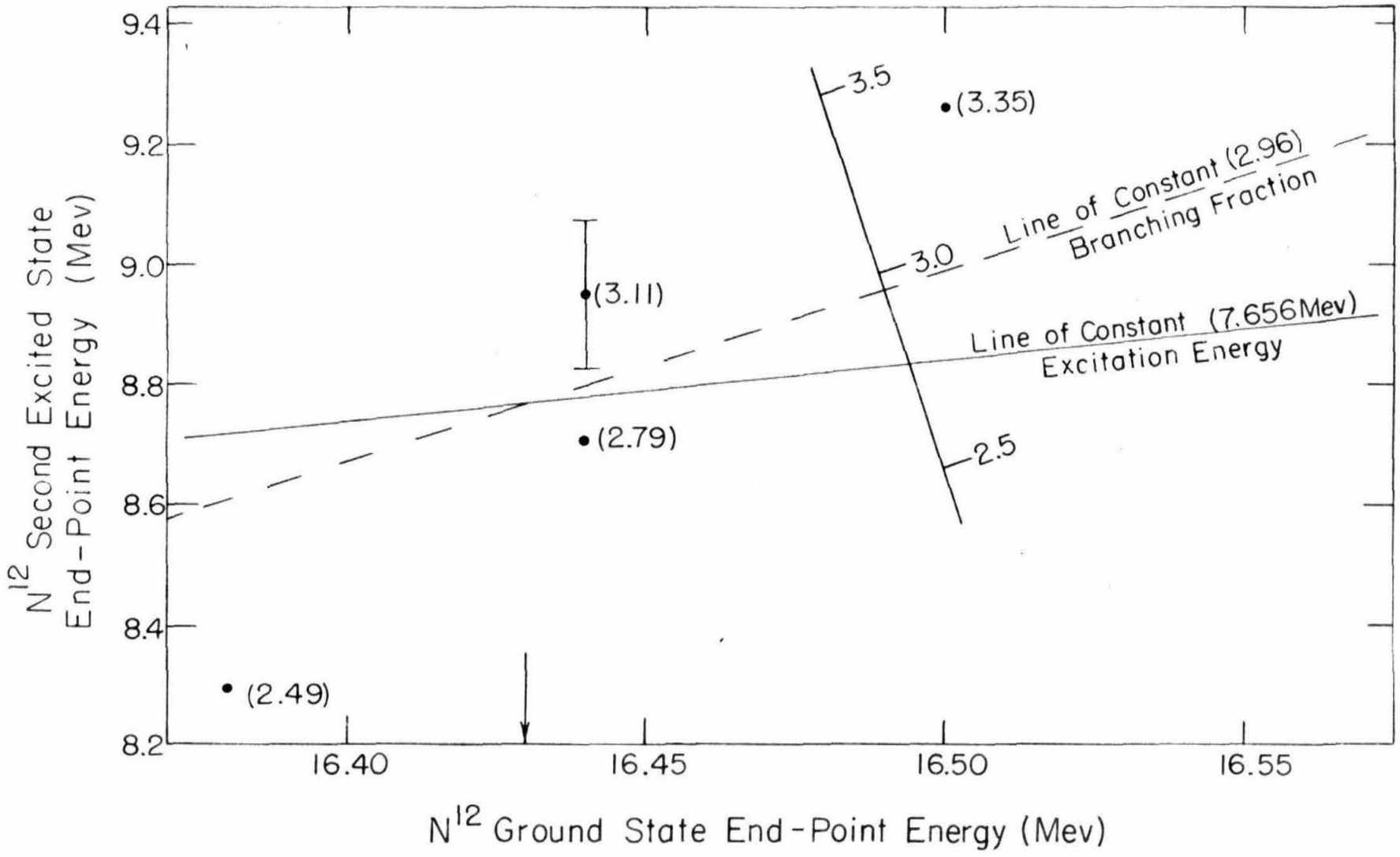
9.4
9.2
9.0
8.8
8.6
8.4
8.2
16.40
16.45
16.50
16.55
N12 Second Excited State End-Point Energy (Mev)
N12 Ground State End-Point Energy (Mev)
(3.35)
(3.11)
(2.79)
(2.49)
3.5
3.0
2.5
Line of Constant (2.96) Branching Fraction
Line of Constant (7.656Mev) Excitation Energy

FIG.19

Fig. 20: Line shape of the 0.4817-Mev conversion line of Bi^{207} for various displacements.

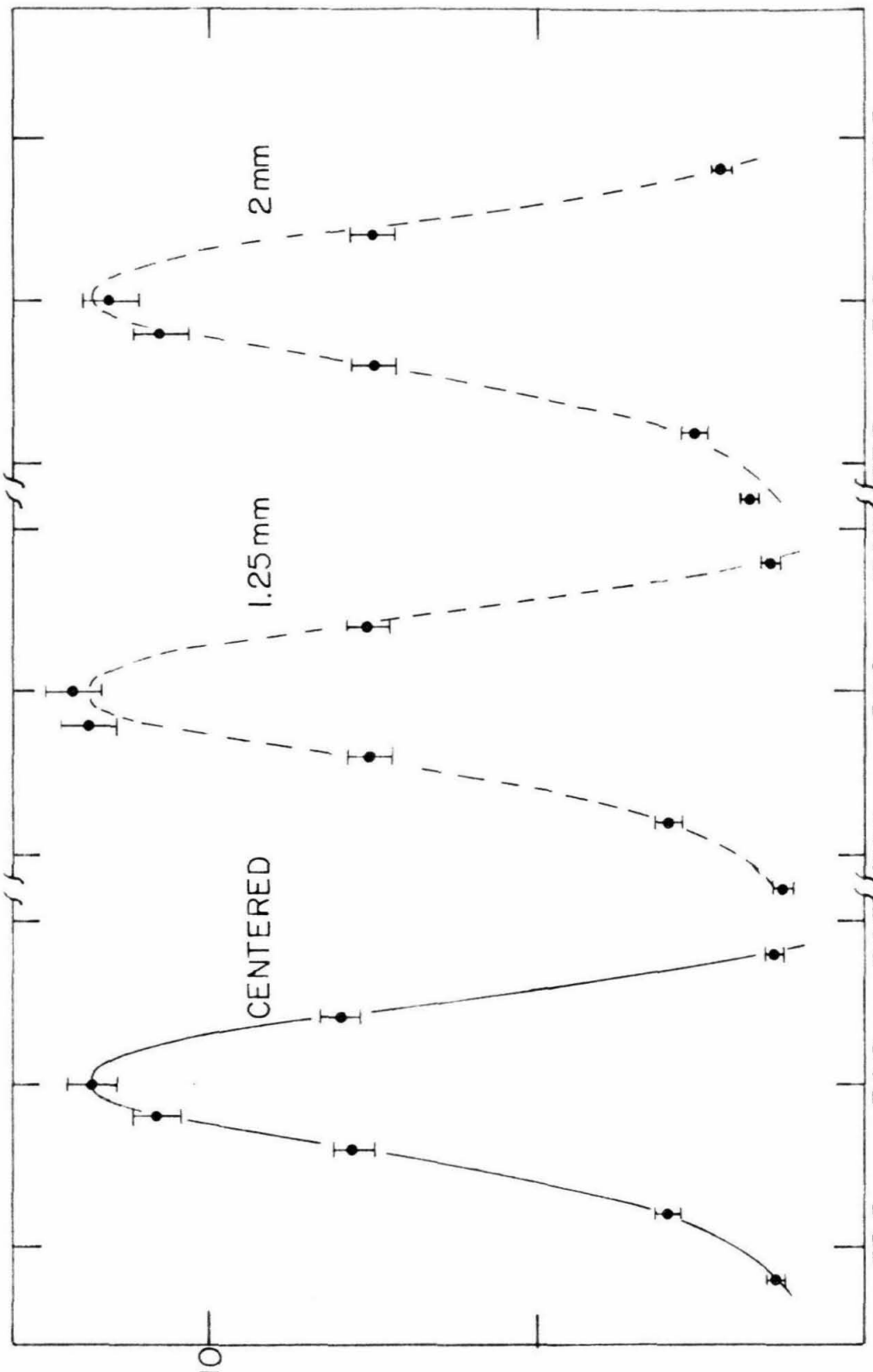
CENTERED
1.25 mm
2 mm
10
COUNTS (Hundreds)
33.5
34.0
34.5
MILLIVOLTS

FIG. 20

Fig. 21: $\left(\| 3(\vec{\sigma}\cdot\vec{r})\vec{r} - \vec{\sigma}r^2 \| \right)$ as a function of the parameters L/K, a/K for the Rosenfeld force mixture. The results for the Kurath and Sereber forces were essentially the same.

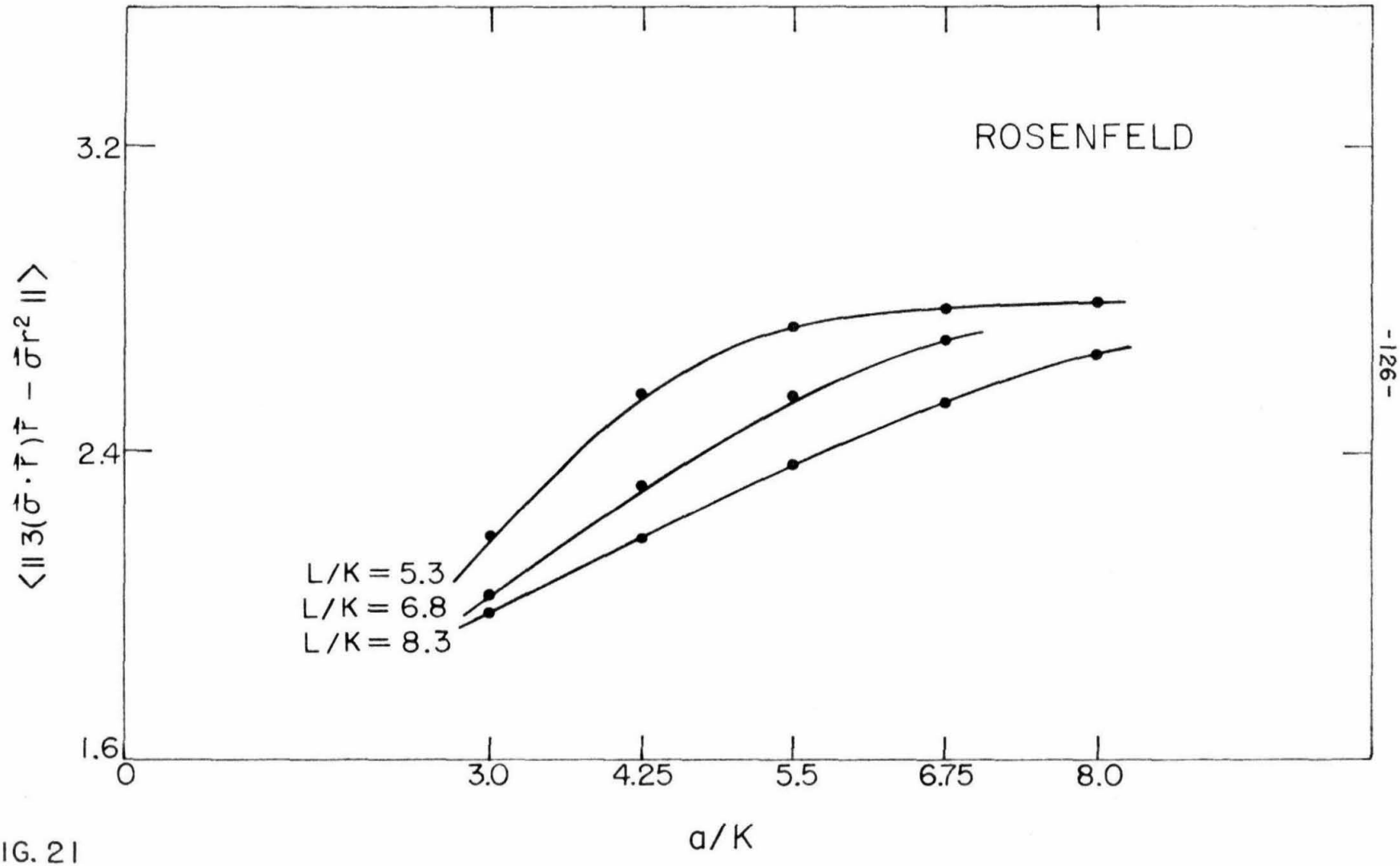
ROSENFELD
3.2
2.4
1.6
0
3.0
4.25
5.5
6.75
8.0
a/K
$\langle\| 3(\vec{\sigma}\cdot\vec{r})\vec{r} - \vec{\sigma}r^2 \|\rangle$
L/K = 5.3
L/K = 6.8
L/K = 8.3

FIG. 21

Fig. 22: Schematic of alignment arrangement.

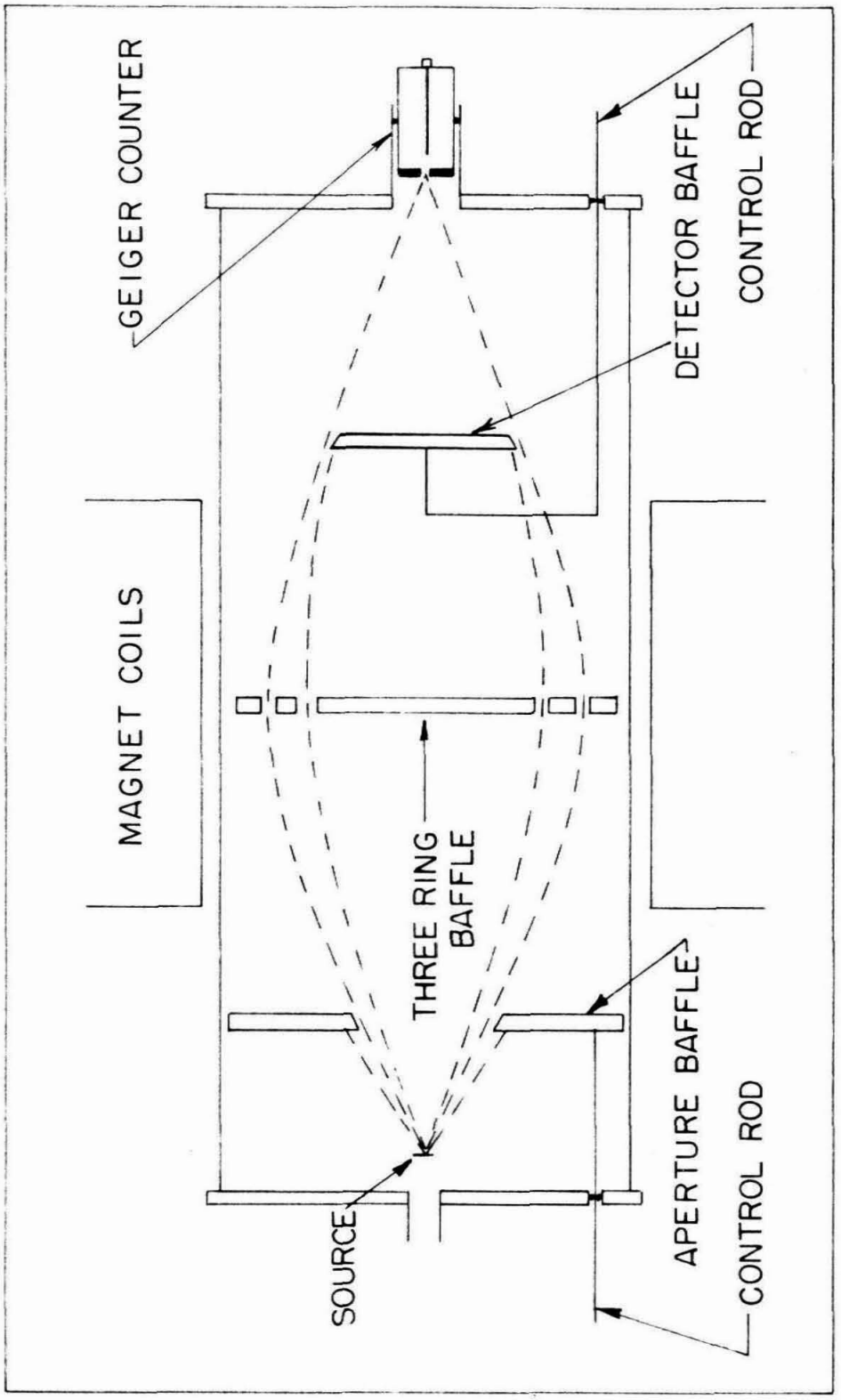
GEIGER COUNTER
DETECTOR BAFFLE
CONTROL ROD
MAGNET COILS
THREE RING BAFFLE
APERTURE BAFFLE
SOURCE
CONTROL ROD

FIG. 22

Fig. 23: Profile of the 0.6616-Mev Cs^{137} conversion line after alignment. The second peak is the L-electron conversion line.

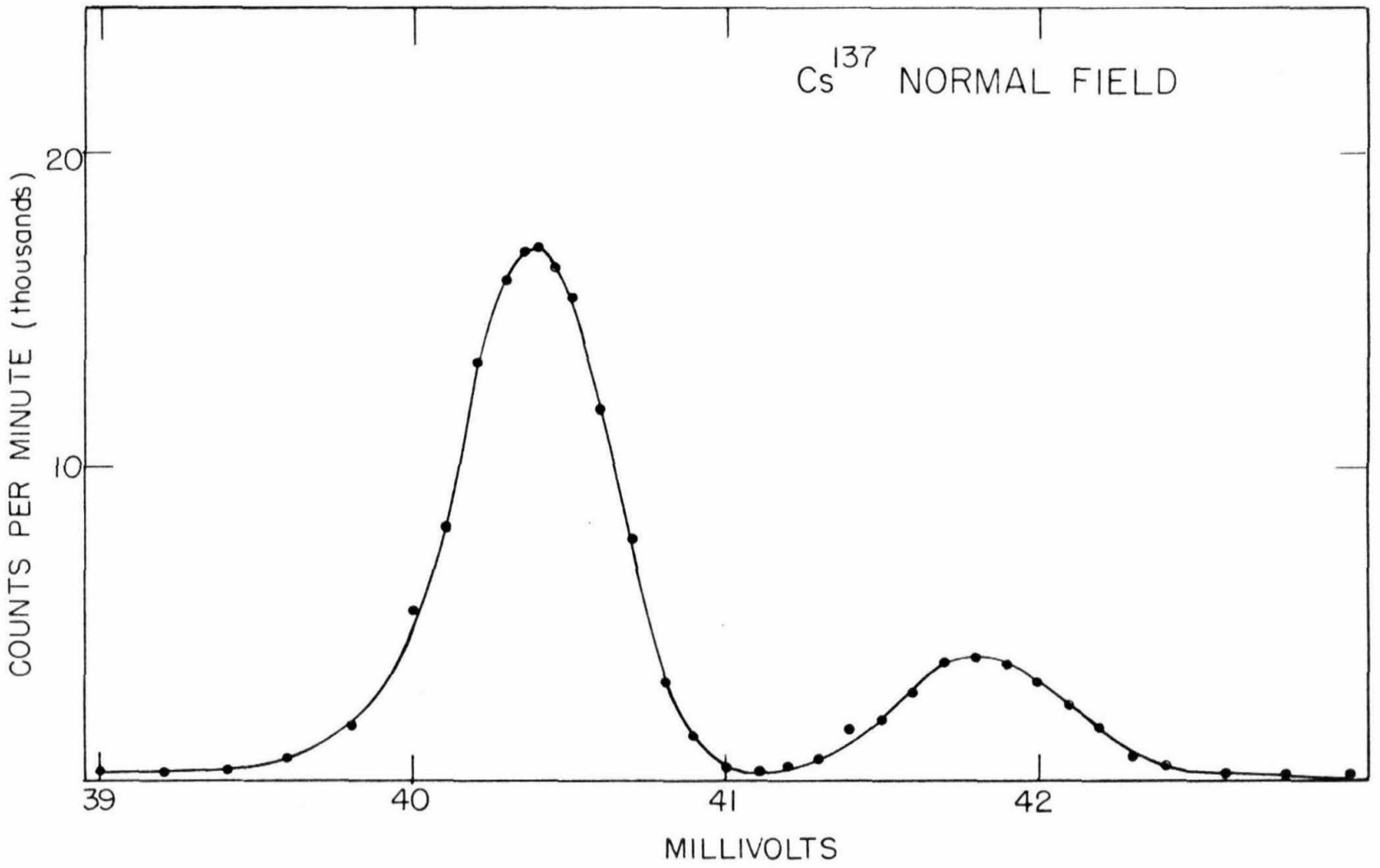
Cs137 NORMAL FIELD
COUNTS PER MINUTE (thousands)
20
10
39
40
41
42
MILLIVOLTS

FIG 23

Fig. 24: Profile of the Cs^{137} conversion line with reversed field.

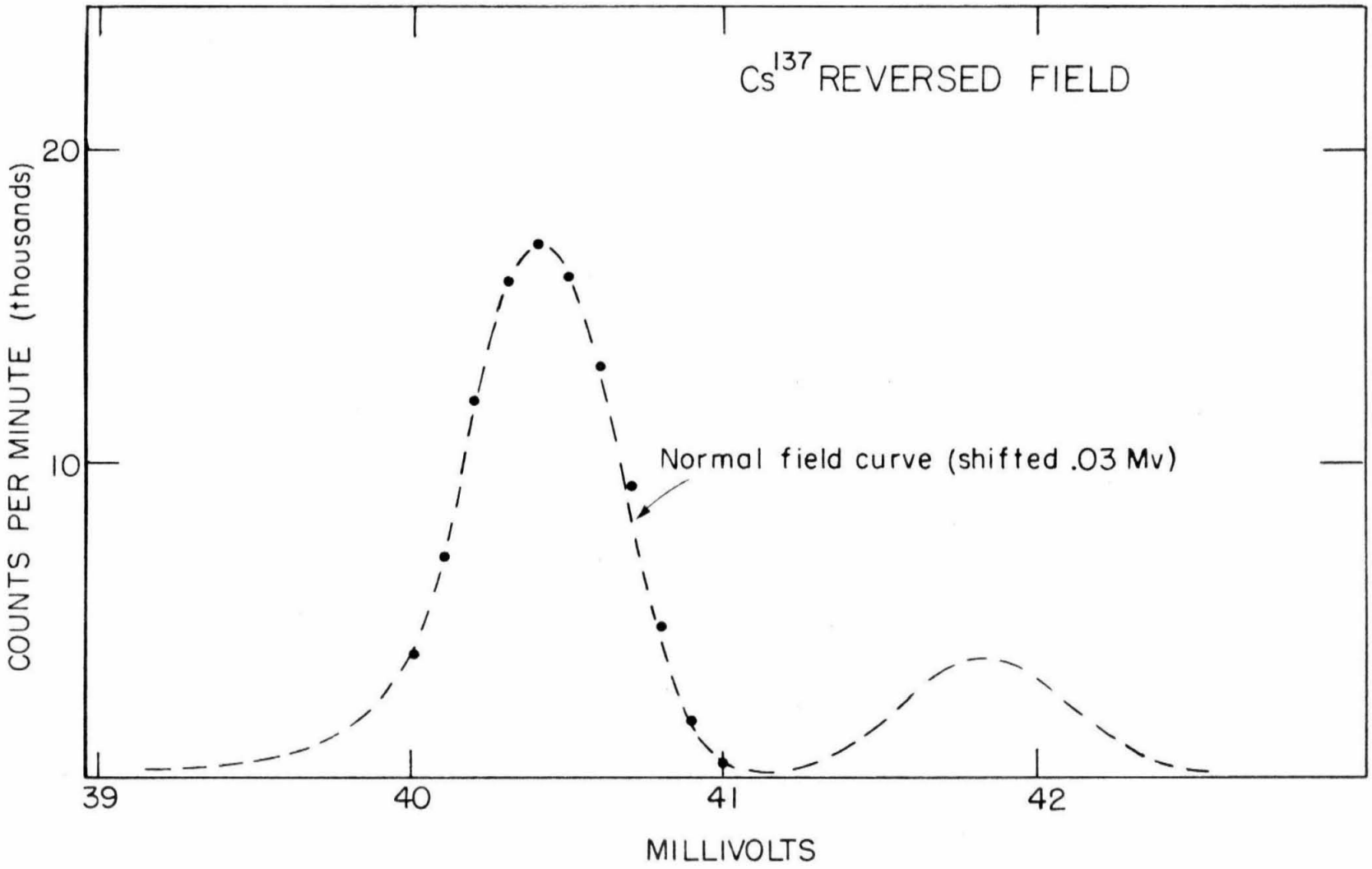
Cs137 REVERSED FIELD
COUNTS PER MINUTE (thousands)
20
10
Normal field curve (shifted .03 Mv)
39
40
41
42
MILLIVOLTS

FIG. 24

Fig. 25: Schematic for baffle penetration analysis. Insert shows actual situation.

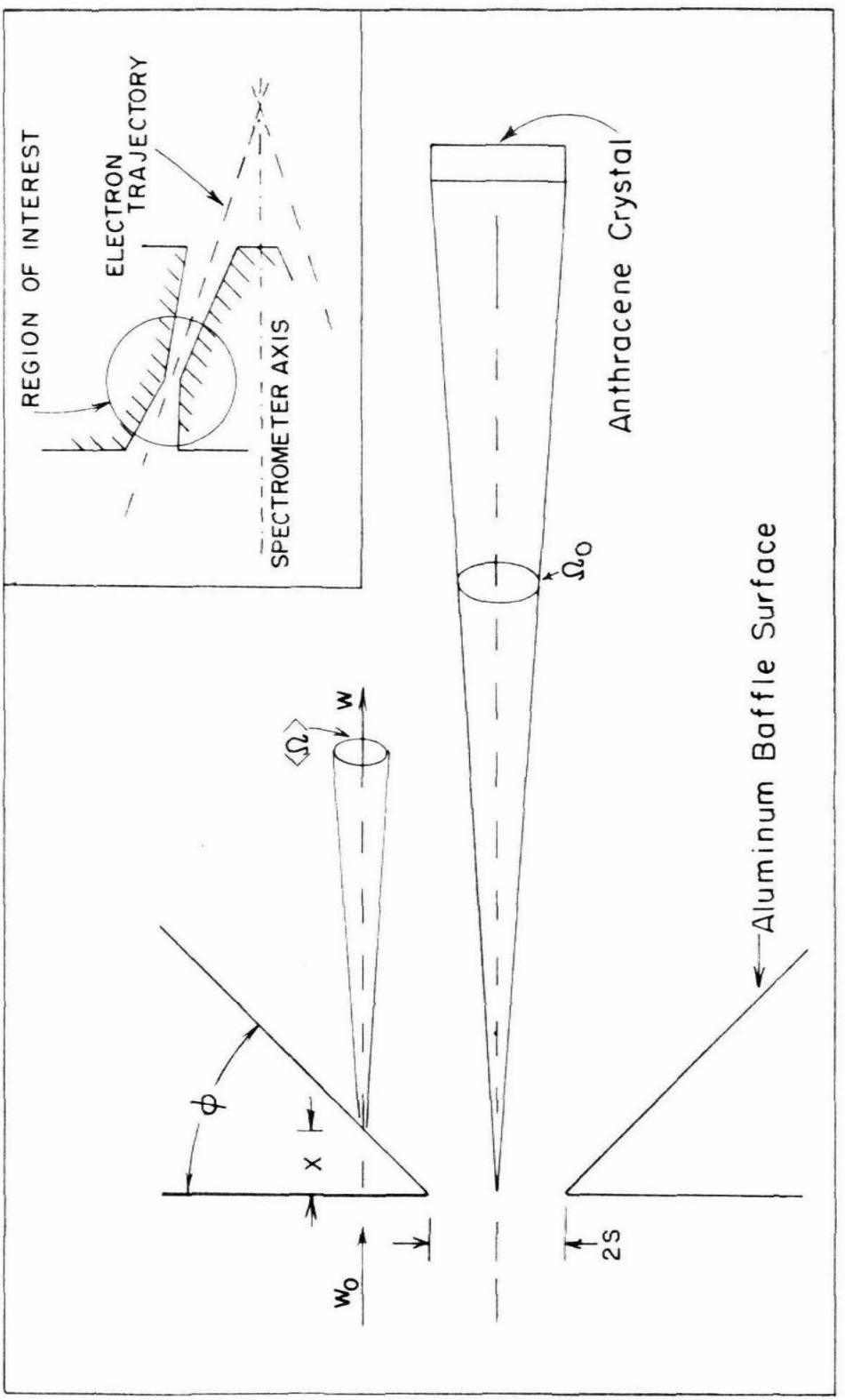
REGION OF INTEREST
ELECTRON TRAJECTORY
SPECTROMETER AXIS
Anthracene Crystal
Aluminum Baffle Surface
Ω_0
$\langle\Omega\rangle$
w
ϕ
x
w_0
2s

FIG. 25